Title
Fluctuations in Radiation Backgrounds at High Redshift and the First Stars

Author
Holzbauer, Lauren Nicole

Publication Date
2014

University of California
Los Angeles

Fluctuations in Radiation Backgrounds at High Redshift and the First Stars

A dissertation submitted in partial satisfaction
of the requirements for the degree
Doctor of Philosophy in Astronomy

by

Lauren Nicole Holzbauer

2014

Abstract of the Dissertation

Fluctuations in Radiation Backgrounds at High Redshift and the First Stars

by

Lauren Nicole Holzbauer

Doctor of Philosophy in Astronomy

University of California, Los Angeles, 2014

Professor Steven R. Furlanetto, Chair

The first stars to light up our universe are as yet unseen, but there have been many attempts to elucidate their properties. The characteristics of these stars ('Population/Pop III' stars) that we do know lie mostly within theory; they formed out of metal-free hydrogen and helium gas contained in dark matter minihalos at redshifts $z \sim 20-30$. The extent to which Pop III star formation reached into later times is unknown. Current and near future instruments are incapable of resolving individual Pop III stars. Consequently, astronomers must devise creative means with which to indirectly predict and measure and their properties. In this thesis, we will investigate a few of those means.

We use a new method to model fluctuations of the Lyman-Werner (LW) and Lyman-α radiation backgrounds at high redshift. At these early epochs the backgrounds are symptoms of a universe newly lit with its first stars. LW photons (11.5-13.6 eV) are of particular interest because they dissociate molecular hydrogen, the primary coolant in the first minihalos that is necessary for star formation. By using a variation of the 'halo model', which describes the spatial distribution and clustering of halos, we can efficiently generate power spectra for these backgrounds. Spatial fluctuations in the LW and (indirectly) the Lyman-α BG can tell us about the transition from primordial star formation to a more metal-enriched

mode that marks the beginning of the second generation of stars in our Universe.

The Near Infrared Background (NIRB) has for some time been considered a potential tool with which to indirectly observe the first stars. Ultraviolet (UV) emission from these stars is redshifted into the NIR band, making the NIRB amenable for hunting Pop III stellar signatures. There have been several measurements of the NIRB and subsequent theoretical studies attempting to explain them in recent years. Though controversial, residual levels of the mean NIRB intensity and anisotropies have been detected after subtracting all known foreground stars and galaxies. Pop III stars have been the leading candidates thought responsible for this observed NIRB excess. We model the Pop III stellar contribution to the NIRB mean intensity and fluctuations and generate observationally motivated values of the star formation (SF) efficiency using high redshift measurements of the UV luminosity density with UDF09, UDF12, and WMAP-9 data. This allows us to characterize the properties of a Pop III stellar population that are required to produce the measured excess.

Finally, we propose a new method for detecting primordial metal-free and very metal-poor stellar populations by cross-correlating fluctuations in the intensity of Lyman-α and He II $\lambda1640$ emission sourced from high redshifts. Pop III stars are expected to be more massive and more compact than later generations of stars. This results in a much harder ionizing spectrum. A large portion of the ionizing photons have energies with $h\nu > 54.4$ eV that carve out substantial patches of doubly ionized helium, He III. These photoionized regions then begin to shine brightly in He II recombination emission. Due to the lack of heavy elements in these regions, Pop III stars must rely on hydrogen and helium for cooling, enhancing both the Lyman-α and He II emission lines. In this regard, Pop III stars can be characterized as 'dual emitters,' i.e. producers of both Lyman-α and He II emission signatures. Though Lyman-α emission is characteristic of both metal-free and metal-enriched stars, He II emission appears to be unique to extremely metal poor stars and metal-free stars, making it a very strong signature of the first stars. Detecting Lyman-α + He II dual emission in individual galaxies at high redshift is difficult and so far rare. The astrophysical engines powering the few Lyman-α + He II dual emitters that have been discovered have still not been clearly identified. Alternatively, we may be able to map fluctuations in the total intensity of the Lyman-α and He II λ1640 lines, which will allow us to indirectly assess sources that are below typical luminosity thresholds of deep surveys. Cross-correlating these lines can provide us with a useful new tool for inferring properties of the first stars, since the two lines together allow us to better isolate the redshift of source emission and the presence of He II λ1640 emission is extremely sensitive to stellar metallicity.

The dissertation of Lauren Nicole Holzbauer is approved.

Edward L. Wright

Alice Eve Shapley

Abby Kavner

Steven R. Furlanetto, Committee Chair

University of California, Los Angeles

2014

To Mom and Loki

With Love

We did it!

Table of Contents

List of Figures

List of Tables

Acknowledgments

I would first and foremost like to sincerely thank my advisor, Steven Furlanetto, for his guidance and patience over the years, and for helping me develop an abstract inclination for astronomy into a rather calculated passion.

I would like to thank my doctoral committee members Abby Kavner, Alice Shapley, and Edward Wright.

I would like to thank my very excellent friend and fabulous astrophysicist, Bade Uzgil, for many candid discussions and her unquantifiable support in this rocky endeavor.

Chapter 1 is based on a version of [Holzbauer and Furlanetto, 2012].

Chapter 2 is a version of a to-be published article. We thank Joseph A. Muñoz for his collaboration on this project.

Chapter 3 is a version of a to-be published article.

This work was partially supported by the David and Lucile Packard Foundation.

Vita

2007	B.S. (Astrophysics)
	University of California, Los Angeles

Publications

Holzbauer, L. N., Furlanetto, S. R., "Fluctuations in the high-redshift Lyman-Werner and Lyman-alpha radiation backgrounds", 2012, Monthly Notices of the Royal Astronomical Society, 419, 718-731

CHAPTER 1

Introduction

In the beginning, our universe was very simple. There was no structure, no stars, nor were there any heavy elements. According to the standard cold dark matter (ΛCDM) paradigm, most of the mass in the universe is indeed cold and dark. This 'dark matter' (DM) was initially smoothly distributed in a homogeneous and isotropic Gaussian random density field. However, the primordial distribution was not perfectly smooth and was characterized by very small-amplitude density fluctuations. These tiny perturbations naturally grew over time and accumulated into overdense regions which then collapsed and formed gravitationally bound objects, or DM halos, on larger and larger scales. In this way, we can describe structure formation in the ΛCDM universe as 'bottom-up' or hierarchical; larger objects are made up of many smaller objects.

Within these DM halos, further structure formation takes place. Baryonic gas streams into the halo's gravitational well and becomes trapped, where it cools, collapses, and condenses into a very hot, dense ball of metal-free H/He gas that eventually heats up into the first star. These first stars (also known as 'Population III' stars) are theorized to have formed in minihalos (small halos with mass $\sim 10^6 M_\odot$) at redshifts $z \sim 20 - 30$ [Couchman and Rees, 1986a], or around a few hundred million years after the Big Bang. The minihalos have virial temperatures less than 10^4 K - below the threshold for atomic hydrogen cooling [Oh and Haiman, 2002]. Consequently, the halos have to rely primarily on H_2 for cooling [Haiman et al., 1996b, Tegmark et al., 1997, Abel et al., 2002, Bromm et al., 2002], making the extent of this first mode of star formation susceptible to dwindling supplies of H_2.

It is unknown as to how late Pop III star formation extends but it is clear that it is quenched over time by both radiative and chemical feedback. As the population of Pop III stars grows, the sites of star formation are increasingly irradiated by soft ultraviolet (UV) photons (the Lyman-Werner, or LW, bands: 11.2-13.6 eV) from existing stars. This LW radiation can photodissociate the H_2 molecules in the gas, destroying the only viable coolant supply and rendering the minihalos sterile. At this point, further star formation can only proceed in halos large enough to cool with atomic hydrogen, and begins to transition away from a truly primordial mode. Secondly, the first cosmic stock of heavy elements was cooked up in the cores of Pop III stars via nucleosynthesis. As these stars underwent supernova explosions, heavy elements were spewed across and mixed into the intergalactic medium (IGM), from which new metal-enriched stars formed, thus gradually ending the era of metal-free star formation.

Not only were the first stars the beginning of the bright, extraordinarily complex universe we live in today, but they may have played a significant role in the reionization of neutral hydrogen, an important milestone of cosmic evolution. But what do we really know about these stars outside of theory? We have yet to observe a single metal-free star, even one that sits at the very tail end of the primordial mode of star formation (which is likely to lie somewhere beyond $z \sim 7 - 8$). In fact, not much is known about the very high redshift universe. Even though we are determinedly traveling ever deeper into our cosmic history by studying the Hubble Ultra Deep Field (HUDF; [Oesch et al., 2012, Bouwens et al., 2013, Ellis et al., 2013, Robertson et al., 2013]) and embarking on new campaigns such as the Cluster Lensing and Supernova survey with Hubble (CLASH; [Postman et al., 2012]), we are still unable to directly detect Pop III stars.

In this thesis, we will explore methods with which to indirectly infer properties of the first stars. Though we cannot detect an individual Pop III star, we can assess the total radiative background originating from them and determine properties of the first stellar population as a whole, such as the initial mass function (IMF), characteristic mass, emissivity, and epochs of formation. In Chapter 2 we model fluctuations in the LW background and characterize the transition from primordial to second generation star formation. In Chapter 3 we discuss the viability of extracting a Pop III signal from the near-infrared background (NIRB), and in Chapter 4 we propose a new method with which to identify and extract a Pop III signal by cross-correlating Lyman-α and He II lines at high redshift. We conclude in Chapter 5.

CHAPTER 2

Fluctuations in the High-Redshift Lyman-Werner and Lyman-α Radiation Backgrounds

2.1 Introduction

An important aspect of the cold dark matter (CDM) universe is that density fluctuations exist on small scales. These small scale perturbations are superimposed on larger scale perturbations; the density reaches its highest value over the smallest region. Consequently, structure forms via hierarchical buildup. An initially smooth density distribution eventually morphs into a web of sheets and filaments. It is the overdense junctions of these filaments that we call dark matter halos. Further structure development takes place inside these halos, commencing with the first (Population III) stars.

Population III (Pop III) stars illuminated our dark universe in its cold youth and from them developed the complex environment we live in today. According to hierarchical structure formation, these stars formed out of metal-free H/He gas contained in minihalos at redshifts $z \sim 20$ - 30 [Couchman and Rees, 1986b]. The minihalos, with masses around $10^6 M_\odot$, have virial temperatures less than 10^4 K - below the threshold for atomic hydrogen cooling [Oh and Haiman, 2002]. Consequently, the halos have to rely primarily on H_2 for cooling [Haiman et al., 1996b, Tegmark et al., 1997, Abel et al., 2002, Bromm et al., 2002]. This cooling takes place via collisional excitation (mainly between H_2 molecules and energetic H atoms) and subsequent radiative decay of the rotational transitions of H_2.

In the classical view of Pop III star formation, molecular cooling produces a single, massive star from cold gas that becomes trapped in the dark matter potential well of one minihalo [Bromm et al., 2009]. A dense core, or protostar, gradually emerges and grows into a massive star by accreting the surrounding gas. These first stars could theoretically grow to be several hundred solar masses [Bromm and Loeb, 2004]; most were probably $\sim 100 M_\odot$ [Bromm and Larson, 2004]. But what would happen if the infalling gas became fragmented? Several studies show that a primordial protostellar cloud will most likely not violently fragment enough for a secondary clump to compete with the parent clump and form a second star [Abel et al., 2002, Yoshida et al., 2008]. However very recent simulations suggest that if a gas cloud surrounding a protostellar core has an initial degree of angular momentum, it could collapse into a dense disk, cool, and fragment, resulting in a binary or even multiple Pop III star system [Stacy et al., 2010a, Turk et al., 2009] consisting of two or more lighter stars as opposed to a single, massive star. These new studies could indicate that the formation of the first stars could be more complicated and varied than previously believed.

In these primordial star cookers, the ability to form new stars is dependent on the abundance of H_2. However, as the population of these luminous stars grows, the sites of star formation are increasingly irradiated by soft UV photons (the Lyman-Werner, or LW, bands: 11.2-13.6 eV) from existing stars. This LW radiation can photodissociate the H_2 molecules in the gas through the two-step Solomon process [Field et al., 1966, Stecher and Williams, 1967],

$$H_2 + \gamma \rightarrow H_2^* \rightarrow 2H, \tag{2.1}$$

in which an H_2 molecule hit by a LW photon bumps it up to an excited electronic state, H_2^* (this intermediate state is extremely short-lived, with a duration of only ~ 10 nanoseconds). A fraction of decays from this excited state end up in the vibrational continuum of the ground state, dissociating the molecule. If the LW background becomes strong enough, it can prevent further collapse and consequently stall the further formation of primordial ionizing sources by terminating the minihalos' primary cooling supply [Haiman et al., 1997]. As a result, the only halos able to cool (via atomic line cooling) and form new stars are those with $T_{\rm vir} > 10^4$ K, or masses above $\sim 10^8 \mathrm{M}_\odot[(1+z_{\rm vir})/10]^{-3/2}$. Minihalos, with temperatures below the threshold for atomic cooling, will not be able to collapse past virialization without a sufficient supply of H_2.

Although these larger halos may still form metal-free stars, the thermodynamics of the cooling process is sufficiently different that we expect the resulting stars to differ substantially (especially in their characteristic mass). The two populations are sometimes described as Population III.1 and Population III.2 to emphasize this: both may be 'primordial,' but they have very different properties regulated by the LW (and other) radiation backgrounds (see, e.g., [Bromm et al., 2009]).

Most previous calculations of the LW background used a homogeneous approximation, in which they assumed a uniform distribution of sources [Haiman et al., 2000, Ricotti et al., 2002, Yoshida et al., 2003]. But the highly clustered, discrete sources responsible for the background radiation do not generate a uniform background. If these fluctuations are large enough, the transition from H_2 cooling to atomic line cooling would be very patchy, potentially allowing exotic star formation to persist for long periods even after the mean background reaches the threshold value for H_2 suppression. [Dijkstra et al., 2008] were the first to consider the inhomogeneous LW background, but only in the context of close halo pairs (using a Monte Carlo model) and only when the background was already well above threshold. [Ahn et al., 2009] were the first to consider the inhomogeneous background using a large-scale radiative transfer simulation of reionization.

These photons have other observable effects as well; most importantly, as they redshift into the Lyman-α transition they couple the excitation temperature of the 21-cm transition of hydrogen to the gas kinetic temperature via a radiative pumping mechanism known as the Wouthuysen-Field effect [Wouthuysen, 1952, Field, 1959]. This renders the 21-cm signal visible in emission or absorption. [Barkana and Loeb, 2005a] showed that the fluctuations in this young Lyman-α background produced strong fluctuations in the 21-cm signal. Conversely, observing these fluctuations can reveal a wealth of information as to the properties of these first luminous sources. We will see that these photons begin to affect the 21-cm background at roughly the same background intensity at which they suppress H_2 cooling. Thus redshifted 21-cm measurements offer an excellent chance to study the transition from Population III.1 to III.2 stars as well as the inhomogeneities in the ultraviolet radiation field during the 'cosmic dawn.'

In this paper, we present a new method with which to efficiently calculate the power spectrum of an arbitrary radiation field for any desired redshift and range in scale (in this paper we focus on the LW and Lyman-α backgrounds specifically; see [Mesinger and Furlanetto, 2009] for an earlier application specific to the ionizing background). Using the halo model to determine the spatial distribution of halos, we can build up the radiation background by superimposing a flux profile specific to that particular background on each halo. This profile effectively replaces the mass density profile traditionally used in the halo model to calculate fluctuations in the density field. We aim to study the importance of fluctuations in these backgrounds and complement the radiative transfer simulation of [Ahn et al., 2009] with our simple, analytic model. Our method also takes a very different approach to calculating 21-cm fluctuations (due to perturbations in the Lyman-α radiation field) compared to existing work

[Barkana and Loeb, 2005a, Pritchard and Furlanetto, 2006].

In this first exploration of the radiation background, we restrict our attention to the soft-UV background from a relatively simple model of first galaxy formation. In fact, many other physical factors contributed to the transition from Population III to Population II star formation. The most obvious is metal enrichment, which also affects the cooling and is highly inhomogeneous (see, e.g., [Furlanetto and Loeb, 2005]). Also, X-rays emanating from the first sources can counteract H_2 destruction by increasing the free electron fraction and so catalyzing its formation [McDowell, 1961, Haiman et al., 1996a, Haiman et al., 2000]. There has been considerable debate as to which of these backgrounds is more influential. For our simple model, we will follow [Machacek et al., 2003] by assuming that the enhancement of the electron density due to the X-ray background occurs too slowly to compete with photodissociation and so neglect the X-ray background.

Recently, [Tseliakhovich and Hirata, 2010] pointed out that the residual relative velocities of the baryon fluid and underlying dark matter distribution, imprinted during the recombination era by the baryons' close coupling to photons and now visible as baryon acoustic oscillations, may have important implications for star formation in these early, fragile halos. These large-scale velocities will suppress the accretion of gas onto small dark matter halos [Tseliakhovich and Hirata, 2010, Tseliakhovich et al., 2011]. The actual implications for star formation are as yet unclear; the first simulations show modest effects on the reionization era itself [Maio et al., 2011, Stacy et al., 2011], but the effect on the earlier epochs is important for the LW and Lyman-α backgrounds [Dalal et al., 2010]. Because the effects are as yet unclear, we will ignore these velocity corrections here, thus providing a baseline prediction for comparison with future work better incorporating them.

This paper is organized as follows: in Section 2.2 we describe our method for calculating the power spectrum of the LW and Lyman-α radiation background fluctuations using the halo model. In Sections 2.3 and 2.4 we calculate the flux profiles for the LW and Lyman-α backgrounds, respectively, and also present our results. We summarize our results and conclude in Section 2.5. We adopt a background cosmology $(\Omega_0, \Omega_\Lambda, \Omega_b, h, \sigma_8, n) = (0.26, 0.74, 0.044, 0.74, 0.8, 0.95)$ consistent with the most recent measurements [Komatsu et al., 2011].

2.2 Method

We are interested in modeling the power spectrum of fluctuations in the LW and Lyman-α radiation backgrounds using the halo model. Unlike earlier treatments of the LW background, we are specifically interested in its large-scale inhomogeneities, complementing the high resolution, large-scale N-body radiative transfer simulation of [Ahn et al., 2009] and the small-scale treatment of [Dijkstra et al., 2008]. Instead we will expand the model of [Mesinger and Furlanetto, 2009], who treated the inhomogeneous hydrogen-ionizing ultraviolet background using a halo model-like prescription.

The halo model, as described in [Cooray and Sheth, 2002], uses properties of virialized dark matter halos to calculate the effects of non-linear gravitational clustering, assuming that all mass in the universe is compartmentalized in such halos, whose properties can be parameterized purely by their mass m. The three ingredients of the model are the (1) halo number density, $n(m)$, (2) spatial distribution of the halos, and (3) distribution of mass within each halo, or halo density profile, $\rho(r|m)$, (where r is the distance away from the center of a halo with mass m). Typically, a theoretically-motivated halo mass function for (1) (the classic choice being [Press and Schechter, 1974]) allows one to calculate (2). The density profile for (3) can be calibrated by numerical simulations, such as the NFW [Navarro et al., 1996] or [Moore et al., 1999] profiles. This model is very powerful in that it can efficiently determine the power and many other useful properties for any density field at an arbitrary epoch and scale.

Since we wish to quantify the radiation background rather than the mass density field, we simply replace the 'halo density profile' with the profile of the radiation field around each halo. This flux profile, $\rho_{\rm rad}(r|m)$, depends on the radiation background under consideration and will be discussed later. For a spherically symmetric profile, the normalized Fourier transform, $u(k|m)$, can be written as:

$$u(k|m) = \frac{\int_0^{r_c} dr 4\pi r^2 [\sin(kr)/(kr)] \rho_{\rm rad}(r|m)}{\int_0^{r_c} dr 4\pi r^2 \rho_{\rm rad}(r|m)}, \tag{2.2}$$

where r_c is the cutoff distance at which an observer can no longer see the radiation emanating from the source. For the case of the LW radiation, for example (described more fully in section 2.3.1), this cutoff distance, or horizon, is given by $r_{\rm LW} \sim 100$ comoving Mpc (cMpc).

As described above, we are interested in modeling the fluctuations in a variety of radiation backgrounds (in this paper, the LW and Lyman-α backgrounds). We use the power spectrum, $P(k)$, or the dimensionless quantity $\Delta(k) \equiv k^3 P(k)/2\pi^2$ to quantify these fluctuations. Following the halo model, we write the power as a sum of two terms: the first term, $P^{\rm 1h}(k)$, describes the case for which radiation at two points comes from the same source,[1] while the second term, $P^{\rm 2h}(k)$, describes the case for which the two points are illuminated by two sources:

$$P(k) = P^{\rm 1h}(k) + P^{\rm 2h}(k), \text{where} \tag{2.3}$$

$$P^{\rm 1h}(k) = \int_{M_{\rm min}}^{\infty} dm n(m) \left(\frac{m}{\bar{\rho} f_{\rm coll}}\right)^2 |u(k|m)|^2 \tag{2.4}$$

$$P^{\rm 2h}(k) = \left[\int_{M_{\rm min}}^{\infty} dm n(m) \left(\frac{m}{\bar{\rho} f_{\rm coll}}\right) u(k|m) b(m)\right]^2 P^{\rm lin}(k). \tag{2.5}$$

Here, $\bar{\rho}$ is the matter density, $f_{\rm coll}$ is the collapse fraction (fraction of mass in the universe contained in galaxies, or collapsed in a halo), $b(m)$ denotes the halo

[1] In the context of the halo model, our radiation background calculation is analogous to the dark matter density power spectrum in the halo model, *not* to the (discrete) galaxy power spectrum. Thus the 'one-halo' term is very important to our results on small scales, even if each halo contains only one galaxy.

bias (describing how strongly clustered the halos are; [Mo and White, 1996]), and lastly $P^{\rm lin}(k)$ is the linear power spectrum. Here we have approximated the halo-halo power spectrum, for two halos with mass m_1 and m_2, as $b(m_1)b(m_2)P^{\rm lin}(k)$, which requires that the halo fluctuations remain linear on the appropriate scales (i.e., those on which $P^{\rm 2h}$ dominates). While the density fluctuations themselves are very weak at the redshifts of interest to us, the halos are also highly biased, so nonlinear corrections will be important on sufficiently small scales. We use the [Eisenstein and Hu, 1999] fit to the transfer function to calculate $P^{\rm lin}(k)$ and the Sheth-Tormen mass function and collapse fraction [Sheth and Tormen, 1999].

To model the density power spectrum one must include the entire halo population, over all masses. However, we are interested in the total radiation field and so should not include the low-mass halos unable to host stars. We assume that only halos more massive than a cutoff mass, $M_{\rm min}$, host stars and so contribute to the radiation background. To motivate our choices for $M_{\rm min}$, we first consider the 'filter mass,' $M_{\rm filter}$, the characteristic scale over which baryonic perturbations are smoothed in linear perturbation theory or the minimum mass of a halo to accrete baryons [Gnedin and Hui, 1998, Naoz and Barkana, 2007], as a lower limit ($\sim 10^5 {\rm M}_\odot$ in our redshift regime). In linear theory, the relative force balance between gravity and pressure can be characterized by the Jeans mass, M_J; the corresponding Jeans scale is the minimum scale on which a small perturbation will grow due to gravity. M_J depends on the instantaneous value of the sound speed of the gas, consequently overestimating the characteristic mass scale by up to an order of magnitude [Gnedin, 2000]. In contrast, $M_{\rm filter}$, which takes into account the full thermal history of the gas, is a more accurate mass scale.

An upper limit would be the threshold for atomic cooling, $T_{\rm vir} \sim 10^8$K [Oh and Haiman, 2002]. Since the $\rm H_2$ fraction, $f_{\rm H_2}$, increases with halo mass ($f_{\rm H_2} \propto T_{\rm vir}^{1.5}$, [Tegmark et al., 1997]) the cutoff mass certainly lies somewhere between these two limits. The classical criterion that the cooling time be smaller than the dynamical time will set the redshift-dependent transition: in the absence of a LW background, these successful minihalos probably have $f_{\mathrm{H}_2} \sim 10^{-4}$ and $M_{\mathrm{halo}} \sim 10^6 \mathrm{M}_\odot$ [Haiman et al., 1996b, Tegmark et al., 1997, Yoshida et al., 2003]. However, rather than try to model this in detail we will employ a variety of selections for M_{min} in order to remain most general.

2.3 The LW Background

In this section we will apply the above method to fluctuations in the LW radiation background, which determines if the sterilization of minihalos at high redshift (through the photodissociation of H_2) was a patchy or homogeneous transition.

2.3.1 The Flux Profile

Our LW flux profile (shown in Figure 2.3.1 for $z = 10$ and 25) for a halo with mass, m, located at an effective luminosity distance, r, from the observer is given by:

$$\rho_{\mathrm{rad}}(r|m) \propto m \frac{f_{\mathrm{mod}}(r)}{4\pi r^2}, \tag{2.6}$$

where we assume for simplicity that the luminosity of each halo scales with its mass. [2] Here we use the picket fence modulation factor, $f_{\mathrm{mod}}(r)$, from [Ahn et al., 2009]. This is the fraction of LW continuum radiation emitted by a source that is received by the observer without redshifting into a hydrogen Lyman series resonance line, where it will either be absorbed or scattered. An absorbed photon will either cascade to the $2p$ level and produce a Lyman-α photon or cascade to the metastable $2s$ level and decay by two photon emission [Pritchard and Furlanetto, 2006]– either way, the resulting photon will be below the LW range. On the other hand, the scattered photon will be reab-

[2] A more complex relationship is likely, but any such relationship can be bracketed by our different choices of M_{min}.

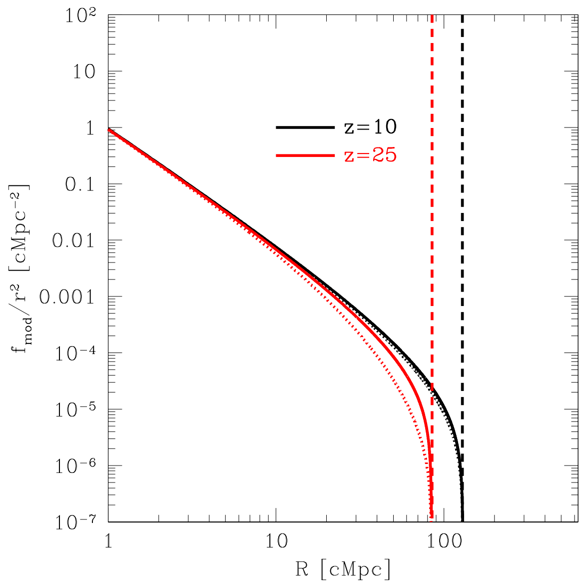

Figure 2.1: The normalized LW flux profile, $\rho_{\rm LW}(r|m)$, shown for $z = 10, 25$ (right and left sets of curves, respectively). Each profile terminates at the horizon $r_{\rm LW}$, indicated by the vertical dashed lines. The dotted curves represent the corresponding time dependent versions of the flux profile using the timescale of typical halo growth, $t_\star$, for $M_{\rm min} = 10^8 {\rm M}_\odot$.

sorbed until it, too, decays into a low-frequency photon (typically after just a few scatterings). So, for a given photon at observed frequency, $\nu_{\rm obs}$, we can define a maximum redshift, $z_{{\rm max},i}$, corresponding to the maximum distance within which photons from a source remain in the LW band without redshifting into the closest Lyman line from above (located at frequency ν_i):

$$\frac{1+z_{{\rm max},i}}{1+z_{\rm obs}} = \frac{\nu_i}{\nu_{\rm obs}}. \tag{2.7}$$

With each Lyman line associated with its own $z_{{\rm max},i}$ and the spacing between them decreasing with increasing ν_i, we are left with a transmission spectrum resembling a poorly fashioned picket fence, illustrated in Figure 2 from [Ahn et al., 2009]. The modulation factor, $f_{\rm mod}$, is defined as the fraction of the LW frequency interval, 11.5-13.6eV, that lies within the pickets, or that is successfully transmitted to the observer:

$$f_{\rm mod} = 1 - \sum_j \left(\frac{h\Delta\nu_{{\rm gap},j}}{2.1\ {\rm eV}}\right), \tag{2.8}$$

where $\Delta\nu_{{\rm gap},j}$ is the frequency interval between each picket in which there is no transmission. [3] The profile terminates at the 'LW horizon,' $r_{\rm LW} = 97.39\alpha$ cMpc, the distance at which a photon redshifts across the maximum picket spacing (between the pickets corresponding to the Lyδ and Lyγ lines). The scaling factor, α, is defined as:

$$\alpha = \left(\frac{h}{0.7}\right)^{-1}\left(\frac{\Omega_m}{0.27}\right)^{-1/2}\left(\frac{1+z}{21}\right)^{-1/2}. \tag{2.9}$$

While $f_{\rm mod}$ can be calculated numerically, [Ahn et al., 2009] have devised a fitting formula:

$$f_{\rm mod}(r) = 1.7\exp\left[-(r_{\rm cMpc}/116.29\alpha)^{0.68}\right] - 0.7$$

if $r_{\rm cMpc}/\alpha \leq 97.39$ and zero otherwise, where $r_{\rm cMpc}$ is the distance to the source in cMpc. We have successfully reproduced $f_{\rm mod}$ using the method described

[3] We implicitly assume a flat photon spectrum within the LW range here, which is a reasonable approximation over this short frequency interval.

by [Ahn et al., 2009] and have confirmed that the fitting formula is accurate to within 2 per cent error of the true numerical values.

2.3.1.1 The Light Cone

There is one difficulty with the halo model as usually constructed for our problem: it does not allow the sources to evolve over time. As usually constructed, the halo model takes the properties of each halo at a particular instant. This is not actually appropriate for our application, where the time delay from the finite speed of light implies that many sources will only be visible to a given point as they were long in the past, when their luminosity may have differed from the present value. For example, the light travel time across the LW horizon is 38.6 Myr at $z = 10$ and 11.1 Myr at $z = 25$. These values are a full $\sim 5\%$ of the Hubble time at those epochs, so a fraction of the visible sources would appear much dimmer than the above model would suggest. We next estimate how much we would expect the inclusion of such a time dependence to alter our results.

We can crudely account for halo growth by attaching a damping factor to the flux profile:

$$\rho_{\rm rad}(r|m) = L(m)\frac{f_{\rm mod}}{4\pi r^2} \longrightarrow L(m)\frac{f_{\rm mod}e^{-r/r_\star}}{4\pi r^2}, \tag{2.10}$$

where $r_\star = ct_\star(1+z)$ in cMpc and $t_\star$ corresponds to the typical timescale for halo growth, assuming that at these high redshifts the halos grow exponentially fast so that the luminosity of a halo $L(m) \propto \exp^{t/t_\star}$. The growth timescale we define as: $t_\star = a(z)t_{\rm H}$ (where a is some proportionality factor that evolves over time and $t_{\rm H}$ is the Hubble time).

To estimate a, consider a population of identical halos with mass m, at some redshift z, in which the halos are conserved; no new halos are created and none are destroyed. In this simple case, the collapse fraction is given by:

$$f_{\rm coll}(t) = \frac{n \cdot m(t)}{\bar{\rho}}. \tag{2.11}$$

Note how the halo mass is now a function of time, t. Taking the time derivative of this expression leads to:

$$\frac{1}{f_{\rm coll}(t)}\frac{df_{\rm coll}}{dt} = \frac{1}{m}\frac{dm}{dt} \equiv \frac{1}{t_\star}. \tag{2.12}$$

Thus for example, $a(z = 10) = 0.283, 0.167$ for $M_{\rm min} = 10^6{\rm M}_\odot, 10^8{\rm M}_\odot$ respectively and $a(z = 25) = 0.062, 0.034$ for the same choices of $M_{\rm min}$.

Although this simple model overestimates the growth rate of individual sources (because in reality much of the increase in collapse fraction is driven by new halos passing the relevant mass threshold), it provides a simple conservative parameterization of the effects of growth.

Adding this rapid source evolution effectively damps the source profile whenever $r_\star < r_{\rm LW}$ – these effects are illustrated in Figure 2.3.1. For example, for $M_{\rm min} = 10^8{\rm M}_\odot$, $r_\star(z = 10) = 401.6$ cMpc and $r_\star(z = 25) = 53.7$ cMpc while $r_{\rm LW} = 129.7$ cMpc and 84.4 cMpc for those respective redshifts. We include this crude model for the light cone effect below but also point out where it modifies our results substantially.

2.3.2 The Threshold Intensity

In order to determine when fluctuations are most important, we next compute the evolution of the LW intensity – and hence the point at which H_2 cooling is suppressed – in some simple models of structure formation. This section is not meant to provide a detailed model of star formation, but it should provide some context for the fluctuations we will later examine. We can estimate the mean LW intensity, $\bar{J}_{\rm LW}(z)$, with the following:

$$\bar{J}_{\rm LW}(z) = \frac{(1+z)^2}{4\pi}\int_z^{z+z_{\rm LW}} \frac{c dz'}{H(z')}\bar{\epsilon}(z') f_{\rm mod}(z'-z), \tag{2.13}$$

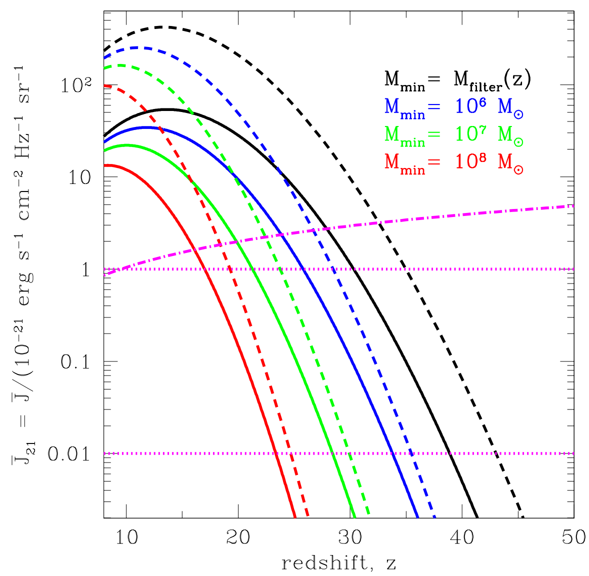

Figure 2.2: The mean intensities of the LW background (solid curves), $\bar{J}_{\mathrm{LW},21}$, and the Lyman-α background (dashed curves), $\bar{J}_{\alpha,21}$, for $M_{\mathrm{min}} = M_{\mathrm{filter}}$, $10^6\mathrm{M}_\odot$, $10^7\mathrm{M}_\odot$, and $10^8\mathrm{M}_\odot$ (right to left). Horizontal dotted lines indicate the upper and lower limits for the expected threshold value of $J_{\mathrm{LW},21}$. The dot-dashed line indicates the critical intensity for the Lyman-α background, $J^c_{\alpha,21}$ (see §2.4.2).

where $f_{\rm mod}(z'-z)$ is part of the LW flux profile (described more fully in §2.3.1) and the mean emissivity, $\bar{\epsilon}(z')$, is given by:

$$\bar{\epsilon}(z) = f_\star \bar{n}_b^0 \frac{d}{dt} f_{\rm coll}(z)\epsilon_b, \tag{2.14}$$

with $f_\star$ being the star forming efficiency (fraction of baryons that actually form stars), which we take to be 10% as a fiducial value, and $\bar{n}_b^0$ is the mean baryon number density. We can approximate the spectral distribution function (defined as the number of photons per frequency ν emitted per baryon), $\epsilon_b(\nu)$, as its mean value ϵ_b over the LW range (11.2–13.6 eV) for simplicity since we are looking at such a small range in frequency. We normalize $\epsilon_b(\nu)$ to produce 4800 photons per baryon between Lyman-α and the Lyman limit for very massive Population III.1 (zero-metallicity, $M \geq 100{\rm M}_\odot$) stars [Barkana and Loeb, 2005a]. Note that the light cone effect is inherent in this expression due to the redshift dependence of the mean emissivity.

Our results are summarized in Figure 2.2. The LW intensity is calculated in units of $J_{\rm LW,21} = J_{\rm LW}/(10^{-21}$ erg s^{-1} cm^{-2} Hz^{-1} sr^{-1}). The solid curves represent the very massive Population III stars. Replacing the emissivity with that of a Population II star (with metallicity equal to 1/20 the solar value) producing 9690 photons per baryon in our frequency range [Barkana and Loeb, 2005a] boosts the intensities by a factor of ~ 2; the background reaches threshold earlier. According to [Haiman et al., 2000], background intensities of $J_{\rm LW,21} \sim 10^{-2} - 1$ are needed to suppress H_2 cooling in all minihalos over a range of redshift from $z \sim 10-50$. The lower value describes H_2 suppression in halos near the $T_{\rm vir} < 10^{2.4}$ K limit; below these low temperatures H_2 cooling is inefficient even in the absence of any photodissociating background, so no stars will form. Since $f_{\rm H_2}$ increases with $T_{\rm vir}$, it will be more difficult to terminate a more massive halo's larger cooling supply. Thus, as the halo population evolves, becoming more numerous and more massive with time, the threshold intensity must increase, self-regulating star formation by shifting the minimum mass to higher values. Once halos reach $T_{\rm vir} > 10^{3.8}$ K the value of the background intensity is once again irrelevant since these large halos are able to cool via atomic line cooling and no longer rely on their fragile H_2 supply. In further calculations, we will take $J_{\rm LW,21} = 0.1$ as our fiducial threshold intensity.

It is evident from Figure 2.2 that our models reach this threshold between redshifts $z \sim 15 - 35$. Of course, these models are extremely naive and ignore a host of complications (such as the evolving star formation efficiency and cooling threshold, as well as other feedback mechanisms). But they suffice to illustrate approximately when a given model reaches the H_2 photodissociation threshold, where the fluctuations which we will study are particularly interesting. Note that, because structure formation itself proceeds exponentially fast at high redshifts, uncertainties in the star formation parameters themselves are relatively unimportant. In any case, $J_{\rm LW,21} \propto f_\star \epsilon_b$, so it is easy to read off the appropriate intensity for such a model.

We emphasize that the fluctuations will be most important near the threshold, because that is when the transition in cooling modes actually occurs. If fluctuations are small, the transition would occur uniformly over the entire Universe. If not, the Universe could contain isolated, sparsely populated patches in which H_2 cooling remains possible. If a minihalo inhabits one of these 'safe' patches, it could continue to form very massive stars via H_2 cooling even after the mean intensity reaches threshold. On the other hand, even well before an average IGM point reaches threshold, regions near existing sources will be well above it, and this could strongly affect the highly-clustered early sources. We will examine this phase in §2.3.4.

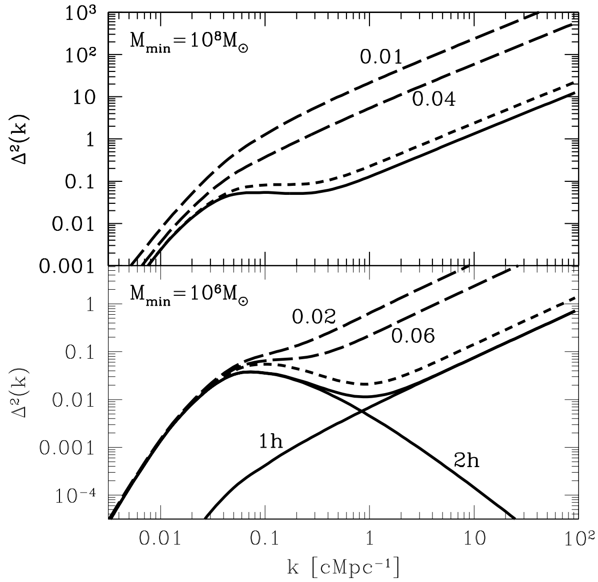

Figure 2.3: Power spectrum of the LW background, $\Delta^2(k)$ for scenarios normalized to reach $J_{\rm LW,21} = 0.1$. Scenarios include: $M_{\rm min} = 10^6{\rm M}_\odot$, $z = 30.15$ (bottom panel) and $M_{\rm min} = 10^8{\rm M}_\odot$, $z = 20.5$ (top panel). The light cone versions for both scenarios are also shown (short-dashed curves) while the original versions are the solid curves. For the $M_{\rm min} = 10^6{\rm M}_\odot$ curve we have shown not only the total spectrum but also the one-halo (labeled '1h') and two-halo (labeled '2h') contributions for visual aid (see equation 3.49). The two, topmost, long-dashed curves represent the light cone scenarios with the duty cycle taken into account. The $M_{\rm min} = 10^6{\rm M}_\odot$ model includes two different values for this: $f_{\rm duty} = 0.02$ (topmost curve, labeled 0.02) and $f_{duty} = 0.06$ (second curve, labeled 0.06). The $M_{\rm min} = 10^8{\rm M}_\odot$ case also includes two curves for $f_{\rm duty} = 0.01$ and 0.04.

2.3.3 Power Spectrum

Results are depicted in Figures 2.3 and 2.4. In the former, we simultaneously vary $M_{\rm min}$ and redshift so that $J_{\rm LW,21} = 0.1$ is fixed, while in the latter we follow a single star formation model over redshift (varying $L_{\rm LW,21}$).

The normalized scenarios displayed in Figure 2.3 include: $M_{\rm min} = 10^6 {\rm M}_\odot$, $z = 30.15$ (bottom panel) and $M_{\rm min} = 10^8 {\rm M}_\odot$, $z = 20.5$ (top panel). The short-dashed curves represent the light cone versions for both scenarios, using equation (2.10) for the flux profile. It is evident that the inclusion of the light cone effect preserves the shape of the power but modestly boosts the amplitude (by a factor of ~ 2). We have also separately displayed the 1-halo and 2-halo terms (bottom-most, solid lines) for the $M_{\rm min} = 10^6 {\rm M}_\odot$ scenario so as to gain a sense of when these terms are dominant and to show how they work in tandem to determine the shape of $\Delta^2(k)$.

It is important to note that the above prescriptions assume that all halos above the mass threshold, $M_{\rm min}$, form stars continuously. Of course, these stars have finite lifetimes, and in the classical Pop III scenario in which each halo undergoes only a short burst of star formation, not all of these stars are going to be 'turned on' when we take a snapshot of the fluctuations at a particular point in time. We can account for this simply by incorporating a duty cycle, $f_{\rm duty}$, into our calculation. This addition exclusively affects the one-halo term in equation 3.49; since both $n(m)$ and the effective $f_{\rm coll}$ (which in this model gives the fraction of halos hosting *active* sources) are altered by a factor of $f_{\rm duty}$, the two-halo term remains unchanged.

The two topmost, long-dashed curves in both panels of Figure 2.3 represent the $M_{\rm min} = 10^8 {\rm M}_\odot$ and $10^6 {\rm M}_\odot$ scenarios including the light cone effect using two different values of $f_{\rm duty}$. A reasonable estimate for $f_{\rm duty}$ would be the ratio between the average lifetime of a Pop III star, τ, and the Hubble time, $t_{\rm H}$. The lifetime of these massive stars is believed to be a few million years (Myrs) [Barkana and Loeb, 2001b, Bromm and Larson, 2004], though that remains to be directly measured. The topmost curve in both cases assumes an average lifetime of $\tau \sim 3$ Myrs ($f_{\rm duty} = 0.02$ for $M_{\rm min} = 10^6{\rm M}_\odot$ and 0.01 for $M_{\rm min} = 10^8{\rm M}_\odot$) while the second curve assumes $\tau \sim 10$ Myrs ($f_{\rm duty} = 0.06$ and 0.04 for $M_{\rm min} = 10^6{\rm M}_\odot$ and $10^8{\rm M}_\odot$ respectively). This greatly increases the importance of the one-halo term and so boosts the fluctuations on scales below the LW horizon. However, note that the mean background intensity also falls by a factor of $f_{\rm duty}$, so these strong fluctuations occur well *before* threshold is reached.

The most striking feature common to all power spectra is the first turnover located at $k_{\rm LW} \sim 0.06$ cMpc^{-1}. This is a strong signature of the LW flux profile, which terminates at $r_{\rm LW} \sim 100$ cMpc ($k_{\rm LW} = 2\pi/r_{\rm LW} \sim 0.06$ cMpc^{-1}). Power is smallest for the largest scales and then steadily increases until it reaches $k_{\rm LW}$. In this regime, regions are far outside the LW horizon of each source and so sample independent patches in the radiation field. The total power is therefore simply proportional to the matter power spectrum multiplied by a mean bias factor (squared). However, at $k_{\rm LW}$, Δ^2 turns over and begins to fall. This is because such scales sample the variations within $r_{\rm LW}$; if the two points see the same halo populations, their radiation amplitudes will vary together and the fluctuations decrease. On the smallest scales the power turns up and increases monotonically. This indicates where the $P^{1\rm h}(k)$ term becomes dominant, which occurs on larger scales (smaller k) for increasing choice of $M_{\rm min}$ because the sources become more rare.

Note how the signature shifts to slightly higher k in the light cone versions, because the damping scale $r_\star < r_{\rm LW}$. The turnover is also smoothed out as $M_{\rm min}$ increases and the one-halo component begins to dominate at larger scales. This signature is further smoothed by accounting for the duty cycle. The shorter the stellar lifetime (and the smaller the duty cycle), the more amplified the one-halo

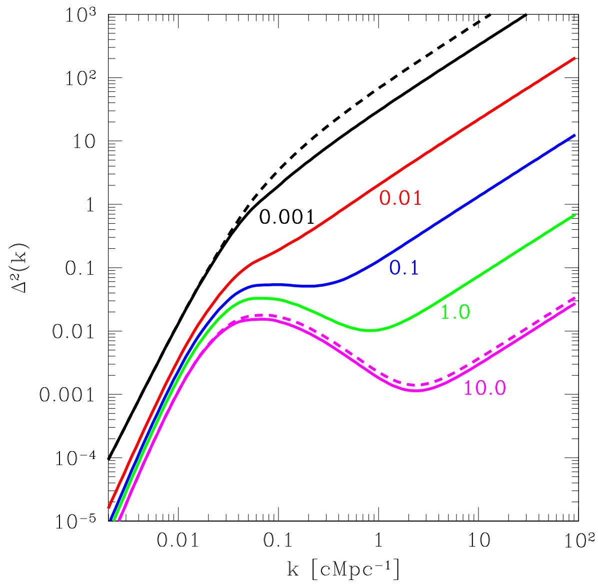

Figure 2.4: Power spectrum of the LW background, $\Delta^2(k)$, for our $M_{\rm min} = 10^8 {\rm M}_\odot$ scenario, which reaches threshold $J_{\rm LW,21} = 0.1$ at $z = 20.5$. The curves show the power at different redshifts in the same model: $J_{\rm LW,21} \sim 0.001$, 0.01, 0.1, 1, and 10 (corresponding to $z = 25.8$, 23.35, 20.5, 17.0, and 11.05 from top to bottom). We display the time dependent versions (dashed curves) for the first and last of these.

term will be relative to the unchanged two-halo contribution.

Figure 2.4 shows the $M_{\rm min} = 10^8 {\rm M}_\odot$ scenario at several different redshifts. Curves are labeled according to their normalized $J_{\rm LW,21}$ values. The central curve (blue in the online version) corresponds to the $J_{21} \sim 0.1$ normalized version (z=20.5). Apparent in Figure 2.4 is the washing out of the turnover at increasing z; at high z halos are more rare and the LW background patchier – consequently the 1-halo term begins to dominate earlier on scales $k < k_{\rm LW}$, thus smoothing out the key signature.

One important caveat for our model is the assumption of linear bias when computing the 2-halo term in the power spectrum. For example, consider the

$M_{\rm min} = 10^8$ $M_\odot$ model, which reaches threshold at $z \sim 20$. At that time, such a halo has $b \sim 10$. Thus, even though the rms density fluctuation on ~ 5 Mpc scales is ~ 0.04, the halo fluctuations are $\sim b\sigma \sim 0.4$, where nonlinear effects are becoming important. The steep intensity profiles around these sources make clustering somewhat more important for the radiation background, as found by [Mesinger and Furlanetto, 2009], and probably enhance the fluctuations on moderately small scales by a factor of a few. For example, [Mesinger and Furlanetto, 2009] found from semi-numeric simulations that nonlinear clustering tends to smooth out the signature turnover in the power spectrum of the ionizing background (where it is due to the smaller attenuation length of high-z ionizing photons); see also the discussion in §2.3.5 below.

As discussed in § 2.3.2, we assumed $f_\star = 0.1$ here. This is likely to be an upper limit, and it could be much smaller if, for example, the first star to form in each halo suppresses the formation of any others. In this case the radiation field would not reach threshold until *later*, when there are many more halos and hence smaller fluctuations. Our scenarios therefore provide upper limits to the fluctuation amplitude at threshold.

Given the unusual shapes of these power spectra, we next compute the real-space standard deviation in the intensity to provide better intuition for the amplitude of these fluctuations. We calculate the fractional standard deviation, $\sigma(R)$, in the following way:

$$\sigma^2(R) = \int dk \frac{k^2}{2\pi^2} P(k) W_R^2(k), \tag{2.15}$$

where $W_R^2(k)$ is the 'window function' or smoothing window over which we consider varying $P(k)$. We employ a simple Gaussian window for computational simplicity:

$$W_R(k) = e^{-k^2R^2/2}. \tag{2.16}$$

We display $\sigma(R)$ in Figure 2.5 for the choice of $M_{\rm min} = 10^8 M_\odot$. From top to bottom, the solid curve is normalized to $10^{-5} J_{21}$ ($z = 30.0$), while the others have

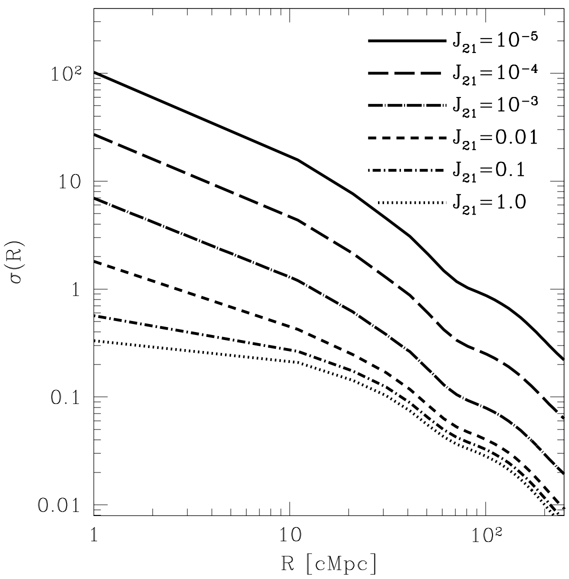

Figure 2.5: The fractional standard deviation, $\sigma(R)$, of the LW background depicted for $M_{\rm min} = 10^8 \rm M_{\odot}$. From top to bottom: the solid curve is normalized to $10^{-5} J_{21}$ ($z = 30$), the long-dashed curve to $10^{-4} J_{21}$ ($z = 28$), the dot-long–dashed curve to $10^{-3} J_{21}$ ($z = 25.8$), the short-dashed curve to $0.01 J_{21}$ ($z = 23.4$), the dot-short-dashed curve to $0.1 J_{21}$ ($z = 20.5$), and the dotted curve to $1.0 J_{21}$ ($z = 17.0$). We take $f_\star = 0.1$ in these scenarios.

$J_{\rm LW,21} = 10^{-4},\ 10^{-3},\ 0.01,\ 0.1$, and 1.

The signature turnover at $k_{\rm LW}$ (see Figures 2.3 and 2.4) has been lightly imprinted onto the shape of $\sigma(R)$ in the form of a gentle kink at $R \sim 100$ cMpc. It is evident that at intensity levels nearly approaching, at, and beyond the threshold value, $\sigma(R)$ is small (< 1) down to very small scales (~ 1 cMpc), indicating a fairly uniform background. This suggests that it is unlikely for isolated patches still harboring H_2 to exist and foster star-forming minihalos around the threshold.

2.3.4 Fluctuations in the Background at Early Phases

Nevertheless, Figure 2.5 shows that fluctuations in the background are large early on when $J_{\rm LW}$ is well below threshold; $\sigma(8\ {\rm cMpc}) \sim 20$ for $M_{\rm min} = 10^8 {\rm M}_\odot$ at $z = 30$. On the flip side of asking whether or not scattered H_2 driven star formation could persist in epochs close to or at threshold, these large fluctuations could indicate that even in epochs for which the background is substantially below threshold there will be patches that are locally at threshold in which H_2 cooling is suppressed.

However, in this regime the fluctuations are not gaussian, so the standard deviation σ is not a good representation of the importance of the fluctuations. Moreover, because we primarily care about the radiation intensity at highly clustered sites of other halos – where star formation is trying to occur – simply taking a pure spatial average is not necessarily the proper approach (see also [Dijkstra et al., 2008]).

In order to delve into this new question, we follow the method presented in [Furlanetto and Loeb, 2005] with which they calculated the probability that a collapsing halo forms in a region already enriched by galactic winds at high redshift. In contrast, we are interested in calculating the probability that a collapsing halo forms in a region with a LW background above the dissociation threshold. If the sources are very rare, this corresponds to lying within a radius $R_{\rm thres}$ of a

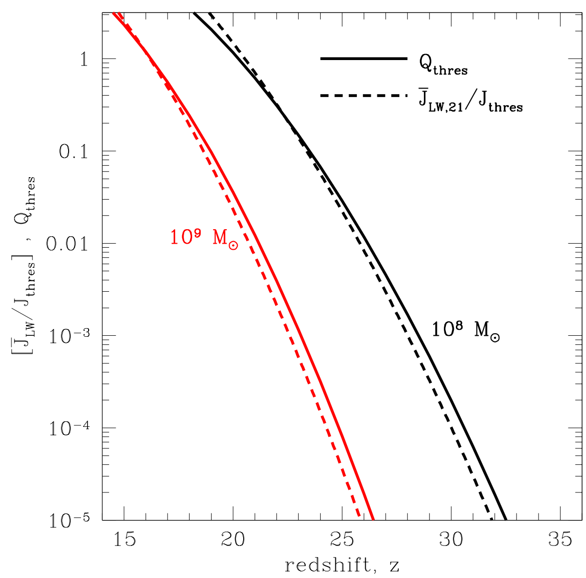

Figure 2.6: The probability, $Q_{\rm thres}$ (solid curves), that a new halo forms within $R_{\rm thres}$ of an existing halo, or within the region irradiated by a local LW intensity above the threshold for H_2 suppression. Scenarios include $M_{\rm min} = 10^8 M_\odot$ (rightmost, black curves) and $M_{\rm min} = 10^9 M_\odot$ (leftmost, red curves). Also displayed is the mean LW intensity in units of the threshold level, $\bar{J}_{\rm LW,21}/J_{\rm thres}$, using $f_\star = 0.1$ and $J_{\rm thres} = 0.1 J_{21}$.

LW emitting halo. Within this radius, the 'new' halo – one that has passed the threshold to form stars – is irradiated by a local LW intensity above the threshold value for suppressing H_2 cooling. We can start by calculating the fraction of space contained within $R_{\rm thres}$ of all LW emitting halos, $Q'_{\rm thres}(z)$, assuming that these regions do not overlap:

$$Q'_{\rm thres}(z) = \int_{M_{\rm min}}^{\infty} dm \left(\frac{m}{\bar{\rho}}\right) \eta(m) n(m), \tag{2.17}$$

where $\eta(m)$ is the ratio of mass irradiated within $R_{\rm thres}$ of a halo with mass m to that halo's mass:

$$\eta(m) = \frac{4\pi\bar{\rho}R_{\rm thres}^3/3}{m}. \tag{2.18}$$

For example, for a halo of mass $10^8 {\rm M}_\odot$ at $z = 20$ with $M_{\rm min} = 10^8 {\rm M}_\odot$ and $f_\star = 0.1$, $R_{\rm thres} \sim 3$ cMpc and $\eta \sim 5.5 \times 10^4$. The corresponding values for $z = 30$ are $R_{\rm thres} \sim 8$ cMpc and $\eta \sim 9.7 \times 10^5$. If the flux profile were a pure $1/r^2$ power law, then $R_{\rm thres} \propto L^{1/2}$, so $\eta \propto m^{1/2}$. In reality, the modulation factor steepens the flux profile, so η is closer to flat.

In the limit in which sources are truly isolated, $Q'_{\rm thres}$ would be the total filling factor of threshold regions. However, as more sources appear, their regions will begin to overlap and – because η is an increasing function of m – grow faster. Because we are only after a crude estimate of this effect, we do not worry about overlap here and use $Q'_{\rm thres}$ as our fiducial estimate. A more sophisticated numerical or Monte Carlo model can easily incorporate this possibility [Dijkstra et al., 2008]. The model will, of course, break down when sources become common enough to sit within each other's $R_{\rm thres}$ (indeed, $Q'_{\rm thres}$ is not limited to be less than unity). Fortunately, in this regime near threshold the halo model approach is perfectly adequate.

Since the newly forming halos are spatially biased and preferentially collapse near existing halos, this expression is not entirely correct. If we consider two halos, the first a newly formed halo and the second an established LW emitting halo, then the excess probability that the two halos live near each other is quantified by the correlation function, $\xi_{\rm gg}$. To linear order, the correlation function can be written as $\xi_{\rm gg} = b_{\rm new}\bar{b}_{\rm thres}\xi_{\delta\delta}$, where $b_{\rm new} = b(M_{\rm min})$ and $\bar{b}_{\rm thres}$ are the biases of the newly collapsed and LW threshold region respectively and $\xi_{\delta\delta}$ is the dark matter correlation function. The mean bias of the LW threshold regions surrounding established halos can be written as:

$$\bar{b}_{\rm thres} = \frac{\int dmm\eta(m)b(m)n(m)}{\int dmm\eta(m)n(m)}. \tag{2.19}$$

With this in mind, we can approximate the corrected probability that a new halo lives within $R_{\rm thres}$ of an established halo as:

$$Q_{\rm thres} = Q'_{\rm thres}\left[1 + b_{\rm new}\bar{b}_{\rm thres}\xi_{\delta\delta}(R_{\rm thres})\right]. \tag{2.20}$$

We found that these corrections typically boost $Q'_{\rm thres}$ by a factor of ~ 2 in our scenarios.

Figure 2.6 shows $Q_{\rm thres}$ for a choice of $M_{\rm min} = 10^8 {\rm M}_\odot$ (rightmost, solid black curves) and $M_{\rm min} = 10^8 {\rm M}_\odot$ (leftmost, solid red curves) with $f_\star = 0.1$. The dashed curves in Figure 2.6 represent the mean intensity relative to threshold, $\bar{J}_{\rm LW,21}/J_{\rm thres}$. $Q_{\rm thres}$ increases as redshift decreases and the LW background builds up and becomes more uniform in both scenarios. It is evident from Figure 2.6 that increasing the choice of $M_{\rm min}$ delays H_2 suppression; increasing $M_{\rm min}$ from $10^8 {\rm M}_\odot$ to $M_{\rm min} = 10^9 {\rm M}_\odot$ decreases $Q_{\rm thres}$, for example, by a factor of ~ 33 at $z \sim 20$. By increasing the mass threshold one eliminates contributions from a host of less massive potential sources, requiring more time for the background to strengthen and boost $Q_{\rm thres}$. Identical calculations using $f_\star = 0.01$ yield values of $Q_{\rm thres}$ that are up to factors of ~ 15 smaller.

Also, note that $Q_{\rm thres}$ increases roughly in proportion to $\bar{J}_{\rm LW}$: evidently the mean background provides a good estimate of the volume illuminated by a high intensity of LW radiation. However, note that the quantitative similarity of this filling factor and $\bar{J}_{\rm LW}/J_{\rm thres}$ shown in Fig. 2.6 is coincidental and does not occur if we, e.g., change our choice of threshold value or $f_\star$.

Once $J_{\rm LW,21}$ reaches threshold, $Q_{\rm thres} \sim 1.2$ (for $M_{\rm min} = 10^8 {\rm M}_\odot$ and $f_\star = 0.1$). At earlier times, the discrete nature of the sources does substantially increase the probability for a new halo to lie within a threshold region over and above what one might naively guess from Figure 2.5; for example, when $J_{\rm LW} \sim 0.1 J_{\rm thres}$, $\sim 15\%$ of the halos lie in this regime, even though $\sigma < 1$ down to very small scales. Nevertheless, we still find that at early times there are relatively few patches above threshold.

2.3.5 Comparison to Other Work

There has been relatively little work on fluctuations in the LW background at high redshifts. The most salient comparison is to [Ahn et al., 2009], who calculated the LW background power spectra using a large-scale radiative transfer simulation with size $R_{\rm box} \sim 50$ cMpc. They resolved halos down to $10^8 {\rm M}_\odot$ and implemented a simple two-population model for galaxies, in which halos with $M < 10^9 {\rm M}_\odot$ had large ionizing efficiencies and larger halos had more modest efficiencies. By following the radiative transfer of ionizing photons, they also included the suppression of galaxy formation in halos with $M < 10^9 {\rm M}_\odot$ following reionization, so this higher-efficiency population gradually disappeared.

Although this simulation box should be sufficiently large to include a fair sample of the halo population,[4] it is still much smaller than $r_{\rm LW}$. [Ahn et al., 2009] therefore used a periodic tiling in order to fill out the LW horizon. Unfortunately, this means that they cannot measure the turnover at $k_{\rm LW}$, nor the regime in which the two-halo component dominates and approaches the straightforward limit $b^2 P^{\rm lin}$, so interpreting their results is somewhat difficult.

[4] According to the methods of [Barkana and Loeb, 2004], the missing large-scale modes only suppress the halo population by a few percent.

We are unable to implement the self-regulated reionization model used by [Ahn et al., 2009] in our simpler analytic model, but we have nevertheless made several test calculations to compare our results, choosing a reasonable minimum mass to match theirs at the different redshifts. Fortunately, [Ahn et al., 2009] find that their simulation reaches threshold at $z \approx 16$, when the ionized fraction is less than a percent – thus we do not expect the self-regulation to be important in the regime of most interest. On the other hand, their box has only one radiation source at $z = 19$, so the pre-threshold regime probably suffers from their finite box size even more than expected.

Comparing to their Figure 12, we find less power, by an order of magnitude or so, in the $k \sim 0.3$–20 Mpc^{-1} regime probed by their simulations, from $z \sim 16$–8. (They provide only an upper limit at higher redshifts because of the many fewer sources in the box.) However, our model does help to explain the *shape* of their power spectrum, which (when converted to Δ^2) shows relatively flat power over this range, especially at the lower redshifts. This is because it lies between the turnover at $k_{\rm LW}$ and the regime in which the one-halo term dominates (see, e.g., the lower-redshift curves in our Fig. 2.4). The flattening becomes more pronounced at lower redshifts as the one-halo term decreases in importance, thanks to the increased source density.

Nonlinear clustering is one likely explanation for the different amplitudes: the simulations can include the fully nonlinear clustering of these sources, while our model ignores them. [Mesinger and Furlanetto, 2009] did indeed find a boost of power on comparable scales comparing a halo-model implementation of radiation fluctuations to semi-numeric simulations (in this case, the ionizing background at $z \sim 6$). However, they found a much more modest boost (a factor ~ 2), followed by a steepening toward much smaller scales relative to the halo model prediction. Reconciling our results with those of [Ahn et al., 2009] requires a much larger effect. One possible explanation is the amplitude of the source fluctuations, which is ~ 2 times larger in the [Ahn et al., 2009] model at $z = 20$ than in the [Mesinger and Furlanetto, 2009] comparison, because the much higher bias of the higher-redshift halos compensates for the smaller fluctuations in the density field.

Another possible explanation is the finite source lifetimes imposed in the numerical simulations, which decreases the number of sources in the box and increases the importance of the one-halo term [Ahn et al., 2009, Iliev et al., 2007], albeit in a non-uniform manner within the numerical simulation.

In any case, however, both the simulations and analytic models agree that, before the threshold is reached, fluctuations are relatively unimportant. The large-scale uniformity of the background seems robust, in the absence of large-scale modulation to the source population itself (as may be provided by relative velocities between baryons and dark matter; [Tseliakhovich and Hirata, 2010]).

In principle, we can also compare our model with the detailed Monte Carlo simulations of [Dijkstra et al., 2008]. However, they focus exclusively on times far beyond threshold and very close halo pairs, where our crude approximation no longer applies.

2.4 The Lyman-α Background

The Lyman-α background imprints fluctuations onto the 21-cm signal [Barkana and Loeb, 2005a] by way of the Wouthuysen-Field effect [Wouthuysen, 1952, Field, 1958] in which the two hyperfine states of neutral hydrogen are mixed via the absorption and reemission of a Lyman-α photon. Once the first sources in the universe turn on and amalgamate into a Lyman-α background, this effect drives the spin temperature, T_S, to the gas temperature, T_K, resulting in a nonzero brightness temperature relative to the CMB, T_b, and allowing the 21-cm line to become visible. We can write T_b as [Furlanetto et al., 2006]:

$$T_b(\nu) \approx 9 x_{\rm HI}(1+\delta)(1+z)^{1/2} \left[1 - \frac{T_\gamma(z)}{T_S}\right] \left[\frac{H(z)/(1+z)}{dv_\parallel/dr_\parallel}\right] \ \mathrm{mK}, \tag{2.21}$$

where $x_{\rm HI}$ is the neutral fraction, $(1+\delta)$ is the fractional overdensity of baryons, $T_\gamma(z) = 2.73(1+z)$ K is the brightness temperature of the CMB, and $dv_\parallel/dr_\parallel$ is the gradient of the proper velocity along the line of sight. We can relate T_γ/T_S to T_γ/T_K with [Furlanetto et al., 2006]:

$$\left[1 - \frac{T_\gamma(z)}{T_S}\right] = \frac{x_c + x_\alpha}{1 + x_c + x_\alpha} \left[1 - \frac{T_\gamma(z)}{T_K}\right], \tag{2.22}$$

where x_c and x_α are the collisional and Lyman-α scattering coupling coefficients.

Observing the 21-cm signal could provide us a window with which to investigate properties of the exotic sources that collectively shaped the nature of this background. This means that the Lyman-α background is a directly observable effect of (nearly) the same photons that make up the LW background. This allows us to measure that feedback process directly rather than having to infer it from modeling star formation in halos, which is quite difficult.

2.4.1 The Flux Profile

Our construction of the Lyman-α flux profile follows
[Pritchard and Furlanetto, 2006]. To calculate the Lyman-α flux originating from a particular source one must consider contributions from all Lyn levels. After absorption (and ignoring recombinations directly to the ground state, which just regenerate the original photons), a fraction, $f_{\rm recycle}$ [Hirata, 2006], of Lyn photons will be converted into Lyman-α photons via cascades through a series of radiative transitions and will contribute to the total observed Lyman-α flux. The remainder will wind up in the metastable $2s$ configuration and decay via two-photon emission, resulting in no Lyman-α photon. We use the values of $f_{\rm recycle}$ presented in [Pritchard and Furlanetto, 2006]. For example, $f_{\rm recycle} = 0.2609, 0.3078$ for

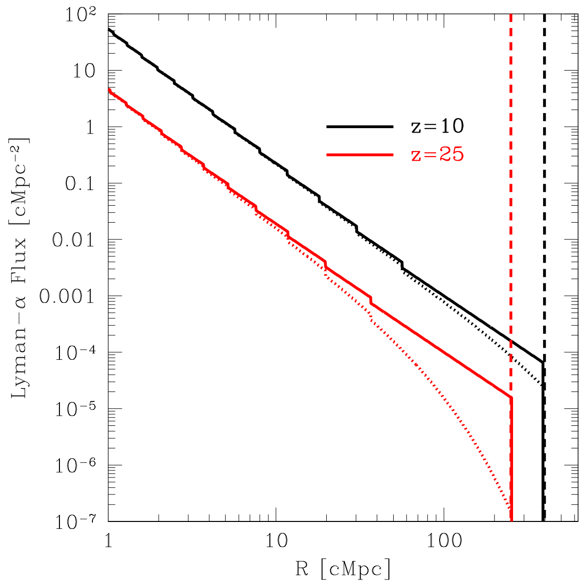

Figure 2.7: The Lyman-α flux profile shown for $z = 10$ (black, top curve) and 25 (red, bottom curve) with $M_{\rm min} = 10^8 \rm M_\odot$. The light cone versions are displayed as dotted curves and the corresponding dashed vertical lines indicate the Lyman-α horizons. The $z = 10$ curve is displaced by a factor of 10 to make it more visible.

$n = 4, 5$ respectively. At large n, $f_{\rm recycle}$ asymptotes to a value of ~ 0.36. However we note that quantum selection rules ($\Delta L = \pm 1$) forbid a Lyman-β photon from producing a Lyman-α photon.

Since a source can only be separated from the observer by a finite distance before its photons redshift into their nearest Lyn transitions, a photon received at redshift z as a Lyn photon must have been emitted below redshift $z_{\rm max}$:

$$1 + z_{\rm max}(n) = (1+z)\frac{[1-(n+1)^{-2}]}{(1-n^{-2})}. \tag{2.23}$$

This imprints a set of horizons on the flux profile; horizons become smaller and smaller as you consider higher Lyn levels. The series of horizons results in a step-like structure of the overall profile. We assume the flux from one halo takes the following form:

$$F_{\rm Ly\alpha} \propto \frac{m}{4\pi r^2}\sum_{n}^{n_{\rm max}} \epsilon_{b,\alpha}(\nu'_n) f_{\rm recycle}(n) \tag{2.24}$$

where $\epsilon_{b,\alpha}(\nu)$ is the spectral distribution function (defined as the number of photons per baryon emitted at frequency ν per unit frequency) described by a power law $\epsilon_b(\nu) \propto \nu^{\alpha_s - 1}$. We use the values for α_s presented in [Barkana and Loeb, 2005a] for massive Population III stars and Population II stars. A photon emanating from the source at emission frequency, ν'_n, located at redshift z' is absorbed by level n at redshift z:

$$\nu'_n = \nu_n \frac{(1+z')}{(1+z)}. \tag{2.25}$$

The sum is ultimately truncated at $n_{\rm max} = 23$ to exclude levels for which the horizon lies within the HII region of a typical (isolated) galaxy [Barkana and Loeb, 2005b].

The Lyman-α flux profiles for $z = 10$ (top curve) and 25 (bottom curve) are displayed in Figure 2.7. We normalize the curves arbitrarily here in order to focus on the shape as a function of redshift. The Lyman-α horizon distance, $r_{\rm Ly\alpha}$, corresponds to the distance over which a Lyman-β photon would redshift into the Lyman-α resonance. This is the maximum range a photon can travel and become a Lyman-α photon; at $z = 10$ and 25, $r_{\mathrm{Ly}\alpha} \sim 390$ and 254 cMpc respectively. In comparison, the LW horizons for those redshifts are ~ 130 and 84 cMpc respectively. We can therefore expect *smaller* fluctuations in the Lyman-α background than in the LW background. However, note that the difference is not as large as one might otherwise expect because the delay from the light travel time already reduces the importance of distant sources.

The dotted curves represent the light cone corrected profiles; we treat the light cone effect in the same fashion that we amended the LW profile in §2.3.1.1. As can be seen in Figure 2.7, the light cone curves begin to diverge from the original version on scales $R > 10$ cMpc. The final and largest 'step' (and more and more of the smaller steps as you look at higher redshift) in the profile is effectively beveled as the flux begins to prematurely slope downward until it runs into the horizon. This difference morphs the shape of the power spectrum as discussed further in §2.4.3.

2.4.2 The Mean 21-cm Background

We next estimate the redshifts for which the Lyman-α background fluctuations are important when observing the 21-cm signal. Following [Furlanetto et al., 2006] we can write the fractional variation of the brightness temperature of the 21-cm line, δ_{21}, in the following way:

$$\delta_{21} = \beta\delta_b + \beta_\alpha\delta_\alpha - \delta_{\partial_v}, \tag{2.26}$$

where δ_b is the perturbation in the baryonic density, δ_α is that for the Lyman-α coupling coefficient x_α, and δ_{∂_v} is that for the line of sight peculiar velocity gradient. The expansion coefficients, β_i, and their evolution over time determine the epochs for which the various perturbations influence the fluctuations in T_b. In particular,

$$\beta = 1 + \frac{x_c}{x_{\rm tot}(1+x_{\rm tot})} \tag{2.27}$$

and

$$\beta_\alpha = \frac{x_\alpha}{x_{\rm tot}(1+x_{\rm tot})}. \tag{2.28}$$

β_α is basically the fractional contribution of the Wouthuysen-Field effect [Wouthuysen, 1952, Field, 1958] to the coupling, where $x_{\rm tot} \equiv x_c + x_\alpha$ and x_c and x_α are the coupling coefficients for collisions and Lyman-α scattering. For simplicity in our calculations, and for easy comparison to earlier work [Barkana and Loeb, 2005a, Pritchard and Furlanetto, 2006], we ignore all fluctuations except for those due to density ($\beta\delta_b$) and the Lyman-α background ($\beta_\alpha\delta_\alpha$). We neglect perturbations in the neutral fraction ($\beta_x\delta_x$) and the gas kinetic temperature, T_K ($\beta_T\delta_T$).

The collisional coupling coefficient was calculated as in [Furlanetto, 2006]. The Lyman-α coupling coefficient can be written as

$$x_\alpha = S_\alpha \frac{J_\alpha}{J_\alpha^c}, \tag{2.29}$$

where S_α is a correction factor of order unity [Chen and Miralda-Escudé, 2004, Hirata, 2006, Pritchard and Furlanetto, 2006] that we neglect in our simple model and J_α is the mean Lyman-α intensity. In a similar fashion to equation (2.13), J_α is given by:

$$J_\alpha(z) = \sum_{n=2}^{n_{\rm max}} \int_z^{z_{\rm max}(n)} dz' f_{\rm recycle}(n) \frac{(1+z)^2}{4\pi} \frac{c}{H(z')} \epsilon(\nu_n', z'). \tag{2.30}$$

The critical intensity, $J^c_{\alpha,21} = 0.66[(1+z)/20]$ (in the units of J_{21}), corresponds to the threshold level of J_α for which T_S sticks to T_K [Furlanetto et al., 2006, Chen and Miralda-Escudé, 2004]. How does this threshold intensity compare to the LW intensity at which H_2 cooling is suppressed? We have displayed J_α^c in

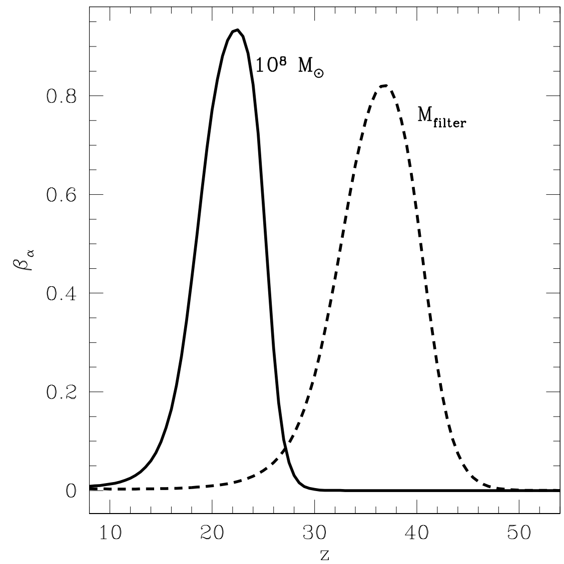

Figure 2.8: The Lyman-α coupling coefficient, $\beta_\alpha(z)$, for $M_{\rm min} = M_{\rm filter}$ (dashed line) and $10^8 {\rm M}_\odot$ (solid line), assuming $f_\star = 0.1$.

units of J_{21} as the dot-dashed line in Figure 2.2. The dashed curves in Figure 2.2 represent the calculated average Lyman-α intensities for scenarios with $M_{\rm min} = M_{\rm filter}(z)$, $10^6{\rm M}_\odot$, $10^7{\rm M}_\odot$, and $10^8{\rm M}_\odot$ and $f_\star = 0.1$. Notice how these intensities are larger than their LW counterparts (solid curves); the Lyman-α horizon distance is a factor of ~ 3 times larger than the LW horizon, which not only allows the Lyman-α background to build up more quickly but also allows for a more uniform background, as discussed in § 2.4.1.

Around the time that the LW intensity reaches threshold for H_2 suppression, J_α is also somewhat higher than that, and hence very close to J_α^c. As a result, the 21-cm background is directly sensitive to the physics of cooling; around the time when T_S sticks to T_K numerous minihalos are shutting down stellar production as their H_2 supplies are wiped out. Conveniently, this makes the 21-cm background a nearly direct probe of this very interesting epoch in the history of galaxy formation.

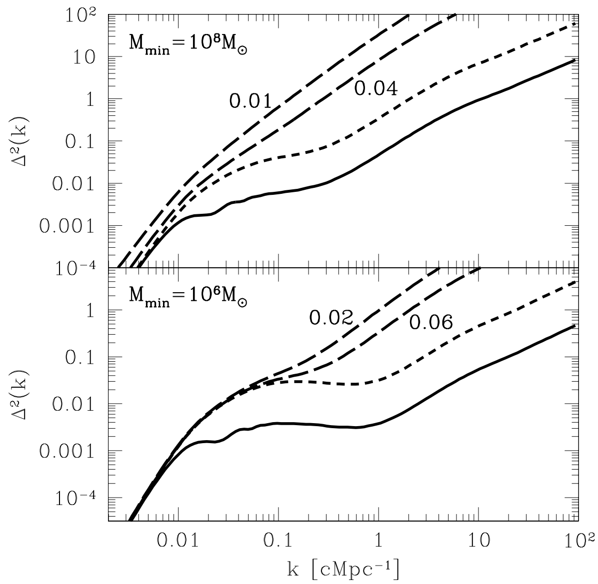

Figure 2.9: Power spectrum of the Lyman-α background, $\Delta^2(k)$, for scenarios normalized to reach $J_{\mathrm{LW},21} = 0.1$ for ease of comparison with Fig. 2.3. Scenarios include: $M_{\mathrm{min}} = 10^6 \mathrm{M}_\odot$ at $z = 30.15$ (bottom panel) and $M_{\mathrm{min}} = 10^8 \mathrm{M}_\odot$ at $z = 20.5$ (top panel). The light cone versions for both scenarios are also shown (short-dashed curves) while the original versions are the solid curves. The two, topmost, long-dashed curves include the light cone effect and duty cycle for the $M_{\mathrm{min}} = 10^8 \mathrm{M}_\odot$ case ($f_{\mathrm{duty}} = 0.01$ and 0.04; labeled 0.01 and 0.04 respectively) and the $M_{\mathrm{min}} = 10^6 \mathrm{M}_\odot$ case ($f_{\mathrm{duty}} = 0.02$ and 0.06).

We present $\beta_\alpha(z)$ in Figure 2.8 for $M_{\mathrm{min}} = 10^8 \mathrm{M}_\odot$ and $f_\star = 0.1$. We find that, for $M_{\mathrm{min}} = 10^8 \mathrm{M}_\odot$, β_α peaks at $z \sim 22$ and is significantly nonzero from $z \sim 15 - 30$; fluctuations in the Lyman-α background are important over this range. For this scenario, the mean LW background reaches threshold ($J_{\mathrm{LW},21} \sim 0.1$) by $z \sim 21$.

2.4.3 Results

Results for the Lyman-α radiation background power spectra are displayed in Figure 2.9. For ease in comparison to our LW results, we use the corresponding scenarios from Fig 2.3, normalized to reach $J_{\rm LW,21} \sim 0.1$. Values for β_α in these scenarios are 0.89 for $M_{\rm min} = 10^6 {\rm M}_\odot$ at $z = 30.15$ (bottom panel) and 0.83 for $M_{\rm min} = 10^8 {\rm M}_\odot$ at $z = 20.5$ (top panel). The light cone versions are also shown (short-dashed curves; original versions are the solid curves). The two, long-dashed curves at the top of both panels represent fluctuations for these scenarios including the light cone effect and duty cycle. The topmost curve in both cases assumes an average lifetime of $\tau \sim 3$ Myrs ($f_{\rm duty} = 0.02$ for $M_{\rm min} = 10^6 {\rm M}_\odot$ and 0.01 for $M_{\rm min} = 10^8 {\rm M}_\odot$) while the second curve assumes $\tau \sim 10$ Myrs ($f_{\rm duty} = 0.06$ and 0.04 for $M_{\rm min} = 10^6 {\rm M}_\odot$ and $10^8 {\rm M}_\odot$ respectively).

As discussed in § 2.4.2, the mean Lyman-α intensity, J_α, is very nearly the critical intensity, J_α^c, around the time that the LW intensity reaches the threshold level for H_2 suppression (this can be seen in Figure 2.2). However, $J_\alpha \propto f_{\rm duty}$: stars are 'turned on' for a smaller fraction of the time and thus build the radiation background more slowly. Thus the duty cycle curves in this Figure are *not* at the coupling threshold. Obviously the fluctuations are boosted on small and mid-range scales (see Figure 2.9), but this is not surprising given that we are no longer probing the threshold epochs.

Present in the original models are a series of sequentially damped wiggles, in contrast to the smooth transition of the LW power. These result from the (Fourier transform of the) discontinuous horizon steps present in the Lyman-α flux profile. Unfortunately, these signature wiggles are smoothed out once the light cone effect is applied to the models. As discussed earlier in §2.4.1, the light cone effect bevels out the horizon steps that give the flux profile its distinctive shape, resulting in a more featureless profile and producing a nearly featureless power spectrum.

The power turns over at roughly $k_{\mathrm{Ly}\alpha} \sim 2\pi/r_{\mathrm{Ly}\alpha}$, where $r_{\mathrm{Ly}\alpha}$ is the Lyman-α horizon distance (discussed above in §2.4.1), except for the light cone versions whose turnovers shift to somewhat higher k. In addition, the amplitude of the light cone Lyman-α power is roughly a factor of 2 smaller than the corresponding amplitudes for the LW background for scales of $k \sim 0.1$ cMpc^{-1}. This is likely a symptom of the larger Lyman-α horizon distances, which are $\sim 3r_{\mathrm{LW}}$ for these redshifts. Furthermore, the light cone effect on the Lyman-α power is stronger than the corresponding effects on the LW fluctuations. The Lyman-α models corrected for halo growth over time are boosted in amplitude by a factor of ~ 7, while the LW models receive a boost by a factor of ~ 1.5. The large Lyman-α horizon allows points to 'see' more halos, bolstering the light cone effect on the most distant sources.

2.4.4 The 21-cm Signal

Finally, armed with the fluctuations in the radiation background and the fluctuations in the baryon density (computed with the linear power spectrum on these scales), we can estimate the 21-cm signal itself. Referring back to equation (2.26), we consider fluctuations in T_b sourced by perturbations in the matter density, Wouthuysen-Field coupling (or the Lyman-α flux), and radial velocity gradient of the gas. All of these fluctuations are isotropic except for the velocity fluctuation, which introduces an anisotropy to the power spectrum and can be written as $\delta_{\partial_v}(k) = -\mu^2\delta_b$ [Bharadwaj and Ali, 2004], where μ is the cosine of the angle between the wavenumber $\mathbf{k}$ of the Fourier mode and the line of sight. This enables the total power spectrum for T_b to be separated into powers of μ^2 [Barkana and Loeb, 2005b]:

$$P_{T_b}(\mathbf{k}) = \mu^4 P_{\mu^4}(\mathbf{k}) + \mu^2 P_{\mu^2}(\mathbf{k}) + P_{\mu^0}(\mathbf{k}). \tag{2.31}$$

The μ^2 term, which can be written as [Barkana and Loeb, 2005b]

$$P_{\mu^2}(k) = 2\mu^2[\beta P_\delta(k) + \beta_\alpha P_{\delta-\alpha}(k)], \tag{2.32}$$

contains contributions of density-induced fluctuations in the Lyman-α flux, where $P_{\delta-\alpha}(k)$ is the cross-power spectrum for the matter density and Lyman-α radiation background. In our halo model, this is very easy to calculate (c.f., [Cooray and Sheth, 2002]):

$$\begin{aligned}
P_{\delta-\alpha}(k) &= P^{1\mathrm{h}}_{\delta-\alpha}(k) + P^{2\mathrm{h}}_{\delta-\alpha}(k), \text{where} && (2.33)\\
P^{1\mathrm{h}}_{\delta-\alpha}(k) &= \int_{M_{\min}}^{\infty} dm n(m) \left(\frac{m}{\bar{\rho} f_{\mathrm{coll}}}\right)\left(\frac{m}{\bar{\rho}}\right) |u_\delta(k|m)||u_\alpha(k|m)| && (2.34)\\
P^{2\mathrm{h}}_{\delta-\alpha}(k) &= \left[\int_0^{\infty} dm n(m) \left(\frac{m}{\bar{\rho}}\right) u_\delta(k|m) b(m)\right] && (2.35)\\
&\quad \times \left[\int_{M_{\min}}^{\infty} dm n(m) \left(\frac{m}{\bar{\rho} f_{\mathrm{coll}}}\right) u_\alpha(k|m) b(m)\right] P^{\mathrm{lin}}(k), && (2.36)
\end{aligned}$$

where u_δ is the halo density profile that describes the distribution of mass within each halo.

Therefore, $P_{\mu^2}(k)$ can easily be used to investigate fluctuations in the Lyman-α background at high redshift. We display $P_{\mu^2}(k)$ in Figure 2.10 for $M_{\min} = 10^8 \mathrm{M}_\odot$ at redshifts $z = 11.05, 17.0, 20.5, 23.35$, and 25.8 (from top to bottom) so as to correspond to the scenarios presented in Figure 2.4. We find that fluctuations in T_b increase with decreasing redshift and decrease with scale. The increase in amplitude levels off once J_α reaches the critical intensity, J_α^c (which, for the scenario in Figure 2.10, occurs around $z \sim 18$). At this point the Lyman-α coupling is saturated ($x_{\mathrm{tot}} \gg 1$) and the 21 cm fluctuations become insensitive to the fluctuations in the Lyman-α background. One can also pick out the 'one-halo' term kicking in on small scales for these later epochs (the $z = 11.05$ curve in Figure 2.10).

The amplitude and overall shape of our power spectra are comparable to those presented in [Pritchard and Furlanetto, 2006], who used the same model to describe the Lyman-α flux but calculated P_{μ^2} using a linear transfer function. The

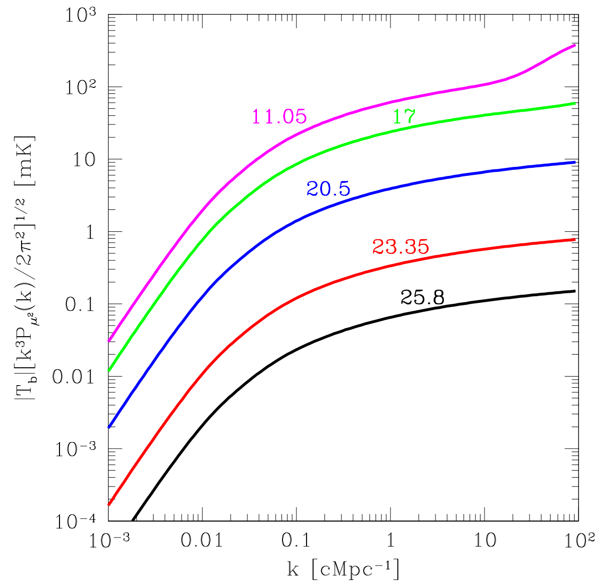

Figure 2.10: Power spectrum of T_b for the 21-cm transition, $|T_b|[k^3 P_{\mu^2}(k)/2\pi^2]^{1/2}$ (in mK), for scenarios with $M_{\rm min} = 10^8 {\rm M}_\odot$ for ease of comparison with Fig. 2.4. Scenarios include: $z = 11.05, 17.0, 20.5, 23.35$, and 25.8 from top to bottom.

amplitudes from our model also agree with those from [Barkana and Loeb, 2005a], although the shape of the power differs because they neglected the effects of atomic cascading (by assuming $f_{\rm recycle} = 1$) in their calculations.

Unfortunately, these power spectra do not display any sort of tell-tale signature feature such as the distinct LW turnover as can be seen in Figures 2.3 and 2.4 or the wiggles from the horizon steps, because the density-induced fluctuations wash them out. This agrees with previous work; recently, [Vonlanthen et al., 2011] showed with a radiative transfer numerical simulation that the horizon steps present in the Lyman-α flux profile left imprints in the differential brightness temperature profile just after the first luminous sources turned on. However, as time progressed and more new sources began contributing to the Lyman-α background, the steps were effectively wiped out.

2.5 Summary & Conclusions

In this paper, we have modeled fluctuations in the LW and Lyman-α radiation backgrounds using a variation of the halo model. First, we calculated the LW power spectrum and found that the power is characterized by an abrupt cut-off at the LW horizon distance, $r_{\rm LW}$; the power turns over at the horizon wavenumber, $k_{\rm LW}$, unless the sources are so rare that the one-halo term dominates (i.e., correlations are determined by the flux profiles of individual sources).

We found that the fluctuations in the background are weak and should not lead to substantial spatial fluctuations in H_2 content. Once a population of low-mass halos produces enough stars to generate a threshold LW background large enough to destroy their own H_2 reservoirs used for cooling, star formation can only proceed in larger halos with more substantial reservoirs. Our model predicts that, by the time this threshold is reached, fluctuations in the intensity field will be quite small, so this transition will be rather homogeneous across the entire Universe.

Though we found fluctuations in the background to be small around threshold, on the flip side we also found them to be large in those early epochs during which the background was approaching threshold. This could indicate the presence of patches of collapsing halos that are locally above threshold and H_2 suppressed. Taking into account the bias of sources, we crudely approximated the probability that a new halo lives in such a patch and found that even though source clustering substantially increases this probability, it is still relatively small. Thus, at this time, the majority of newly-forming halos can continue to cool via H_2, even in the presence of established galaxies [Dijkstra et al., 2008].

Eventually the first stars will build up the LW background by enough to suppress their own star formation; the process will terminate when only those halos above the atomic cooling threshold can form stars. However, the mode of star formation in these halos is very different from the minihalos that produce the first stars, so the transition to higher-mass halos has important consequences for the global star formation history [Oh and Haiman, 2002]. This transition from Population III to Population II star formation is of course extremely complex, and we have examined only a small part of it. The formation of very massive Population III stars requires two physical conditions: (1) metal-free gas and (2) a reservoir of H_2 that allows the gas to cool [Bromm and Larson, 2004]. We have not examined the first condition, but the slow speed of galactic winds (compared to the speed of light) guarantees that metal enrichment will be very inhomogeneous, and pristine pockets of gas could persist until very low redshifts [Scannapieco et al., 2002, Furlanetto and Loeb, 2005]. In contrast, the LW background is spatially uniform and so will induce a rapid, homogeneous transformation in the fundamental processes of star formation, even when metal enrichment remains inhomogeneous. This will induce a shift from very massive Population III.1 stars to less massive – but still primordial – Population III.2 stars that require atomic cooling.

Next we considered the fluctuations in the Lyman-α background in a similar fashion. The Lyman-α flux profile imprints a series of wiggles on the shape of the power, corresponding to the series of horizon steps that characterize the profile. Unfortunately, unlike the LW case, these signature wiggles are washed out once we account for halo growth over time. We found that the amplitude of the Lyman-α power is smaller than that for the LW background by a factor of ~ 2 for scales larger than ~ 15 cMpc. The smaller fluctuations are due to the large Lyman-α horizon distance, $r_{\mathrm{Ly}\alpha} \sim 3r_{\mathrm{LW}}$, allowing the halos to 'see' further.

We used our model for the fluctuations in the Lyman-α background to generate power spectra for the brightness temperature, T_b, of the 21-cm signal. We find our values to be in good agreement with previous estimates [Pritchard and Furlanetto, 2006, Barkana and Loeb, 2005a] that used a very different approach to estimate the radiation field fluctuations. We do not see a signature feature present in the power in contrast to the distinct LW turnover.

Our relatively simple model, though convenient and efficient, has a number of caveats that compromise accuracy. Most notably, we neglect nonlinear effects on the backgrounds by relying on a linear approximation for the halo-halo correlation function. Thus, our models are only good down to the scales for which this linear approximation still holds. In addition, we assumed a uniform star forming efficiency, $f_\star$, for all minihalos in our calculations. As the halo population grows in size and complexity in the later epochs, variations in galactic properties – sourced partly by the suppression of H_2 cooling, but also due to a myriad of other factors – will complicate our simple treatment. After comparing our results to the previous simulation from [Ahn et al., 2009] we find that the shapes can be well matched even with the limited dynamic range of the Ahn values (the signature turnover is not covered in their range). Although our amplitudes disagree by a factor of ~ 10 at the lower redshifts, we both find gentle fluctuations in the background around the time it reaches threshold, implying that 'safe' patches sheltering isolated sources of H_2 are rare by this epoch.

Furthermore, we have neglected the effects of X-rays in our models. If the first luminous sources had hard spectra that extended out to X-rays, these X-rays would have far reaching effects due to their large mean free paths – they could, by catalyzing the formation of new H_2, potentially counteract H_2 photodissociation by the growing UV background [McDowell, 1961, Haiman et al., 1996a, Haiman et al., 2000]. This could stall the transition of Population III to Population II stars by allowing minihalos to continue forming new stars, altering the make-up of the sources responsible for reionization.

Finally, [Tseliakhovich and Hirata, 2010] argue that a new nonlinear effect must be considered in structure formation: the supersonic relative velocity between dark matter and baryons can suppress the matter power spectrum near the baryonic Jeans scale, altering the abundance and clustering properties of the first dark matter halos. This effect could be accounted for in a future version of our simple model by introducing a modulation factor to the halo mass function. In fact, [Dalal et al., 2010] argue that the resulting fluctuations in the radiation background could strongly affect the 21-cm absorption power spectrum. However, they assume that the velocity exerts a very strong effect on galaxy formation, which may be at odds with more detailed numerical simulations [Maio et al., 2011, Stacy et al., 2011]. In any case, such a large scale modulation will add more power to the radiation field and may have important implications for the homogeneity of the LW and Lyman-α backgrounds, since these acoustic features appear on comparable scales to the LW horizon (~ 100 Mpc).

CHAPTER 3

Fluctuations in the High Redshift Near-Infrared Background

3.1 Introduction

The detailed nature of the reionization of intergalactic neutral hydrogen is as yet uncertain, but the larger picture is generally well illustrated. The nine-year *Wilkinson Microwave Anisotropy Probe* (WMAP-9) results indicate that reionization occurred at a redshift of $z_{reion} \sim 10$ if the process was instantaneous and homogeneous in a spatially flat universe [Hinshaw et al., 2012]. Detections of the Gunn-Peterson (GP) trough [Gunn and Peterson, 1965] in $z \sim 6$ quasars [Becker et al., 2001, Fan et al., 2002, Fan et al., 2006] suggest that the reionization process was in its final stages around that time. We are certain that reionization took place but the exact make up of the responsible ionizing source population is still unclear. Stars likely did most of the work since they are efficient sources of ionizing photons- but what were these very early stars actually like?

Even though we are determinedly traveling ever deeper into our cosmic history by studying the Hubble Ultra Deep Field (HUDF; [Oesch et al., 2012, Bouwens et al., 2013, Ellis et al., 2013, Robertson et al., 2013]) and embarking on new campaigns such as the Cluster Lensing and Supernova survey with Hubble (CLASH; [Postman et al., 2012]), we are still unable to directly detect the first stars (Population III). The bits and pieces that we do know about Pop III stars lie mostly within theory; they formed out of metal-free H/He gas contained in minihalos at redshifts $z \sim 20-30$ [Couchman and Rees, 1986a]. Up until recently, it was widely accepted that Pop III stars formed in isolation and were probably very massive, with typical masses $M_\star \sim 100 M_\odot$ [Yoshida et al., 2006]. However more recent simulations [Clark et al., 2008, Stacy et al., 2010b, Clark et al., 2011a, Clark et al., 2011b] suggest that fragmentation in the primordial protostellar disks is possible, producing additional protostars with masses ~ 0.1 to $10 M_\odot$ [Greif et al., 2011] and allowing for rich Pop III stellar clusters.

If Pop III stars in fact contributed to the reionization of the universe [Barkana and Loeb, 2001a]; the degree to which they contribute is in part limited by how soon prior to reionization they disappear, which is determined by how soon the H_2 suppressing background sterilizes the minihalos [Holzbauer and Furlanetto, 2012] and the rate of early chemical enrichment of the IGM. Some studies suggest that Pop III SF at low levels could extend to as far as $z \sim 2.5$, in small halos living in extremely rare patches that have avoided metal enrichment even at these late times [Furlanetto and Loeb, 2005, Jimenez and Haiman, 2006, Tornatore et al., 2007]. Some recent models of reionization are friendly to Pop III stars; [Trenti and Stiavelli, 2009] find that if multiple Pop III stars are allowed to form in a single halo, then they can easily account for the remaining optical depth, τ_e, needed to explain the WMAP-5 data for $z > 7$.

Because current and near future instruments are unfortunately incapable of resolving individual Pop III stars, we have to rely on indirect methods. If Pop III stars are primarily found in the redshift range $10 \leq z \leq 30$, then they would be expected to contribute to the cosmic infrared background (CIRB; $1 - 300 \mu m$) in the NIR at $1 - 5 \mu m$ [Bond et al., 1986], as the ionizing continuum of such a hot, early star will be redshifted into this window. While dust emission taints the mid- and far-IR background, starlight dominates the CIRB in the NIR range [Dwek et al., 1998]. Additionally, the Lyman-α recombination lines emitted at $z = 7 - 15$ are redshifted to $\sim 1 - 2\mu m$, making the NIR background amenable for hunting Pop III stellar signatures.

There have been several measurements of the NIR background and subsequent theoretical studies attempting to explain them in recent years [Kashlinsky, 2005]. Using the data from the Diffuse Infrared Background Experiment (DIRBE) instrument on board the *Cosmic Background Explorer* (COBE) satellite, multiple authors [Wright, 2001, Cambrésy et al., 2001, Levenson et al., 2007] detected residual, isotropic background intensities in the J (1.25μm), K (2.2μm), and L (3.5μm) bands after subtracting the zodiacal (due to thermal emission from interplanetary dust grains) and galactic stellar foregrounds. [Matsumoto et al., 2005] used the Near-Infrared Spectrometer (NIRS) on the *Infrared Telescope in Space* (IRTS) and found similar results. Integrated source counts in the J and K bands from deep surveys like the Hubble Deep Field [Madau and Pozzetti, 2000] and Subaru Deep Field [Totani et al., 2001] cannot account for the total observed NIR background.

Theoretical studies, motivated by this issue, suggest that Pop III stars could be responsible for a substantial fraction of the observed excess emission [Santos et al., 2002, Salvaterra and Ferrara, 2003, Cooray and Yoshida, 2004] [Fernandez and Komatsu, 2006]. Even with additional constraints on the first luminous sources such as the observed metallicity of the IGM [Madau and Silk, 2005] and the soft X-ray background [Dijkstra et al., 2004], interpreting NIR data is tricky. Measuring the NIR background is extremely difficult due to the removal of foreground stars and galaxies and zodiacal light, whose emission is ~ 3 times as large as the isotropic component [Fernandez and Komatsu, 2006]. [Thompson et al., 2007a] observed the NIR background using the Near-Infrared Camera and Multi-Object Spectrometer (NICMOS; $1.1 - 1.6\mu$m) on the *Hubble Space Telescope* (HST). Their data revealed fluxes that were significantly below those previously reported using NIRS, leading them to the conclusion that their data can be entirely explained by normal resolved galaxies between $z \sim 0-7$.

Though the accuracy of measurements of the mean NIR background is still in question, measuring *fluctuations* in the background could be more forgiving because they are less sensitive to zodiacal light subtraction (zodiacal light is very smooth), which really only effects the amplitude of the monopole, or the mean background. Further, some theoretical models predict that unresolved galaxies at $z \geq 3$ are expected to dominate the anisotropy of the CIRB at $\lambda \geq 4\mu$m for all angular scales of interest, while Pop III stars are expected to dominate for $1 \leq \lambda \leq 4\mu$m over tens of arcminute scales [Cooray et al., 2004], since these extremely distant sources should be strongly clustered with low shot noise. This makes the NIR an interesting regime to study Pop III clustering, which is an important ingredient in our understanding of early structure formation.

Observations of NIR anisotropies are, however, not without their own share of controversy. Some early studies have claimed that observed excess fluctuations (above those expected from normal galaxies) are indeed due to Pop III stars [Kashlinsky, 2005, Kashlinsky et al., 2007], while others insist that they simply originate from the clustering of low redshift galaxies [Cooray et al., 2007, Thompson et al., 2007b]. Since then, the controversy over where exactly this excess is coming from has continued to simmer. Most recently, [Matsumoto et al., 2011] detected significant fluctuations on scales of a few hundred arcseconds using AKARI ($2.4-4.1\mu$m). They claim that the excess anistropy can very well be due to Pop III stars at high redshift. [Kashlinsky et al., 2012] again confirmed excess fluctuations in the Spitzer Extended Deep Survey (SEDS) with IRAC; they believe that the excess must originate from a high-z population consistent with the first stars or an as yet undiscovered source population. In opposition, [Cooray et al., 2012a] detected an excess with data from the Spitzer Deep Wide-Field Survey (SDWFS) that is so large that it cannot be explained by Pop III stars with reasonable star formation rates; they suggest that it can however be simply explained by diffuse intrahalo light emanating from low redshift dark matter halos.

Recent theoretical endeavors [Magliocchetti et al., 2003, Cooray et al., 2004, Salvaterra et al., 2006, Fernandez et al., 2010, Cooray et al., 2012b] [Fernandez et al., 2012] to explain these putative excess anisotropies are also unclear. [Cooray et al., 2004] employ a halo model-like approach to model fluctuations of the NIR background due to Pop III stars. They predicted that Pop III stars produce a signature peak at tens of arcminute scales in the angular power spectrum, C_l, of NIR background anisotropies and expressed optimism that Pop III clustering could be observable depending on the extent to which future studies can remove foreground sources and zodiacal light. However, [Fernandez et al., 2010] do not see such a signature when utilizing a large-scale N-body simulation. Additionally, the most recent endeavors are still unable to reproduce the amplitude of the observed excess fluctuations with Pop III stars alone.

At this point there is a gathering consensus that the detected excess anisotropies do indeed exist– a small fraction could originate from faint galaxies at low redshift [Helgason et al., 2012], but there also could be an extractable signal originating from galaxies of the reionization era. In this paper, we will use a semi-analytic argument in combination with the most recent high redshift observations to determine the feasibility of such an extraction and predict how much of the NIRB excess Pop III stars could have produced. In section 3.2 we will describe the analytic formulae with which we model the total Pop III emission emanating from each DM halo and also how we constrain this model with recent observations. In section 3.3 we calculate the mean NIRB excess produced by Pop III stars and compare our predictions to observations, while in section 3.4 we do the same for the angular PS. We present a summary and conclusions in section 4.6.

We adopt a background cosmology $(\Omega_0, \Omega_\Lambda, \Omega_b, h) = (0.286, 0.7185, 0.0464, 0.697)$

consistent with the most recent WMAP-9 results [Hinshaw et al., 2012].

3.2 The NIR Background

Our simple prescription for the NIRB is based primarily on the halo model, as described by [Cooray and Sheth, 2002]. The halo model uses properties of virialized dark matter halos to calculate the effects of non-linear gravitational clustering, assuming that all mass in the universe is compartmentalized in such halos, whose properties can be parameterized purely by their mass, M_h.

Each halo glows with its very own contribution to the total background, which is made up of both direct stellar emission and indirect nebular (the gas in the host halo not incorporated into stars) emission. The nebular emission comes from free-free emission and reprocessed ionizing photons which are spit out from the stars. Only the fraction of ionizing photons, $(1 - f_{esc})$, that do not escape from the halo and into the intergalactic medium (IGM) contribute. If we can calculate each halo's individual contribution to the total background and how the halos are spatially distributed, then we can describe what the total background looks like. The latter is given by the halo model (see §3.4.1), while the former can be described as follows.

If we install a single galaxy at the center of each halo, and can characterize the stellar population being harbored by each galaxy, then we can determine the emission emanating from one halo. We can make assumptions as to the initial mass function (IMF) of the primordial stellar population, which is still rather uncertain, and utilize the stellar synthesis models of Pop II and Pop III stars from [Schaerer, 2002] to acquire the total galactic emission. We can then combine this with the halo model to calculate the observed mean NIRB intensity and the volume emissivity produced by these stars. These results can be directly compared to observations of the UV luminosity density [Ellis et al., 2013,

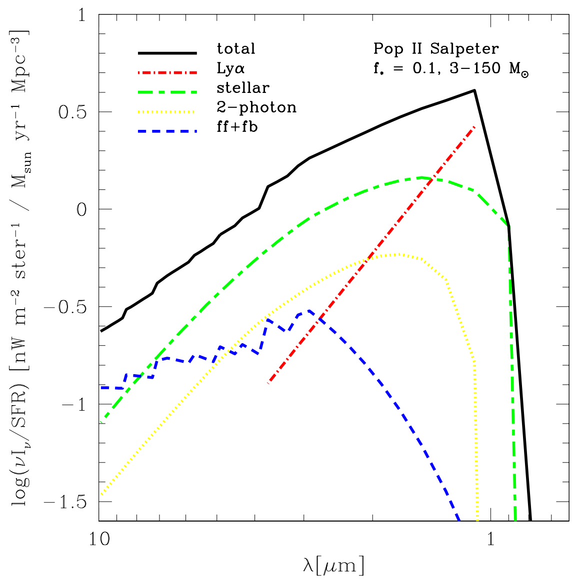

Figure 3.1: The intensity per star formation rate (SFR) produced by Pop II stars living at redshifts $z = 7 - 30$ in units of $\left[nW\ m^{-2}\ ster^{-1}/M_{\odot}\ yr^{-1}\ Mpc^{-3}\right]$ at varying wavelengths produced by the Lyman-α recombinations (dot-dashed/red), direct stellar emission (long and short dashed/green), 2-photon recombinations (dotted/yellow), and free-free and free-bound emission (short dashed/blue). The total intensity per SFR is shown as the black solid curve. The stellar population is characterized by a Salpeter IMF ranging in mass from $3 - 150 M_{\odot}$ and SF efficiency of $f_{\star} = 0.1$.

Robertson et al., 2013] and mean NIRB (see Table 3.1) to calibrate the star formation efficiency and assess the primordial stellar contribution to the NIRB excess, respectively.

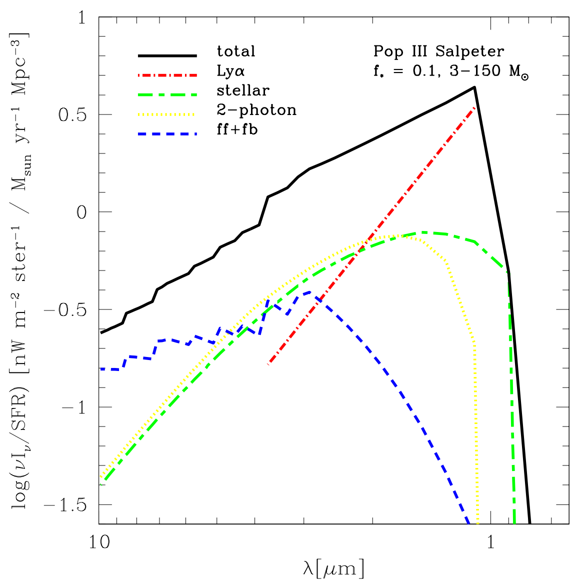

Figure 3.2: The intensity per star formation rate (SFR) produced by Pop III stars living at redshifts $z = 7 - 30$ in units of $\left[nW\ m^{-2}\ ster^{-1}/M_{\odot}\ yr^{-1}\ Mpc^{-3}\right]$ at varying wavelengths produced by the Lyman-α recombinations (dot-dashed/red), direct stellar emission (long and short dashed/green), 2-photon recombinations (dotted/yellow), and free-free and free-bound emission (short dashed/blue). The total intensity per SFR is shown as the black solid curve. The stellar population is characterized by a Salpeter IMF ranging in mass from $3-150 M_{\odot}$ and SF efficiency of $f_{\star} = 0.1$.

3.2.1 The Volume Emissivity and Halo Luminosity

We can write the observed mean intensity at an observed frequency, ν, and redshift, z, (following pg. 115 from [Loeb and Furlanetto, 2013]) as:

$$\bar{J}_\nu(z) = \frac{c}{4\pi}\int_z^\infty dz' \frac{\bar{\epsilon}_{\nu'}(z')}{H(z')(1+z')}, \tag{3.1}$$

where $H(z)$ is the cosmic expansion rate and $\bar{\epsilon}_{\nu'}(z')$ is the comoving volume emissivity at emitting frequency, $\nu' = \nu(1+z')/(1+z)$, and redshift, z'. We assume that the time averaged star formation rate (SFR) density is proportional to the time derivative of the collapse fraction, f_{coll} (fraction of mass in the universe contained in galaxies, or collapsed in a halo). In this work, we use the Sheth-Tormen mass function [Sheth and Tormen, 1999] to calculate f_{coll}. With this, we can write the star formation rate density as $\dot{\rho}_\star(z) = f_\star \times \dot{M}_{\rm acc}$, or:

$$\dot{\rho}_\star(z) = \bar{\rho}_{b0} f_\star \left[\frac{d}{dt} f_{coll}(z)\right], \tag{3.2}$$

where $f_\star$ is the star formation efficiency (fraction of baryons that actually go into forming stars over the typical star forming (SF) timescale, which we will assume here to be the same for all halos), and the mean baryon density today is $\bar{\rho}_{b0} = 2.775 \times 10^{11}(\Omega_b h^2) M_\odot Mpc^{-3}$. We define the SF timescale as $t_{SF} \equiv [d\ ln\ \rho_\star(z)/dt]^{-1}$. From eqn 4.2, it follows that $t_{SF} \equiv [d\ ln\ f_{coll}(z)/dt]^{-1}$, which is around 55 Myrs at $z = 10$. $\dot{M}_{\rm acc}$ is the rate at which the halo accretes baryonic gas.

In order to determine the total volume emissivity, $\bar{\epsilon}_\nu$, it is necessary to adopt a model describing the stellar population residing in each halo (described in detail in §3.2.2). When considering the total emission produced by a single star of mass, m, one simply needs to add up all of the emission that is produced over the entire lifetime of that star, $\tau(m)$, to calculate the total. However, when considering a population of stars, over the course of the SF timescale new stellar members are being formed while members who formed earlier are simultaneously growing older.

In this case, some stellar members have newly formed after older members have gone dark. In this case, we cannot just add up the emission from the entire family because not all members are turned on at the same time. If we want to take a snapshot of the total emission at a particular time, we need to correct for this (see appendix A from [Fernandez and Komatsu, 2006]). The volume emissivity is now written as:

$$\bar{\epsilon}_\nu(\nu, z) = \frac{\dot{\rho}_\star(z)}{m_\star} \int dm f(m) \bar{L}_\nu(m) \tau(m), \tag{3.3}$$

where $\rho_\star(z) = \bar{\rho}_{b0} f_\star f_{coll}(z)$ is the stellar mass density, $f(m)$ is the initial mass function (IMF) for the stellar population, $m_\star$ is the average stellar mass of the population, and $\bar{L}_\nu(m)$ is the stellar luminosity at frequency, ν, of a star with mass, m, averaged over its main sequence lifetime, $\tau(m)$.

Now that we have the volume emissivity, our next step is to compute the luminosity per stellar mass, $l_\nu(z)$, which is simply the volume emissivity divided by the stellar mass density:

$$l_\nu(z) = \frac{1}{m_\star t_{SF}(z)} \int dm f(m) \bar{L}_\nu(m) \tau(m). \tag{3.4}$$

Next, we compute the frequency band-averaged luminosity per stellar mass, $\bar{l}(z)$, by integrating $l_\nu(z)$ over the observed frequency band $(\nu_1 - \nu_2)$ we are looking at:

$$\bar{l}(z) = \int_{\nu_1(1+z)}^{\nu_2(1+z)} d\nu \ l_\nu(z). \tag{3.5}$$

Finally, we can obtain an expression for the luminosity per halo mass. The total stellar mass contained in a halo of mass, M_h, is $M_\star(M_h) = f_\star M_h(\Omega_b/\Omega_m)$. With that,

$$\frac{L_h(z)}{M_h} = f_\star \frac{\Omega_b}{\Omega_m} \bar{l}(z). \tag{3.6}$$

The NIRB is composed of several separate components: the direct stellar emission component ($\bar{l}^\star(z)$, discussed in §3.2.3.2) and the indirect nebular emission components ($(1 - f_{esc})\bar{l}^{neb}(z)$). The reprocessed light is made up of Lyman-α line emission ($\bar{l}^{Ly\alpha}(z)$, discussed in §3.2.3.3), two-photon continuum emission ($\bar{l}^{2\gamma}(z)$, discussed in §3.2.3.4), and free-free and free-bound continuum emission ($\bar{l}^{free}(z)$, discussed in §3.2.3.5):

$$\frac{L_h(z)}{M_h} = f_\star \frac{\Omega_b}{\Omega_m} \{\bar{l}^\star(z) + (1 - f_{esc})[\bar{l}^{ff+fb}(z) + \bar{l}^{2\gamma}(z) + \bar{l}^{Lya}(z)]\}. \tag{3.7}$$

3.2.2 Stellar Properties and Populations

Past literature exploring models of the NIRB have used various analytic prescriptions to describe the earliest stellar populations and their properties. However, very little is known as to the exact properties of Pop III stellar families. Following [Fernandez and Komatsu, 2006], we adopt two different IMFs, $f(m)$, to represent the total stellar mass spectrum. The first is a Salpeter [Salpeter, 1955] IMF with a mass range of $3 - 150 M_\odot$:

$$f(m) \propto m^{-2.35}, \tag{3.8}$$

while the second is a Larson [Larson, 1998] IMF with mass range of $5 - 150 M_\odot$:

$$f(m) \propto \frac{1}{m}\left(1 + \frac{m}{m_c}\right)^{-1.35}, \tag{3.9}$$

where $m_c = 50 M_\odot$. The average stellar mass of the population is calculated as follows:

$$m_\star = \int dm\, m f(m), \tag{3.10}$$

where $m_\star = 8.7$ and $27.4 M_\odot$ for the Salpeter and Larson IMFs respectively. As we are only interested in stars that produce a non-negligible supply of ionizing photons, the values we use here for the SF efficiency, $f_\star$, only account for this high stellar mass component. The actual values of $f_\star$, which also incorporate non-contributing low-mass stars, are most likely larger. Recent simulations [Clark et al., 2008, Stacy et al., 2010b, Clark et al., 2011a, Clark et al., 2011b] challenge the long accepted scenario of isolated, massive Pop III SF and suggest a model rife with significant fragmentation in the primordial protostellar disks. These fragments could lead to additional protostars with masses ~ 0.1 to $10 M_\odot$ [Greif et al., 2011]. In this case, a Salpeter IMF could be more appropriate and a Larson IMF would result in an upper limit for the total stellar emission. In this work, we will employ by default a conservative Salpeter IMF for Pop II and Pop III populations and a top-heavy Larson IMF for more optimistic Pop III scenarios.

Next we consider properties of individual stars: the main sequence lifetime $\tau(m)$, the hydrogen photoionization rate $\bar{Q}_H(m)$ (averaged over the lifetime), intrinsic bolometric luminosity $L^\star_{bol}(m)$ and effective temperature $T^\star_{eff}(m)$ (both calculated for zero-age main sequence stars), and the stellar radius $R_\star(m)$. We present these properties for Pop III metal-free ($Z = 0$) stars and Pop II metal-poor ($Z = 1/50 Z_\odot$) stars below in §4.2.2.1 and §4.2.2.2.

3.2.2.1 Metal-Free Stellar Properties

We use the following fitting formulae from [Schaerer, 2002] to model properties of individual metal-free ($Z = 0$) Pop III stars. The main sequence lifetime, $\tau(m)$, and hydrogen photoionization rate, $\bar{Q}_H(m)$ (number of ionizing photons produced per second, averaged over the lifetime), apply to stars with $m = 5 - 500 M_\odot$:

$$\log_{10}\left(\frac{\tau}{yr}\right) = 9.785 - 3.759x + 1.413x^2 - 0.186x^3, \tag{3.11}$$

$$\log_{10}\left(\frac{\bar{Q}_H}{sec^{-1}}\right) = \begin{cases} 39.29 + 8.55x, & 5 - 9M_\odot \\ 43.61 + 4.9x - 0.83x^2, & 9 - 500M_\odot \end{cases} \tag{3.12}$$

where $x \equiv \log_{10}(m/M_\odot)$. The bolometric luminosity, $L^\star_{bol}(m)$, and effective temperature, $T^\star_{eff}(m)$, apply to stars with $m = 5 - 1000 M_\odot$:

$$\log_{10}\left(\frac{L^\star_{bol}}{L_\odot}\right) = 0.4568 + 3.897x - 0.5297x^2, \tag{3.13}$$

$$\log_{10}\left(\frac{T^\star_{eff}}{K}\right) = 3.639 + 1.501x - 0.5561x^2 + 0.07005x^3. \tag{3.14}$$

For those formulae that do not reach down to our lower stellar mass limits, we will simply extrapolate as necessary. This should not affect our results, as the lowest mass stars produce a negligible amount of ionizing photons (less than 1% of the total for both Pop III and Pop II stars).

We define the stellar radius, $R_\star(m)$, as

$$4\pi R_\star^2(m) = \frac{L_{bol}^\star(m)}{\sigma T_{eff}^4(m)}, \tag{3.15}$$

where $\sigma = 5.67 \times 10^{-5}\ erg\ sec^{-1}\ cm^{-2}\ K^{-4}$ is the Stefan-Boltzmann constant.

3.2.2.2 Metal-Poor Stellar Properties

We use the following fitting formulae from [Schaerer, 2002] for individual metal-poor ($Z = 1/50 Z_\odot$) Pop II stars. The lifetime and photoionization rate apply for stars with $m = 7 - 150 M_\odot$:

$$\log_{10}\left(\frac{\tau}{yr}\right) = 9.59 - 2.79x + 0.63x^2, \tag{3.16}$$

$$\log_{10}\left(\frac{\bar{Q}_H}{sec^{-1}}\right) = 27.8 + 30.68x - 14.8x^2 + 2.5x^3. \tag{3.17}$$

To account for stars with masses less than $7M_\odot$, we will simply extrapolate as necessary. This should not affect our results, as the lowest mass stars produce a negligible amount of ionizing photons (less than 1% of the total).

We use the fitting formulae from [Lejeune and Schaerer, 2001] for the bolometric luminosity and effective temperature:

$$\log_{10}\left(\frac{L_{bol}^\star}{L_\odot}\right) = 0.138 + 4.28x - 0.653x^2, \tag{3.18}$$

$$\log_{10}\left(\frac{T_{eff}^\star}{K}\right) = 3.92 + 0.704x - 0.138x^2. \tag{3.19}$$

3.2.3 Components of the NIRB

As discussed above, the light that makes up our observed NIRB comes from both direct and indirect processes. The most obvious component is the direct production supply, which is simply made up of stellar emission. We assume that all stellar ionizing photons (with energies $E_\gamma \geq 13.6$ eV) are absorbed. The fraction, $(1 - f_{esc})$, of these photons that do not escape from the halo and into the IGM contribute to indirect nebular emission, making up our indirect production supply. Some of those photons are subsequently absorbed and ionize the surrounding hydrogen, which gives way to to free-bound continuum emission, Lyman-α line emission, and 2-photon continuum emission. Brehmsstralung, or free-free continuum emission, also takes place within the ionized gas and accounts for $\sim 1/4$ of the cooling in the nebula [Santos et al., 2002].

About half of all energy radiated by a Pop III star is ultimately reradiated via recombination [Santos et al., 2002]. Around 2/3 of that recombination energy is released in Lyman-α or 2-photon emission, while the remainder is emitted in other recombination lines and free-bound continuum emission.

3.2.3.1 The Stellar Ionizing Efficiency

We can determine the total emission from each component by first calculating the stellar ionizing efficiency, $\bar{\epsilon}_b$, i.e., the average number of hydrogen ionizing photons emitted per stellar baryon. Most of the NIR emission components are directly proportional to the ionizing emissivity, which we will parameterize through $\bar{\epsilon}_b$. We obtain $\bar{\epsilon}_b$ by integrating the hydrogen photoionization rate and stellar lifetime over the stellar IMF:

$$\bar{\epsilon}_b = \frac{\int dm \; f(m) Q(m) \tau(m)}{\int dm \; f(m)(m/m_p)}, \tag{3.20}$$

where m_p is the proton mass. Eqn 3.20 gives us the stellar ionizing efficiency averaged over the entire stellar population. Average ionizing efficiencies for Pop III stars with a Salpeter and Larson IMF are approximately $\bar{\epsilon}_b \sim 30,000$ and $60,000$ photons per baryon, respectively. The average ionizing efficiency for Pop

II stars with a Salpeter IMF is $\sim 23,000$ photons per baryon.

3.2.3.2 The Direct Stellar Component

Stellar continuum photons directly emitted by stars make a large contribution to the NIRB. Stellar spectra originating from very massive, metal-free Pop III stars and metal-poor Pop II stars can be reasonably modeled using a blackbody of effective temperature, T_{eff}, for energies below 13.6 eV [Bromm et al., 2001]:

$$B_\nu(T_{eff}) = \frac{2h\nu^3/c^2}{\exp\left(h\nu/kT_{eff}\right) - 1}. \tag{3.21}$$

Ionizing photons must be treated in a more detailed manner [Schaerer, 2002], however we will simply assume that all of these photons are totally absorbed. We write the luminosity from direct stellar emission produced by a star of mass m, $L^\star_\nu(m)$, as:

$$\bar{L}^\star_\nu(m) = \begin{cases} 4\pi R^2_\star(m) B_\nu(T_{eff}), & h\nu < 13.6\ eV \\ 0, & h\nu \geq 13.6\ eV \end{cases} \tag{3.22}$$

where $R_\star(m)$ is the stellar radius (see eqn 3.15).

Finally, we can write the stellar luminosity per halo mass as:

$$\left.\frac{L_h(z)}{M_h}\right|_\star = f_\star \frac{\Omega_b}{\Omega_m} \frac{1}{t_{SF}(z)\cdot m_\star} \bar{\xi}^\star, \tag{3.23}$$

where

$$\bar{\xi}^\star = \int dm f(m) \bar{L}^\star_\nu(m) \tau(m). \tag{3.24}$$

3.2.3.3 The Lyman-α Component

If a recombination in the nebula results in a higher order Lyman series photon, it will simply be reabsorbed and eventually cascade to the $n = 2 \to 1$ transition. Around $f_{Ly\alpha} \sim 2/3$ of the time [Cantalupo et al., 2008], this transition will produce a Lyman-α photon via $2p \to 1s$. These Lyman-α photons are then resonantly scattered in neutral hydrogen and do not freely escape into the IGM until they redshift out of the resonance. The other $\sim 1/3$ of the time, the photon will undergo the forbidden 2-photon decay ($2s \rightarrow 1s$) and emit continuum emission (see §3.2.3.4).

If we consider only the Lyman-α component contribution to the total emissivity, and assume that none of these photons are destroyed by dust, we have:

$$\bar{\epsilon}_{\nu}^{Ly\alpha}(\nu, z) = \frac{\dot{\rho}_{\star}(z)}{m_p}(1 - f_{esc}) f_{Ly\alpha} \bar{\epsilon}_b E_{Ly\alpha} \phi(\nu - \nu_{Ly\alpha}), \tag{3.25}$$

where $\dot{\rho}_{\star}(z)$ is the mean SFR (given by eqn 3.2), m_p is the proton mass, $f_{Ly\alpha}$ is the fraction of ionized photons that turn into Lyman-α photons ($\sim 2/3$), $\bar{\epsilon}_b$ is the average number of ionizing photons emitted per baryon (given by eqn 3.20), $E_{Ly\alpha}$ is the energy of a Lyman-α photon, and $\phi(\nu - \nu_{Ly\alpha})$ is the line profile.

We can approximate the line profile in this case as a delta function, as in [Fernandez and Komatsu, 2006]. This is a reasonable approximation because we assume relatively broadband observations that do not resolve the line's structure. The line profile is given by:

$$\phi(\nu - \nu_{Ly\alpha}) = \delta(\nu - \nu_{Ly\alpha}), \tag{3.26}$$

where $\nu_{Ly\alpha}$ is the Lyman-α rest frequency. Moreover,

$$\delta(\nu - \nu_{Ly\alpha}) = \frac{\delta\left(z - z_{Ly\alpha}\right)}{\nu_{obs}}, \tag{3.27}$$

where $\nu_{obs} = \nu_{Ly\alpha}/(1 + z_{Ly\alpha})$ is the observed frequency. Since we are integrating the total emission over a broad frequency band for many luminous objects living at different redshifts, this approximation will not affect our results.

The Lyman-α luminosity per halo mass can be written as:

$$\left.\frac{L_h(z)}{M_h}\right|_{Ly\alpha} = f_{\star} \frac{\Omega_b}{\Omega_m}(1 - f_{esc}) \frac{f_{Ly\alpha} \bar{\epsilon}_b E_{Ly\alpha}}{t_{SF}(z) m_p}. \tag{3.28}$$

In reality, some of these photons will be absorbed by the IGM as they travel towards us, so we are being optimistic as to the brightness of these galaxies in Lyman-α.

3.2.3.4 The Two-Photon Component

All stellar ionizing photons result in a $n = 2 \rightarrow 1$ transition. Most of these photons (a fraction, $f_{Ly\alpha} \sim 0.64$) result in the emission of a Lyman-α photon by way of a $2p \rightarrow 1s$ transition. The remaining fraction, $(1 - f_{Ly\alpha})$, however, eventually undergo two-photon decay via $2s \rightarrow 1s$ and result in continuum emission. Following [Fernandez and Komatsu, 2006] (who performed a fit to data from [Brown and Mathews, 1970]), we write the probability, $P(y)$, per two-photon decay of producing a photon with frequency in the range $dy = d\nu/\nu_{Ly\alpha}$ as:

$$P(y) = 1.307 - 2.627(y - 0.5)^2 + 2.563(y - 0.5)^4 - 51.69(y - 0.5)^6, \tag{3.29}$$

where $P(y)$ is normalized such that $\int_0^1 P(y)dy = 1$. With that, we can describe this emission with a luminosity, $\bar{L}_\nu^{2\gamma}(m)$, coming from one star of mass, m, as:

$$\bar{L}_\nu^{2\gamma}(m) = \frac{2h\nu}{\nu_{Ly\alpha}}(1 - f_{Ly\alpha})P(\nu/\nu_{Ly\alpha})\bar{Q}_H(m). \tag{3.30}$$

Integrating over the observed frequency band $(\nu_1 - \nu_2)$ and stellar IMF, the two-photon luminosity per halo mass becomes:

$$\begin{aligned} \left.\frac{L_h(z)}{M_h}\right|_{2\gamma} &= f_\star \frac{\Omega_b}{\Omega_m}(1 - f_{esc})\frac{2h}{\nu_{Ly\alpha}}\frac{(1 - f_{Ly\alpha})\bar{\epsilon}_b}{t_{SF}(z)m_p} \cdot \nu_{Ly\alpha}^2 \int dx\; xP(x) \\ &\approx \left.\frac{L_h(z)}{M_h}\right|_{Ly\alpha} \cdot \int dx\; xP(x). \end{aligned} \tag{3.31}$$

For $z = 10$, the factor $\int dx\; xP(x)$ has values of 0.2 and 0.5 for an observed bandpass of $1 - 2\mu$m and $1 - 5\mu$m respectively.

3.2.3.5 The Free-Free and Free-Bound Components

Free-free and free-bound continuum emission also makes a contribution, however small, to the total NIRB. We follow [Fernandez and Komatsu, 2006] in the treatment of these components and write the continuum luminosity as:

$$\bar{L}_\nu^{cont}(m) = \frac{\epsilon_\nu \bar{Q}_H(m)}{n_e n_p \alpha_B}, \tag{3.32}$$

where n_e and n_p are the number densities of electrons and protons, respectively, and α_B is the case B recombination coefficient for hydrogen [Spitzer, 1978]:

$$\alpha_B = \frac{2.06 \times 10^{-11}}{T_g^{1/2}} \phi_2(T_g) \text{ cm}^3 \text{ sec}^{-1}. \tag{3.33}$$

$\phi_2(T_g)$ is a dimensionless function of the gas temperature, T_g, which in turn depends on the stellar spectrum. [Fernandez and Komatsu, 2006] assume a gas temperature of $T_g \sim 20,000$ K, for which $\phi_2 \simeq 1$.

The volume emissivity, ϵ_ν, including both the free-free and free-bound emission is given by equation 6.22 of [Dopita and Sutherland, 2002]:

$$\epsilon_\nu = 4\pi n_e n_p \gamma_c(\nu) \frac{e^{-hv/kT_g}}{T_g^{1/2}} \text{ erg cm}^{-3} \text{ sec}^{-1} \text{ Hz}^{-1}, \tag{3.34}$$

where the continuum coefficient, γ_c, is given by:

$$\gamma_c(\nu) \equiv f_k \left[\bar{g}_{ff} + \sum_{n=2}^{\infty} \frac{x_n e^{x_n}}{n} g_{fb}(n) \right], \tag{3.35}$$

assuming complete ionization and ignoring the helium contribution, and where $x_n \equiv Ry/(kT_g n^2)$ ($Ry = 13.6$ eV is the Rydberg energy for the hydrogen atom), while $f_k = 5.44 \times 10^{-39}$ cm^3 erg/sec/Hz. The continuum coefficient is a function of frequency since each recombination is a transfer of finite energy, and cannot result in a photon with more energy than the initial budget. The summation in equation 3.35 is effectively taken from $n \geq 2$ as photons resulting from free-bound transitions to $n = 1$ are ravenously absorbed by nearby hydrogen atoms. The Gaunt factors for both free-free ($\bar{g}_{ff} \simeq 1.1$) and free-bound ($\bar{g}_{fb} \simeq 1.05$) emission are approximately constant [Karzas and Latter, 1961] for $T_g \sim 20,000$ K.

Finally, we can write the total free-free and free-bound luminosity per halo mass as:

$$\begin{aligned}\left.\frac{L_h(z)}{M_h}\right|_{free} &= \frac{4\pi}{2.06\times10^{-11}} f_\star \frac{\Omega_b}{\Omega_m}(1-f_{esc})\frac{\bar{\epsilon}_b}{t_{SF}(z)m_p} \\ &\times \int d\nu\ e^{-h\nu/kT_g}\gamma_c(\nu) \\ &= \frac{4\pi}{2.06\times10^{-11}}\frac{1}{E_{Ly\alpha}f_{Ly\alpha}}\left.\frac{L_h(z)}{M_h}\right|_{Ly\alpha} \\ &\times \int d\nu\ e^{-h\nu/kT_g}\gamma_c(\nu). \end{aligned} \tag{3.36}$$

For example, this gives us $L_h/M_h|_{free} \approx 0.02\ L_h/M_h|_{Ly\alpha}$ for $z = 10$ at an observed bandpass of $1-2\mu$m, while $L_h/M_h|_{free} \approx 0.19\ L_h/M_h|_{Ly\alpha}$ for $1-5\mu$m.

3.2.4 The Total Halo Emissivity

Figure 3.1 shows the intensity per star formation rate (SFR) produced by Pop II stars living at redshifts $z = 7-30$ in units of $\left[\text{nW m}^{-2}\ \text{ster}^{-1}/\text{M}_\odot\ \text{yr}^{-1}\ \text{Mpc}^{-3}\right]$ at varying wavelengths. The total intensity per SFR is shown as the black solid curve. The total intensity is also broken down into its separate components: the Lyman-α recombinations (dot-dashed/red), direct stellar emission (long and short dashed/green), 2-photon recombinations (dotted/yellow), and free-free and free-bound emission (short dashed/blue). The Pop II stellar population is characterized by a Salpeter IMF ranging in mass from $3-150\text{M}_\odot$ and a SF efficiency, $f_\star = 0.1$. Figure 3.2 shows the same for a population of Pop III stars ranging in mass from $3-150\text{M}_\odot$ with a Salpeter IMF and $f_\star = 0.1$.

The Lyman-α and stellar continuum contributions are the dominant processes for most of the NIR band; the Lyman-α component is the leading contributor between approximately $1-2\mu$m and is more overpowering in the Pop III case since the Lyman-α emission is directly proportional to the stellar ionizing efficiency and receives a large boost from the higher Pop III $\bar{\epsilon}_b$. The Lyman-α emission is also directly proportional to the SFR, which gives it its slope towards smaller wavelengths (where the emission is coming from galaxies at higher redshifts). At

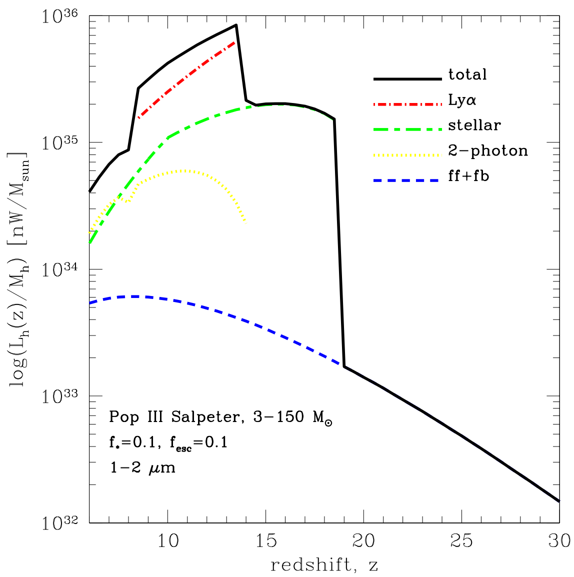

Figure 3.3: The total halo luminosity per halo mass in units of [nW/M$_\odot$], for a threshold mass, $M_{\rm min} = 10^9 {\rm M}_\odot$, at varying redshift, z. We break down the total $L_h(z)/M_h$ (black solid curve) into its various components: the Lyman-α contribution from recombinations (dot-dashed/red), direct stellar emission (long and short dashed/green), 2-photon recombinations (dotted/yellow), and free-free and free-bound emission (short dashed/blue). The halo has an escape fraction, $f_{esc} = 0.1$ and is harboring a population of Pop III stars ranging in mass from $3 - 150 {\rm M}_\odot$ with a Salpeter IMF and SF efficiency, $f_\star = 0.1$, over a bandpass of $1 - 2\mu$m.

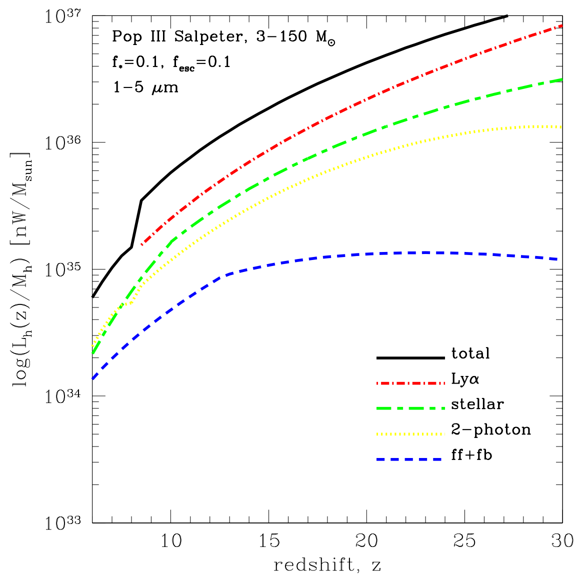

Figure 3.4: The total halo luminosity per halo mass in units of [nW/M$_\odot$], for a threshold mass, $M_{\rm min} = 10^9 M_\odot$, at varying redshift, z. We break down the total $L_h(z)/M_h$ (black solid curve) into its various components: the Lyman-α contribution from recombinations (dot-dashed/red), direct stellar emission (long and short dashed/green), 2-photon recombinations (dotted/yellow), and free-free and free-bound emission (short dashed/blue). The halo has an escape fraction, $f_{esc} = 0.1$ and is harboring a population of Pop III stars ranging in mass from $3-150 M_\odot$ with a Salpeter IMF and SF efficiency, $f_\star = 0.1$, over a bandpass of $1-5\mu$m.

these very early times, f_{coll} (and also the SFR; see equation 4.2) is growing rapidly.

The stellar continuum experiences a cut-off at $\sim 1\mu$m due to the truncation of the stellar blackbody above 13.6 eV (we assume that all of the ionizing photons are absorbed), while the two-photon continuum component cuts off at the high wavelength Lyman-α cutoff (also close to 1μm), since two-photon decay cannot produce a photon that is more energetic than a Lyman-α photon. The rocky free-free + free-bound continuum is so because of the summation over discrete hydrogen energy levels when computing the free-bound portion of the continuum coefficient (see equation 3.35).

Figure 3.3 shows the total halo luminosity per halo mass in units of [nW/M$_\odot$], for a threshold mass, $M_{\rm min} = 10^9$M$_\odot$, at varying redshift, z. We break down the total $L_h(z)/M_h$ (black solid curve) into its various components: the Lyman-α contribution from recombinations (dot-dashed/red), direct stellar emission (long and short dashed/green), 2-photon recombinations (dotted/yellow), and free-free and free-bound emission (short dashed/blue). The halo has an escape fraction, $f_{esc} = 0.1$ and is harboring a population of Pop III stars ranging in mass from $3 - 150$M$_\odot$ with a Salpeter IMF and SF efficiency, $f_\star = 0.1$, over a bandpass of $1 - 2\mu$m. Figure 3.4 represents the same halo harboring an identical stellar population over a bandpass of $1 - 5\mu$m.

As in Figures 3.1 and 3.2, the dominant contributors to the halo luminosites are the Lyman-α and direct stellar continuum processes. What is evident here is how the waveband under consideration selects galaxies in certain redshift bins. For example, Figure 3.3 ($1-2\mu$m) only samples Lyman-α emission from galaxies living between $z \sim 9-14$. This drastically alters the shape of the total luminosity. In Figure 3.4 ($1-5\mu$m), all of the various components' shapes have been preserved (when not accounting for their respective high-redshift cut-offs) except for the free-free + free-bound component. This component only appears to change shape; in fact the free-bound portion of the total gets cut-off in the top panel but remains

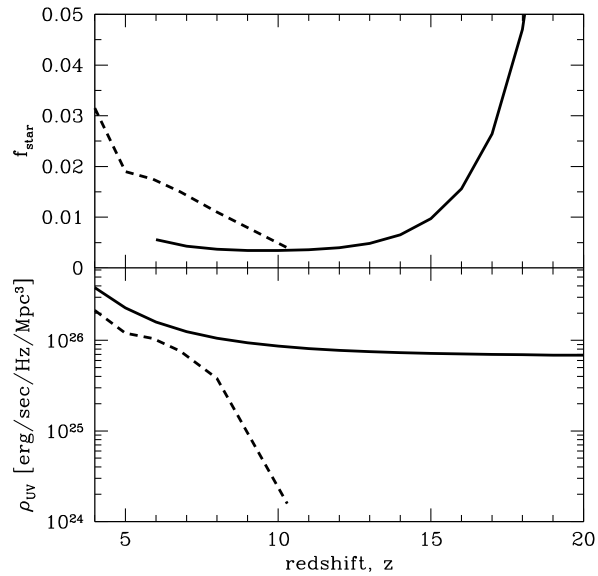

Figure 3.5: *Bottom panel:* The UV luminosity density at high redshift. The solid curve traces equation 14 from [Robertson et al., 2013] using maximum likelihood parameters for a scenario of contributing galaxies with $M_{\rm UV} < -13$. The dashed curve represents results from [Oesch et al., 2012] and [Bouwens et al., 2013] with $M_{\rm UV} < -18$. *Top panel:* Our fits to $f_\star$ while matching UV luminosities to those values from [Robertson et al., 2013] (solid curve) and [Oesch et al., 2012] (dashed curve).

in the bottom panel and boosts the amplitude at high z.

3.2.5 The UV Luminosity Density and Star Formation Efficiency

In this section we will use recent observations of the UV luminosity density to constrain our SF efficiency parameter, $f_\star$. The UV luminosity density at high redshift ($z > 8$) has recently been embroiled in intense controversy. Though there is a general consensus that the cosmic SFR declines measuredly between $z \sim 4-8$ [Bouwens et al., 2007, Bouwens et al., 2011b], whether or not this trend continues to high redshift is up for debate. Field searches scouring the HUDF under the UDF09 program [Bouwens et al., 2011b] with HST could indicate a steep drop off in the UV luminosity density for $z > 8$ i.e. a rapid evolution in the galaxy population [Bouwens et al., 2011a, Oesch et al., 2012, Bouwens et al., 2013]. However, even more recent field searches under the UDF12 campaign [Ellis et al., 2013] paint a scenario with a smoother decline in the high redshift SFR which is more consistent with a simple linear extrapolation of the $z \sim 8$ trends to earlier times.

The CLASH survey [Postman et al., 2012], which uses HST data to identify strongly lensed high redshift galaxies hiding behind low redshift galaxy clusters, has also produced differing opinions. Some recent lensed searches prefer the smooth decline scenario [Zheng et al., 2012, Coe et al., 2013], however [Bouwens et al., 2013] searched even deeper in the same cluster fields and their findings leaned more towards the steep drop off scenario presented in [Oesch et al., 2012]. In this work, we will consider both sides of the debate and will generate $f_\star$ values using observations favoring both the steep drop off and smooth decline scenarios (see the dashed and solid curves, respectively, in the bottom panel of Figure 3.5).

[Robertson et al., 2013] fused the results from the UDF12 campaign [Ellis et al., 2013] and WMAP-9 [Hinshaw et al., 2012] to develop a simple model for the evolution of the UV luminosity density:

$$\rho_{\rm UV}(z) = \rho_{{\rm UV},z=4}\left(\frac{z}{4}\right)^{-3} + \rho_{{\rm UV},z=7}\left(\frac{z}{7}\right)^{\gamma}, \tag{3.37}$$

where $\log\rho_{{\rm UV},z=4} = 26.50$ log erg sec^{-1} Hz^{-1} Mpc^{-3}, $\log\rho_{{\rm UV},z=7} = 25.82$ log erg sec^{-1} Hz^{-1} Mpc^{-3}, and $\gamma = -0.003$ for a galaxy population that extends to an absolute UV limiting magnitude of $M_{\rm UV,lim} = -13$ (see the solid curve in the bottom panel of Figure 3.5).

We can calculate the total luminosity density, $\bar{\rho}_L$, by integrating over the luminosity function (LF), $\Phi(L, z)$:

$$\bar{\rho}_L(z) = \int_{L_{\rm lim}}^{\infty} dL\ L\Phi(L, z). \tag{3.38}$$

We follow [Muñoz and Loeb, 2011] in developing an expression for the LF:

$$\Phi(L,z) = \int_{M_{\rm min}}^{\infty} dm \frac{dn(z)}{dm}\frac{dP(L|m)}{dL}, \tag{3.39}$$

where $dn(z)/dm$ is the halo mass function [Sheth and Tormen, 1999], $L(M_{\rm min}) = L_{\rm lim}$. Rather than assume unrealistically that there is only a single halo mass that corresponds to a particular luminosity, we can incorporate a luminosity distribution into our model, such that $dP(L|m)/dL$ is the probability that a halo of mass, m, has luminosity, L. We can approximate the distribution of luminosities produced by halos of a given mass as a log-normal distribution:

$$\frac{dP}{d\log L} = \frac{1}{\sqrt{2\pi\sigma_L^2}} \exp\left\{-\frac{[\log(L/L_c)]^2}{2\sigma_L^2}\right\}, \tag{3.40}$$

with a standard deviation $\sigma_L \sim 0.25$, and where $L_c = (M_h/10^{10}{\rm M}_\odot)L_{10}$, and L_{10} is the mean UV luminosity of a $10^{10}{\rm M}_\odot$ halo.

Following the galaxy formation model described in [Muñoz, 2012], the accretion of baryons by a dark matter halo directly traces that halo's mass growth rate. From [McBride et al., 2009], we can approximate the high-redshift baryon accretion rate as:

$$\dot{M}_{\rm acc} = 3\ {\rm M}_\odot/{\rm yr}\left(\frac{M_h}{10^{10}{\rm M}_\odot}\right)^{1.127}\left(\frac{1+z}{7}\right)^{2.5}\left(\frac{f_b}{0.16}\right), \tag{3.41}$$

where f_b is the cosmic baryon fraction, Ω_b/Ω_m. Assuming a fixed UV luminosity (at 1500 Å), L, to SFR ratio, we can write:

$$L = f_\star A \cdot C_t M_{\rm acc}, \tag{3.42}$$

where $A = 3.01\times10^{28}$ [erg/sec/Hz/(M$_\odot$/yr)] for a $0.04Z_\odot$ stellar population with Salpeter IMF in the mass range $3-100{\rm M}_\odot$ and C_t is a renormalization factor that is calculated as follows.

In order to enforce consistency with our formalism presented in §3.2.1, we will need to renormalize the baryon accretion rate in eqn 3.41. We do this by setting the renormalization factor, C_t, such that the SF timescale of all star-forming halos matches the universal value given by the collapse fraction, $f_{\rm coll}$ (discussed in section 3.2.1). The SF timescale (which in this case is not independent of halo mass) can be written as:

$$t_{\rm SF}(M_h, z) = \frac{M_h}{\dot{M}_h} = \frac{f_b M_h}{C_t \dot{M}_{\rm acc}}, \tag{3.43}$$

where the average timescale, $\bar{t}_{\rm SF}(M_{\rm min}, z)$, averaged over all halo masses is:

$$\frac{1}{\bar{t}_{\rm SF}(M_{\rm min}, z)} = \frac{\int_{M_{\rm min}}^{\infty} dm\ m\ n(m)/t_{\rm SF}(m)}{\int_{M_{\rm min}}^{\infty} dm\ m\ n(m)}, \tag{3.44}$$

where $n(m)$ is the halo mass function for a halo with mass, m, for which we use the [Sheth and Tormen, 1999] version. We require that $\bar{t}_{\rm SF}(M_{\rm min}, z) = [d\ ln\ f_{\rm coll}(z)/dt]^{-1}$, so we choose C_t such that the following is true:

$$\dot{f}_{\rm coll}(z) = \int_{M_{\rm min}}^{\infty} \frac{dm\ n(m) \cdot C_t \dot{M}_{\rm acc}}{\bar{\rho}_b(z)}. \tag{3.45}$$

For example, the 3 $\mathrm{M_\odot}$/yr out in front of eqn 3.41 turns into a 4.5 $\mathrm{M_\odot}$/yr ($z = 6$) and a 10.2 $\mathrm{M_\odot}$/yr ($z = 15$) for $M_{\rm min} = 2.2 \times 10^9$ $\mathrm{M_\odot}$. When modeling the total radiation background, we must account for all halos that are large enough to actually host stars, or all halos with mass $M > M_{\rm min}$. To motivate our choices for $M_{\rm min}$, we first consider the 'filter mass,' $M_{\rm filter}$, the characteristic scale over which baryonic perturbations are smoothed in linear perturbation theory or the minimum mass of a halo to accrete baryons [Gnedin and Hui, 1998, Naoz and Barkana, 2007], as a lower limit ($\sim 10^5 \mathrm{M_\odot}$ in our redshift regime). In linear theory, the relative force balance between gravity and pressure can be characterized by the Jeans mass, M_J; the corresponding Jeans scale is the minimum scale on which a small perturbation will grow due to gravity. M_J depends on the instantaneous value of the sound speed of the gas, consequently overestimating the characteristic mass scale by up to an order of magnitude [Gnedin, 2000]. In contrast, $M_{\rm filter}$, which takes into account the full thermal history of the gas, is a more accurate mass scale.

An upper limit would be the threshold for atomic cooling, $T_{\rm vir} \sim 10^8$K [Oh and Haiman, 2002]. Since the H_2 fraction, f_{H_2}, increases with halo mass ($f_{H_2} \propto T_{\rm vir}^{1.5}$, [Tegmark et al., 1997]) the cutoff mass certainly lies somewhere between these two limits. Rather than try to model this in detail we will employ a variety of selections for $M_{\rm min}$ in order to remain most general.

In the context of our model, we can arbitrarily choose plausible values for the SF efficiency in order to estimate the total NIRB emission from Pop III stars. We can also generate observationally motivated values by tuning $f_\star$ such that our predicted total UV luminosity density (equation 3.38) matches observations for all redshifts. We perform this matching against both the steep drop-off scenario of [Oesch et al., 2012] and the smooth decline scenario of [Robertson et al., 2013]. The solid curve in the bottom panel of Figure 3.5 (or equivalently, equation 3.37) represents the [Robertson et al., 2013] model of the luminosity density. The dashed curve represents the [Oesch et al., 2012] results; specifically, an exponential fit to the UV luminosity density measurements of [Bouwens et al., 2007, Bouwens et al., 2011b] at $z \sim 4-8$ and [Oesch et al., 2012] at $z \sim 10$.

Results for $f_\star$ tuned to [Robertson et al., 2013] (solid curve) and [Oesch et al., 2012] (dashed curve) are shown in the top panel of Figure 3.5. In the case of the solid curve, the trajectory of $f_\star$ is basically flat for $z < 13$ and increases steeply at higher redshifts in order to maintain a smooth luminosity density even while the halo population is falling sharply at those times. For the steep drop-off case (dashed curve), even though the luminosity density is less than that of the smooth decline case, $f_\star$ must be higher in order to make up for the smaller galactic population probed by the [Oesch et al., 2012] magnitude limited galaxy hunt. Since we expect the NIRB coming from Pop III at the highest redshifts to be very small anyway, we will optimistically assume the dashed curve to be a simple plateau extending to very early epochs.

We use our fits for $f_\star$ to generate model UV LFs in Figure 3.6 at redshifts $z = 6$ (top panel) and $z = 8$ (bottom panel). Solid curves use $f_\star$ values matched to the [Robertson et al., 2013] UV luminosity density, while the dashed curves use $f_\star$ values matched to the [Oesch et al., 2012] results. The observed UV LFs are represented by the dotted curves in both panels. At $z = 6$, we compare to the best-fit Schechter parameters from [Bouwens et al., 2007], who calculated the UV LF at $z \sim 4, 5$, and 6 after building large samples of star forming galaxies from the HUDF and deep HST ACS fields. At $z = 8$, we compare to the best-fit Schechter parameters from [McLure et al., 2012] based on UDF12 data. Both of our $f_\star$ fits provide quite reasonable matches to observations to date, while the [Oesch et al., 2012] fit achieves the closest match for both redshifts.

3.3 The Mean NIRB Excess

As discussed in §3.1, the mean NIRB has been measured using DIRBE on board the *COBE* [Gorjian et al., 2000, Wright and Reese, 2000, Cambrésy et al., 2001, Wright, 2001, Wright and Johnson, 2001, Levenson et al., 2007] and also using NIRS on board the *IRTS* [Matsumoto et al., 2005]. The DIRBE measurements, in the J (1.25μm), K (2.2μm), and L (3.5μm) bands, are tabulated in Table 3.1; the NIRS measurements in numerous bands are shown in Figure 3.7 and tabulated in [Matsumoto et al., 2005].

In order to determine the mean NIRB excess, we must subtract the contribution of normal galaxies from the observed values in Table 3.1. There are several galactic integrated source counts available in the NIR, which are listed in Table 3.2. [Madau and Pozzetti, 2000] and [Cambrésy et al., 2001] present compilations of deep *HST* space-based and also ground-based galaxy counts. We also include

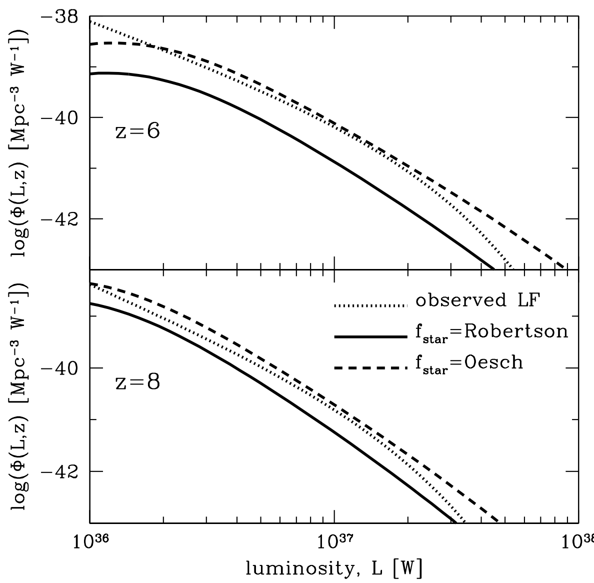

Figure 3.6: Our modeled UV LF (solid and dashed curves) compared to observed LFs (dotted curves) at corresponding redshifts. The solid curves represent our model using $f_\star$ values matched to the [Robertson et al., 2013] UV luminosity density, while the dashed curves use $f_\star$ values matched to the [Oesch et al., 2012] results. The top panel is at redshift $z = 6$ and displays the best-fit LF according to measurements by [Bouwens et al., 2007]. The bottom panel is at redshift $z = 8$ and displays the best-fit LF from high-redshift observations in [McLure et al., 2012].

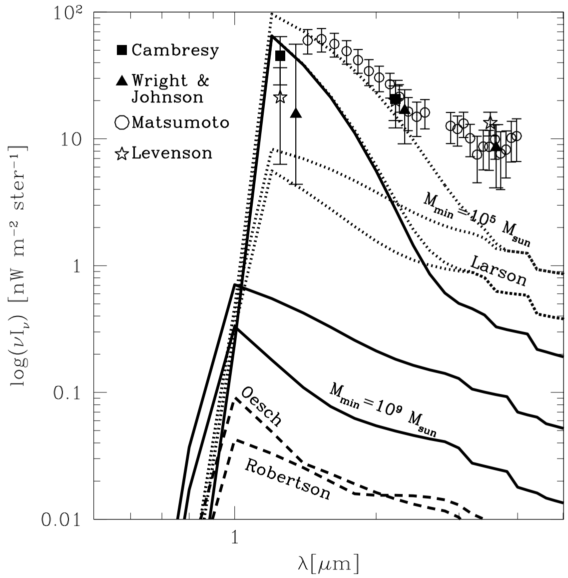

Figure 3.7: The mean NIRB intensity produced by varying populations of Pop III stars. Solid curves represent a population from $3 - 150\mathrm{M}_\odot$ with a Salpeter IMF. All of these curves have $M_{\rm min} = 10^7\mathrm{M}_\odot$ with the exception of the middle curve labeled as $M_{\rm min} = 10^9\mathrm{M}_\odot$. The bottom most dashed curves have the same population but use $f_\star(z)$ calibrated using the UV luminosity densities from [Oesch et al., 2012] (top curve) and [Robertson et al., 2013] (bottom curve). The top most solid curve uses $\epsilon_b = 10^6$ photons per baryon and $f_\star = 0.5$, while the remaining solid curves use $\bar{\epsilon}_b \sim 30,000$ and $f_\star = 0.1$. There are two sets of dotted curves, both representing a population from $1 - 1000\mathrm{M}_\odot$ with a Larson ($m_c = 100\mathrm{M}_\odot$) IMF and $f_\star = 0.5$. The bottom pair and top pair use $M_{\rm min} = 10^7$ and $M_{\rm min} = 10^5\mathrm{M}_\odot$ respectively. For each pair, the bottom and top curves use $\bar{\epsilon}_b \sim 78,000$ and $\epsilon_b = 10^6$ photons per baryon respectively. We also plot data for the observed mean NIRB excess from [Cambrésy et al., 2001] (solid squares), [Wright and Johnson, 2001] (solid triangles), [Matsumoto et al., 2005] (open circles), and [Levenson et al., 2007] (open stars). See Tables 3.1 and 3.2 for these values.

counts from other deep surveys, such as the Subaru Deep Field [Totani et al., 2001] and surveys using the Infrared Array Camera (IRAC) on board *Spitzer* [Fazio et al., 2004].

Indeed the galactic contributions cited above do not make up the entire observed NIRB, leaving a discernible excess. But can Population III stars make up for the entire observed excess? In Figure 3.7 we present our modeled mean NIRB intensity (explicitly equation 3.1) for various populations of Pop III stars directly compared to observations using DIRBE (dark squares: [Cambrésy et al., 2001]; dark triangles: [Wright and Johnson, 2001]) and *IRTS* (open circles: [Matsumoto et al., 2005]). The data presented here are actually representative of the observed excess. We calculated the DIRBE observed excess by subtracting galaxy count data from [Cambrésy et al., 2001] for the J and K bands and data from [Fazio et al., 2004] for the L band. The *IRTS* excess was calculated by subtracting an exponential fit to the two values in the J and K bands recorded in [Totani et al., 2001] from the [Matsumoto et al., 2005] data.

The bottom most dashed curves represent a stellar population from $3-150\mathrm{M}_{\odot}$ with a Salpeter IMF, living in galaxies at redshifts $z = 8-30$ with a threshold halo mass of $M_{\min} = 10^7\mathrm{M}_{\odot}$. The average stellar ionizing efficiency, $\bar{\epsilon}_b$, is calculated with equation 4.13 (in this case, $\bar{\epsilon}_b = 29,947$). Both curves use $f_\star(z)$ calibrated with the UV luminosity densities from [Oesch et al., 2012] (top curve) and [Robertson et al., 2013] (bottom curve). These models generated from observationally motivated parameters live approximately three orders of magnitude below observations. In order to boost the amplitude of our model and theorize a stellar population that is capable of coming closer to accounting for the entire observed NIRB intensity excess, we can, to start with, decrease $M_{\min}$ so that there are more halos forming stars or increase $f_\star$ such that each halo forms more stars. The bottom two solid curves represent the same stellar population with the same stellar ionizing efficiency as the dashed curves, but use a constant star formation efficiency, $f_\star = 0.1$. All solid curves use $M_{\rm min} = 10^7{\rm M}_\odot$ with the exception of the bottom most solid curve labeled as $M_{\rm min} = 10^9{\rm M}_\odot$. It is apparent that decreasing the threshold halo mass by a factor of 10^2 and/or modestly increasing $f_\star$ to 10% for all redshifts is not sufficient to boost the amplitude enough to be comparable to observations.

Still more, we can pump up the stellar ionizing efficiency, ϵ_b, to further boost the amplitude of the intensity. The top most solid curve uses identical parameters to the dashed curves excepting for ϵ_b and $f_\star$ which are pumped up to 10^6 photons per baryon and 0.5 respectively. Though the amplitude is boosted significantly at the 1μm break, the amplitude at higher wavelengths is still too low. Simply assigning an extremely high ϵ_b to a $3-150{\rm M}_\odot$ Salpeter population is not sufficient- doing this will only boost the Lyman-α peak at $\sim 1\mu$m but will not boost the tail end of the NIR intensity out towards $3-5\mu$m, which is made up of direct stellar emission and the free-free and free-bound continuum emission. The tail end is also where the populations at the highest redshifts contribute. These contributions are much smaller due to the steep decline in structure formation at these early times. This results in a much steeper trajectory towards smaller wavelengths and up to the Lyman-α break, while data suggests a more measured incline. By altering the stellar IMF to a more top-heavy Larson model, such that there are more massive stars contributing with their higher ionizing efficiencies, we can boost the tail and trace the shape of the data more closely. There are two sets of dotted curves, both representing a population from $1-1000{\rm M}_\odot$ with a Larson ($m_c = 100{\rm M}_\odot$) IMF (identical to the 'very heavy' IMF utilized in [Salvaterra and Ferrara, 2003]) and $f_\star = 0.5$. The bottom pair and top pair use $M_{\rm min} = 10^7{\rm M}_\odot$ and $M_{\rm min} = 10^5{\rm M}_\odot$ respectively. For each pair, the bottom and top curves use $\bar{\epsilon}_b = 77,686$ (calculated with equation 4.13) and $\epsilon_b = 10^6$ photons per baryon respectively. Not just one of our model parameters can be modestly adjusted in order to match observations; we require all parameters to be simultaneously pumped up in order to reach the desired amplitude.

We find that in order to match the observed excess with a model based exclusively on Pop III stars, we would need ionizing efficiencies well beyond those provided by [Schaerer, 2002] by at least an order of magnitude. We would need an extraordinarily top-heavy stellar IMF that extends out to at least $\sim 1000\mathrm{M}_{\odot}$. Such a mass function might help with the chemical over enrichment dilemma as more stars with $M > 250\mathrm{M}_{\odot}$ would wind up as black holes and store their metals. However, a larger black hole population may over produce the X-ray background. Further, recent observations of high redshift gamma-ray sources disfavor significant Pop III SF at $z \sim 6-8$ with top-heavy IMFs [Gilmore, 2012]. In addition, we would need a very low threshold halo mass, M_{min}, indicating that Pop III SF would have to persist in minihalos until $z \sim 8$. Minihalos can only continue forming Pop III stars while their supplies of their primary coolant, molecular hydrogen H_2, remain intact– molecular hydrogen is dissociated by Lyman-Werner (LW; $11.5-13.6$ eV) UV radiation that is produced by companion minihalos that have already formed stars. This scenario seems rather unlikely at such late times as the cosmic LW BG is thought to have surpassed the threshold for H_2 destruction well before $z \sim 15$ [Holzbauer and Furlanetto, 2012]. Additionally, the LW BG is very smooth at threshold [Holzbauer and Furlanetto, 2012], indicating that it is improbable that any lone minihalos still live in 'safe' patches with low LW levels, allowing further Pop III SF there.

Table 3.1: Summary of Data for the Total Mean NIRB Intensity

J band (1.25 μm)	K band (2.2 μm)	L band (3.5 μm)	References
...	22.4 ± 6.0	11.0 ± 3.3	[Gorjian et al., 2000]
...	23.1 ± 5.9	12.4 ± 3.2	[Wright and Reese, 2000]
54.0 ± 16.8	27.8 ± 6.7	...	[Cambrésy et al., 2001]
28.9 ± 16.3	20.2 ± 6.3	...	[Wright, 2001]
24.3 ± 18	24.0 ± 6.0	13.8 ± 3.4	[Wright and Johnson, 2001]
21.3 ± 15.0	20.03 ± 6.1	13.4 ± 2.9	[Levenson et al., 2007]

Notes.—Observed cosmic background intensity after subtracting zodiacal light and galactic stellar light foregrounds. Units of intensity given in [nW m^{-2} ster^{-1}].

Table 3.2: Summary of Data for the Mean NIRB Arising from Galaxies

J band (1.25 μm)	H band (1.65 μm)	K band (2.2 μm)	L band (3.5 μm)	(4.5 μm)	References
$9.71^{+3.0}_{-1.9}$	$9.02^{+2.62}_{-1.68}$	$7.92^{+2.04}_{-1.21}$	...	...	[Madau and Pozzetti, 2000]
8.64 ± 1.92	...	7.23 ± 1.64	...	...	[Cambrésy et al., 2001]
...	...	...	5.27 ± 1.02	3.95 ± 0.77	[Fazio et al., 2004]
10.9 ± 1.1	...	8.3 ± 0.8	...	...	[Totani et al., 2001]

Notes.—Integrated cosmic background intensity arising from galaxy counts, or the contribution to the NIRB from normal galaxies. Units of intensity given in [nW m^{-2} ster^{-1}].

3.4 The Power Spectrum

The mean NIRB could be as high as $\sim 70 - 80$ nW m^{-2} ster^{-1} and as low as ~ 10 nW m^{-2} ster^{-1} (see Table 3.1 and Figure 3.7). The integrated flux count in the NIR from normal galaxies is currently estimated to be on the order of 10 nW m^{-2} ster^{-1} (see Table 3.2). In lieu of this uncertainty, a possible NIRB excess which could be a signature of Pop III stars or even another as yet undiscovered source population, could be as strong as ~ 60 nW m^{-2} ster^{-1} or virtually a red herring.

The accuracy of mean NIRB observations to date remains relatively dubious, however measuring *fluctuations* in the background may be more forgiving because they are less sensitive to zodiacal light subtraction (zodiacal light is very smooth). In this section we will use the halo model to predict the 3D PS and angular PS of NIRB fluctuations produced by Pop III stars and will compare our results to observations. Have we found a way to indirectly delve into the mysterious properties of the first luminous sources in our universe?

3.4.1 Methodology

Here we will discuss modeling the power spectrum of fluctuations in the NIRB using the halo model. The halo model, as described in [Cooray and Sheth, 2002], uses properties of virialized dark matter halos to calculate the effects of non-linear gravitational clustering, assuming that all mass in the universe is compartmentalized in such halos, whose properties can be parameterized purely by their mass m. The three ingredients of the model are the (1) halo number density, $n(m)$, (2) spatial distribution of the halos, and (3) distribution of mass within each halo, or halo density profile, $\rho(r|m)$, (where r is the distance away from the center of a halo with mass m). Typically, a theoretically-motivated halo mass function for (1) (the classic choice being [Press and Schechter, 1974]) allows one to calculate

(2). The density profile for (3) can be calibrated by numerical simulations, such as the NFW [Navarro et al., 1996] or [Moore et al., 1999] profiles. This model is very powerful in that it can efficiently determine the power and many other useful properties for any density field at any arbitrary epoch and scale.

Since we wish to quantify the radiation background rather than the mass density field, we simply replace the 'halo density profile' with the profile of the radiation field around each halo. This flux profile, $\rho_{\rm rad}(r|m)$, is unique for each radiation background under consideration. For a spherically symmetric profile, the normalized Fourier transform, $u(k|m)$, can be written as:

$$u(k|m) = \frac{\int_0^\infty dr 4\pi r^2 [\sin(kr)/(kr)]\rho_{\rm rad}(r|m)}{\int_0^\infty dr 4\pi r^2 \rho_{\rm rad}(r|m)}. \tag{3.46}$$

As described above, we can adjust the halo model to describe the fluctuations in a variety of radiation backgrounds, focusing on the NIRB in this paper. We use the power spectrum, $P(k)$, or the dimensionless quantity $\Delta(k) \equiv k^3 P(k)/2\pi^2$ to quantify these fluctuations. Following the halo model, we write the power as a sum of two terms: the first term, $P^{\rm 1h}(k)$ ('one-halo' term), describes the case for which radiation at two points comes from the same source, while the second term, $P^{\rm 2h}(k)$ ('two-halo' term), describes the case for which the two points are illuminated by two sources:

$$\begin{aligned} P(k) &= P^{\rm 1h}(k) + P^{\rm 2h}(k), \text{where} && (3.47)\\ P^{\rm 1h}(k) &= \int_{M_{\rm min}}^\infty dm n(m) \left(\frac{m}{\bar{\rho} f_{\rm coll}}\right)^2 |u(k|m)|^2 && (3.48)\\ P^{\rm 2h}(k) &= \left[\int_{M_{\rm min}}^\infty dm n(m) \left(\frac{m}{\bar{\rho} f_{\rm coll}}\right) u(k|m) b(m)\right]^2 P^{\rm lin}(k). && (3.49) \end{aligned}$$

Here, $\bar{\rho}$ is the matter density, $f_{\rm coll}$ is the collapse fraction (fraction of mass in the universe contained in galaxies, or collapsed in a halo), $b(m)$ denotes the halo bias (describing how strongly clustered the halos are; [Mo and White, 1996]), and lastly $P^{\rm lin}(k)$ is the linear power spectrum. Here we have approximated the halo-halo power spectrum, for two halos with mass m_1 and m_2, as $b(m_1)b(m_2)P^{\rm lin}(k)$, which requires that the halo fluctuations remain linear on the appropriate scales (i.e., those on which P^{2h} dominates). While the density fluctuations themselves are very weak at the redshifts of interest to us, the halos are also highly biased, so nonlinear corrections will be important on sufficiently small scales. We use the [Eisenstein and Hu, 1999] fit to the transfer function to calculate $P^{\rm lin}(k)$ and the Sheth-Tormen mass function and collapse fraction [Sheth and Tormen, 1999].

In the case of the NIRB, recall that each individual halo's contribution to the BG is made up emission emanating from the galaxy itself and reprocessed emission from the surrounding IGM. The total emission is made up of three components, two of which constitute the galaxy emission. These galactic components are the direct stellar emission and indirect emission that is made up of the fraction, $(1 - f_{\rm esc})$, of ionizing photons that do not escape into the IGM and carve out HII regions within the galaxy where recombinations take place. The IGM component is made up of indirect emission that comes about after the Lyman limit systems (LLS) surrounding the central source absorb the fraction, $f_{\rm esc}$, of ionizing photons that have escaped the central galaxy. These photons either produce free-free continuum emission or recombine and result in free-bound and 2-photon continuum emission and Lyman-α line emission.

We shall simply model the galactic emission components as delta functions; this component is only nonzero at the center of the galaxy which lies at the center of the halo. This approximation is sufficient since we are only interested in NIRB fluctuations on large scales and we are not concerned with variations in emissivity within the halo. Galactic Lyman-α photons do not contribute to the total emissivity at larger radii, $r > 0$, because they are emitted from the central galaxy and redshift out of the Lyman-α resonance by the time they reach the outlying absorbing systems (we assume the absorbers are living sufficiently far away from the center that this is true).

However, the IGM component is more complicated as these recombinations take place over a more extended volume. In previous studies, this component has either been ignored or treated very simply. To generate $\rho_{\rm rad}(r)$ for the IGM, we basically need to determine the brightness of recombinations around each source. As the Lyman-α photons dominate the nebular emission, we will only focus on these photons for simplicity. Consider a central source producing a flux of ionizing photons, $F_i(r)$, such that $F_i(r) = L_i/4\pi r^2$ (where L_i is the ionizing source luminosity). If we assume that the LLSs are everywhere in space, we can write the probability that an ionizing photon is absorbed within a distance, r, from the central source as:

$$p_{\rm abs}(< r) = 1 - e^{-\tau(r)}, \tag{3.50}$$

where the optical depth, $\tau(r) = r/\lambda$ and λ is the photon's mean free path (we use a value of 10 cMpc; see section 4.4.1 in [Loeb and Furlanetto, 2013]). This gives us a probability of absorption at distance, r, as $p_{\rm abs}(r) = dp(< r)/dr = \lambda^{-1}e^{-r/\lambda}$. If we assume that one recombination occurs each time a photon is absorbed, and taking into account that $\sim 2/3$ of those recombinations will produce a Lyman-α photon, then the flux of Lyman-α recombinations emanating from the central source can be written as $F_{\rm recomb}(r) = (2/3)F_i(r)p_{\rm abs}(r)$ or:

$$\rho_{\rm rad,NIR}(r) = \frac{2}{3\lambda}\frac{L_i}{4\pi r^2}e^{-r/\lambda}, \tag{3.51}$$

which gives us a normalized Fourier Transform of:

$$u_{\rm NIR}(k) = \frac{\arctan(k\lambda)}{k\lambda}. \tag{3.52}$$

In order to calculate the average volume emissivity of each component, $\bar{\epsilon}(z)$, we integrate the NIR luminosity per halo mass over the halo mass function:

$$\bar{\epsilon}_i(z) = \int_{M_{\rm min}}^{\infty} dm n(m) m \frac{L_{h,i}(z)}{M_h}, \tag{3.53}$$

where $\bar{\epsilon}_i(z)$ is the average volume emissivity arising from component i and $L_{h,i}(z)/M_h$ is the luminosity per halo mass of component i. The galaxy component of the average volume emissivity, $\bar{\epsilon}_\delta(z)$, can be written as:

$$\bar{\epsilon}_\delta(z) = \bar{\epsilon}_\star(z) + (1 - f_{\rm esc}) \left[\bar{\epsilon}_{{\rm Ly}\alpha}(z) + \bar{\epsilon}_{2\gamma}(z) + \bar{\epsilon}_{\rm ff+fb}(z)\right]. \tag{3.54}$$

The recipe for this delta component obviously has no 'one-halo' ingredient and is exclusively characterized by a 'two-halo' term:

$$P_\delta^{\rm 1h}(k) = 0 \tag{3.55}$$

$$P_\delta^{\rm 2h}(k) = \bar{\epsilon}_\delta^2(z) \left\{\int_{M_{\rm min}}^\infty dm n(m) \left[\frac{b(m)}{\bar{n}_{\rm gal}}\right]\right\}^2 P^{\rm lin}(k), \tag{3.56}$$

where $\bar{n}_{\rm gal}$ is the average galaxy number density, which we obtain by integrating over the halo mass function (assuming each halo has one galaxy sitting at its center):

$$\bar{n}_{\rm gal} = \int_{M_{\rm min}}^\infty dm n(m). \tag{3.57}$$

The second component, or IGM component, is made up of the LLSs that absorb the ionizing photons radiating from the central galaxy; it includes both 'one-halo' and 'two-halo' terms:

$$P_{\rm IGM}^{\rm 1h}(k) = \bar{\epsilon}_{\rm IGM}^2(z) \int_{M_{\rm min}}^\infty dm n(m) \left(\frac{m}{\bar{\rho} f_{\rm coll}}\right)^2 |u(k)|^2 \tag{3.58}$$

$$P_{\rm IGM}^{\rm 2h}(k) = \bar{\epsilon}_{\rm IGM}^2(z) \left[\int_{M_{\rm min}}^\infty dm n(m) \left(\frac{m}{\bar{\rho} f_{\rm coll}}\right) u(k) b(m)\right]^2 P^{\rm lin}(k), \tag{3.59}$$

where the average volume emissivity arising from the IGM component (which comes from reprocessed ionizing photons that have escaped the central galaxy) can be written as:

$$\bar{\epsilon}_{\rm IGM}(z) = f_{\rm esc} \left[\bar{\epsilon}_{{\rm Ly}\alpha}(z) + \bar{\epsilon}_{2\gamma}(z) + \bar{\epsilon}_{\rm ff+fb}(z)\right]. \tag{3.60}$$

In addition to the clustering terms, there are also fluctuations (or shot noise) that arise from the discrete nature of the halos:

$$P_{\rm shot}(k) = \left(\frac{L_h}{M_h}\right)^2 \int_{M_{\rm min}}^\infty dm n(m) m^2. \tag{3.61}$$

And finally:

$$P_{\rm NIR}(k) = P_{\delta}^{\rm 2h}(k) + \left[P_{\rm IGM}^{\rm 1h}(k) + P_{\rm IGM}^{\rm 2h}(k)\right] + P_{\rm shot}(k). \tag{3.62}$$

Combining all of these ingredients, we can now calculate the NIR 3D PS for any redshift, allowing us to use the Limber approximation [Limber, 1954] in order to acquire the angular PS:

$$C_l = \frac{c}{(4\pi)^2}\int \frac{dz}{H(z)r^2(z)(1+z)^4} P_{\rm NIR}\left[k = l/r(z), z\right], \tag{3.63}$$

where $r(z) = c\int_0^z dz'/H(z')$ is the comoving distance and l is the multipole moment.

3.4.2 Results: The 3D Power Spectrum

In Figure 3.8 we display the total NIR ($1-5\mu$m) 3D PS for Pop III stars with a Salpeter IMF extending from $3-150{\rm M}_\odot$. The PS is calculated for redshifts (from top to bottom) $z = 6$ (black), 8 (cyan), 10 (royal blue), 15 (green), 20 (red), and 25 (magenta). We do not reasonably expect a substantial Pop III component as late as $z = 6$ but include this scenario as a comparison to previous work. Also shown are the various components that make up the total fluctuations at $z = 15$; the dotted curves are labeled as the shot noise, 'two-halo' galaxy/delta ('2h$-\delta$') component, and 'one-halo' ('1h$-$ IGM') and 'two-halo ('2h$-$ IGM') IGM components. The 'two-halo' galaxy term is integral in boosting the power above the shot noise on larger scales and shaping the fluctuations; the IGM components are in all cases several orders of magnitude smaller. All curves use $f_\star = 0.5, f_{\rm esc} = 0.1, t_{\rm SF} = f_{\rm coll}/\dot{f}_{\rm coll}$. This choice of SF efficiency is representative of an extremely optimistic scenario and produces an upper limit for the signal given a choice of stellar IMF. Solid curves use $M_{\rm min} = 10^8{\rm M}_\odot$ while dashed curves use $M_{\rm min} = 10^9{\rm M}_\odot$. Fluctuations for scenarios with the higher threshold mass are smaller, except for the lowest redshift ($z = 6$), at which point the total power achieves a

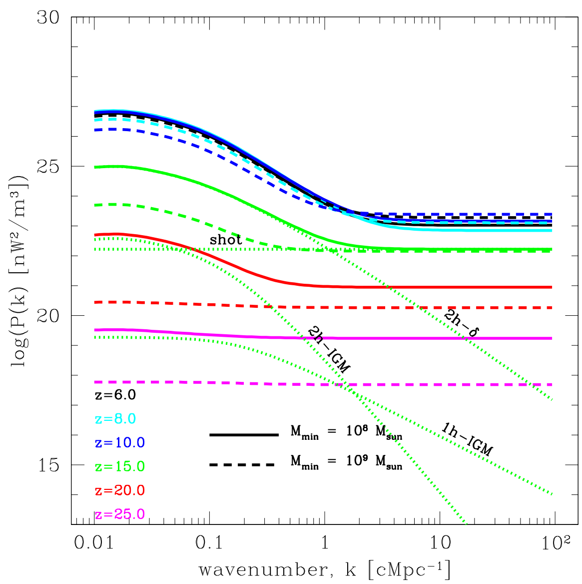

Figure 3.8: The 3D total NIR ($1 - 5\mu$m) PS for Pop III stars with a Salpeter IMF over $3 - 150\mathrm{M}_{\odot}$ calculated for redshifts (from top to bottom) $z = 6$ (black), 8 (cyan), 10 (royal blue), 15 (green), 20 (red), and 25 (magenta). Solid curves use $M_{\rm min} = 10^8\mathrm{M}_{\odot}$ while dashed curves use $M_{\rm min} = 10^9\mathrm{M}_{\odot}$. All curves use $f_{\star} = 0.5, f_{\rm esc} = 0.1, t_{\rm SF} = f_{\rm coll}/\dot{f}_{\rm coll}$. Also shown are the various components that make up the total fluctuations at $z = 15$. The dotted curves are labeled as the shot noise, 'two-halo' delta component, and 'one-halo' and 'two-halo' nebular components.

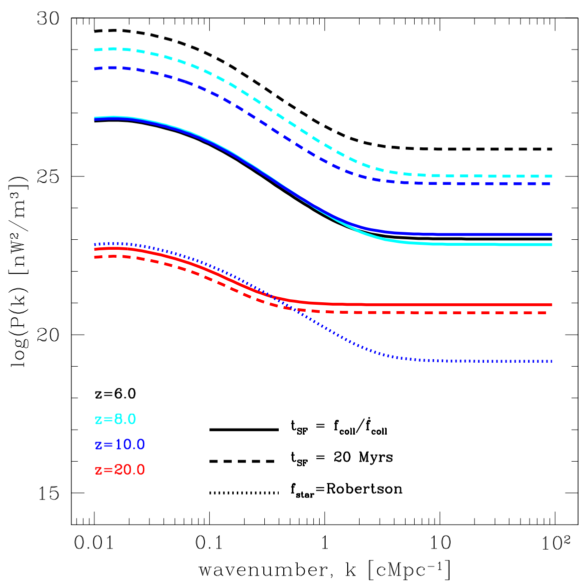

Figure 3.9: The 3D total NIR ($1-5\mu$m) PS for Pop III stars with a Salpeter IMF over $3-150\mathrm{M}_\odot$ calculated for redshifts (from top to bottom) $z=6$ (black), 8 (cyan), 10 (royal blue), and 20 (red). Solid curves use $t_{\rm SF}=f_{\rm coll}/\dot{f}_{\rm coll}$ while dashed curves use $t_{\rm SF}=20$Myrs. Solid and dashed curves use $f_\star=0.5$ while the dotted curve ($z=10$) uses $t_{\rm SF}=f_{\rm coll}/\dot{f}_{\rm coll}$ and $f_\star(z)$ calculated with the UV luminosity density from [Robertson et al., 2013]. All curves use $f_{\rm esc}=0.1, M_{\rm min}=10^8\mathrm{M}_\odot$.

ceiling that is relatively independent of $M_{\rm min}$ since at these late times, $f_{\rm coll}$ is no longer growing rapidly. The shot noise dominates towards higher redshifts and smooths out the power on larger scales, covering up the clustering contributions that harbor the clues with which to infer properties of the Pop III populations.

In Figure 3.9, we display the total NIR ($1-5\mu$m) 3D PS for Pop III stars with a Salpeter IMF over $3-150{\rm M}_\odot$ calculated for redshifts (from top to bottom) $z = 6$ (black), 8 (cyan), 10 (royal blue), and 20 (red). In this case we have chosen a constant threshold halo mass of $M_{\rm min} = 10^8{\rm M}_\odot$ and $f_{\rm esc} = 0.1$ but have varied the SF timescale; solid curves use $t_{\rm SF} = f_{\rm coll}/\dot{f}_{\rm coll}$ while dashed curves use $t_{\rm SF} = 20$ Myrs for all redshifts (as in [Fernandez et al., 2010]). In the latter case, a SF timescale of 20 Myrs indicates that the galaxy is turning its entire fraction of baryons available for SF, $f_\star$, into stars in only 20 Myrs. By assuming that the timescale varies with $f_{\rm coll}(z)$, we acquire SF timescales that are much longer than the constant value of 20 Myrs. This gives us a $t_{\rm SF}$ that reaches ~ 90 Myrs by $z = 10$ and ~ 175 Myrs by $z = 8$. A SF timescale significantly smaller than these values implies that the galaxies are cycling through their baryons and forming new stars incredibly fast.

Solid and dashed curves use $f_\star = 0.5$ while the dotted curve uses $t_{\rm SF} = f_{\rm coll}/\dot{f}_{\rm coll}$ and $f_\star(z)$ calculated with the UV luminosity density from [Robertson et al., 2013]. Evident in Figure 3.9 is that the different treatments of $t_{\rm SF}$ do not affect the shape of the power, however using a constant SF timescale does not produce a saturation effect of fluctuations at the lower redshifts as it does using the time dependent timescale. The constant $t_{\rm SF}$ case results in higher power at $z < 15$, as $t_{\rm SF}(z) = f_{\rm coll}/\dot{f}_{\rm coll}$ is rising sharply and becomes much larger than 20 Myrs, causing the luminosity per halo to fall. For $z = 20$ and 25, $t_{\rm SF}(z)$ is smaller than 20 Myrs which results in higher fluctuations. As we will see in section 3.4.3, the 3D PS at later times dominates the total angular PS. As a result, an overestimate of the 3D PS for $z < 15$ by choosing a constant SF timescale will lead to an even larger overestimate of the angular PS. In these models, a choice of SF efficiency of $f_\star = 0.5$ is extremely generous. The dotted curve uses parameters identical to the $z = 10$ solid curve except for the SF efficiency, which is calibrated to match observations. This more realistic choice of $f_\star$ decreases the $f_\star = 0.5$ signal by at least four orders of magnitude.

The shapes of our fluctuations in Figures 3.8 and 3.9 can be directly compared to the 3D PS presented in Figures 7 and 8 from [Fernandez et al., 2010], who utilized N-body simulations to describe the distribution of halos hosting these very early luminous sources. They point out that the halo bias increases substantially towards smaller scales and could affect the shape of the PS; [Mesinger and Furlanetto, 2009] found from semi-numeric simulations that non-linear clustering tends to smooth out the signature turnover in the PS of the ionizing background (where it is due to the smaller attenuation length of high-z ionizing photons). In contrast, our model assumes a linear bias when computing the 'two halo' terms in the PS. As the shot noise becomes important, our curves appear to flatten out on about the same scales as the [Fernandez et al., 2010] versions. However our clustering terms produce a slightly steeper incline towards the larger scales– [Fernandez et al., 2010] display a more gentle, eroded slope.

3.4.3 Results: The Angular Power Spectrum

In Figure 3.10 we present the NIR angular PS over the AKARI 2.4μm bandpass in units of $\left[\mathrm{nW}^2/\mathrm{m}^4/\mathrm{ster}^2\right]$, for a Pop III stellar population (Salpeter from $3 - 150\mathrm{M}_\odot$) with $f_{\rm esc} = 0.1$, $f_\star = 0.5$, contributing over a redshift range of $z = 6 - 30$. Dotted, solid, and dashed curves have a threshold mass of $M_{\rm min} = 10^6,\ 10^8,\ 10^9\mathrm{M}_\odot$ respectively. The bottom most pair of curves use star formation efficiencies obtained using the UV luminosity densities from [Robertson et al., 2013] and [Oesch et al., 2012] (see §3.2.5). All curves use $t_{\rm SF} = f_{\rm coll}/\dot{f}_{\rm coll}$.

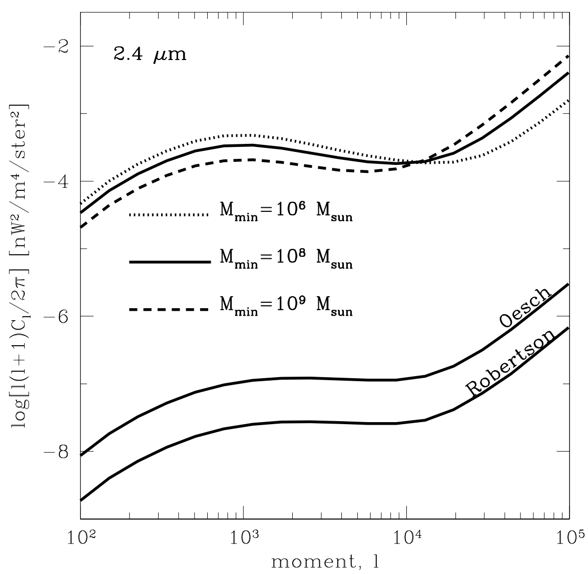

Figure 3.10: The angular NIR PS over the AKARI 2.4μm bandpass in units of $\left[\mathrm{nW}^2/\mathrm{m}^4/\mathrm{ster}^2\right]$, for a Pop III stellar population (Salpeter from $3-150\mathrm{M}_\odot$) with $f_{\mathrm{esc}}=0.1$, $f_\star=0.5$, contributing over a redshift range of $z=6-30$. Dotted, solid, and dashed curves have a threshold mass of $M_{\mathrm{min}}=10^6,\ 10^8,\ 10^9\mathrm{M}_\odot$ respectively. The bottom most pair of curves use star formation efficiencies obtained using the UV luminosity densities from [Robertson et al., 2013] and [Oesch et al., 2012]. All curves use $t_{\mathrm{SF}}=f_{\mathrm{coll}}/\dot{f}_{\mathrm{coll}}$.

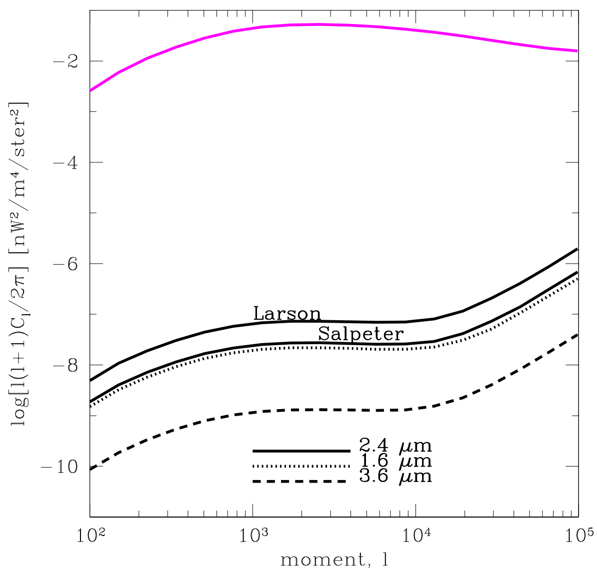

Figure 3.11: The angular NIR PS in units of $\left[\mathrm{nW}^2/\mathrm{m}^4/\mathrm{ster}^2\right]$, for a Pop III stellar population (Salpeter from $3-150\mathrm{M}_\odot$) with $M_{\min}=10^8\mathrm{M}_\odot$, $f_{esc}=0.1$, $t_{\mathrm{SF}}=f_{\mathrm{coll}}/\dot{f}_{\mathrm{coll}}$, contributing over a redshift range of $z=6-30$. The star formation efficiencies are obtained using the UV luminosity densities from [Robertson et al., 2013]. Solid, dotted, and dashed curves are calculated over several bandpasses: 2.4μm (AKARI), 1.6μm (NICMOS), and 3.6μm (IRAC), respectively. The topmost magenta solid curve represents a Pop III stellar population (Larson from $1-1000\mathrm{M}_\odot$ with $m_c=100\mathrm{M}_\odot$) with $M_{\min}=10^5\mathrm{M}_\odot$, $f_{\mathrm{esc}}=0.1$, $t_{\mathrm{SF}}=f_{\mathrm{coll}}/\dot{f}_{\mathrm{coll}}$, $f_\star=0.5$, contributing over a redshift range of $z=8-30$.

The amplitude of the NIR angular PS is sensitive to the square of the luminosity per halo mass, which is in turn proportional to the SF efficiency, ionizing efficiency, and the inverse of the SF timescale, all three of which are highly unconstrained parameters for Pop III stars at these very early times.
[Fernandez et al., 2012] use a constant SF timescale of 20 Myrs in all of their models, which implies that the galaxies are cycling through their baryons and forming new stars incredibly fast. Switching to a constant and very short $t_{\rm SF} = 20$ Myrs boosts the amplitude of fluctuations by around two orders of magnitude. Our treatment of $t_{\rm SF}$ results in much smaller fluctuations.

The curves for all models are relatively flat with a gentle turnover at $l \sim 10^3$, which is due to our linear treatment of the 'two-halo' term of the 3D PS, which we assume is proportional to the linear matter PS, $P^{\rm lin}(k)$ (the linear PS turns over at $l \sim 10^3$). [Fernandez et al., 2010] argue that the more emphatic turnover at this scale reported by [Cooray et al., 2004] is merely a symptom of neglecting non-linear effects on the halo bias, which underestimates the angular PS on small scales. [Cooray et al., 2012b] however do not report such a turnover.

The shape of our angular PS is rather impervious to changes in model parameters, in particular the threshold mass, $M_{\rm min}$. As in [Cooray et al., 2012b], we find that a lower $M_{\rm min}$ leads to a higher clustering amplitude but lower shot noise amplitude; consequently the shape of the total fluctuations is relatively flat for all choices of $M_{\rm min}$ over the angular scales that we expect to find Pop III stellar contributions (over a few tens of arcminute scales, or $l \sim 10^2 - 10^3$). This is in contrast to [Fernandez et al., 2012], who found larger fluctuations for the cases with higher $M_{\rm min}$. This is due to their varying ionizing efficiencies used throughout their models; each modeled stellar population was constrained to be exclusively responsible for reionization. Consequently, smaller populations with higher $M_{\rm min}$ required larger ionizing efficiencies to reionize on their own, resulting in higher fluctuations. In our models we employ one constant ionizing efficiency for each stellar population at hand regardless of $M_{\rm min}$– in other words, the halos do not know how many other halos there are forming stars. We do not assume that early stars were solely burdened with the task of reionization; this assumption will lead to an overestimate of their contribution to the total background.

[Fernandez et al., 2012] also found that the shape of the NIR angular PS changes for varying choices of $M_{\rm min}$, with the PS being steeper for cases with the highest $M_{\rm min}$ and a partial suppression of small halos (no star formation in halos with $M < 10^9{\rm M}_\odot$ that live in ionized regions). Though our linear approximation may underestimate the 'one-halo' contribution at the smaller scales (high l), our 'two-halo' predictions at the larger scales (small l) should remain unaffected by non-linear effects. We do not find that the shape of the 'two-halo' contribution on these large scales can be necessarily distinguished between models using varying $M_{\rm min}$, excepting for a small change in amplitude by a factor of a few.

In Figure 3.11 we present the NIR angular PS in units of $\left[{\rm nW}^2/{\rm m}^4/{\rm ster}^2\right]$, for a Pop III stellar population (Salpeter from $3-150{\rm M}_\odot$) with $M_{\rm min} = 10^8{\rm M}_\odot$, $f_{\rm esc} = 0.1$, $t_{\rm SF} = f_{\rm coll}/\dot{f}_{\rm coll}$, contributing over a redshift range of $z = 6-30$. The star formation efficiencies are obtained using the UV luminosity densities from [Robertson et al., 2013]. Solid, dotted, and dashed curves are calculated over several bandpasses used in observations: 2.4μm (AKARI; [Matsumoto et al., 2011]), 1.6μm (NICMOS; [Thompson et al., 2007b]), and 3.6μm (IRAC; [Kashlinsky et al., 2012, Cooray et al., 2007]), respectively. These curves live several orders of magnitude below the observations (for example the AKARI measurements live at $l(l+1)C_l/2\pi \sim 0.1-1.0$ ${\rm nW}^2/{\rm m}^4/{\rm ster}^2$). The middling solid curve labeled 'Larson' represents the same model parameters as the bottom most solid curve labeled 'Salpeter' excepting for the stellar IMF which is characterized by a Larson form with $m_c = 100{\rm M}_\odot$ that spans over stellar masses of $1-1000{\rm M}_\odot$. Adjusting the IMF to this more top-heavy version only boosts the angular PS by a factor of ~ 3. The topmost magenta solid curve represents a Pop III stellar population (Larson from $1-1000\mathrm{M}_\odot$ with $m_c = 100\mathrm{M}_\odot$) with $M_{\min} = 10^5\mathrm{M}_\odot$, $f_{\rm esc} = 0.1$, $t_{\rm SF} = f_{\rm coll}/\dot{f}_{\rm coll}$, $f_\star = 0.5$, contributing over a redshift range of $z = 8-30$. While these more extreme parameters are sufficient to boost the amplitude of our model mean NIRB intensity to become comparable to the observed excess intensity, they are not enough to match our model angular PS to the observed levels; the magenta curve still lives up to two orders of magnitude below the AKARI observations.

There are strong arguments that the measured excess fluctuations in the NIRB could indeed be indirect signatures of Pop III stars; both [Helgason et al., 2012] and [Kashlinsky et al., 2012] claim that the measured signal cannot be accounted for by the observed, or 'counted,' ordinary galaxies or by faint, uncounted galaxies at low redshift. In order to reproduce the measured source subtracted NIRB fluctuations, a highly clustered luminous population with low shot noise is required. Additionally, [Matsumoto et al., 2011] point out that the colors of the fluctuations require them being produced by highly redshifted, very luminous sources. Figure 3.11 demonstrates that our predictions are well below the observed excess fluctuations to date for all models; currently, observations do not constrain any of our parameters. Our results indicate that though the contribution of Pop III stars to NIRB fluctuations is non-zero and finite, it could be even smaller than initially hoped.

3.5 Summary & Conclusions

The NIRB has for some time been considered a potential window to the mysterious era of Pop III stars, widely regarded as the likely harbingers of cosmic hydrogen reionization. Pop III stars are thought to have formed around $z \sim 20-30$ [Couchman and Rees, 1986a] and new Pop III star production could have fizzled out already before reionization was complete. The Lyman-α recombination lines emitted at $z = 7-15$ are redshifted to $\sim 1-2\mu m$, making the NIR background amenable for hunting Pop III stellar signatures. The hunt has indeed been well underway, as several groups have reported excess levels of the mean NIRB intensity [Wright, 2001, Cambrésy et al., 2001, Matsumoto et al., 2005] and fluctuations [Kashlinsky, 2005, Cooray et al., 2007, Kashlinsky et al., 2007] [Thompson et al., 2007b, Matsumoto et al., 2011, Kashlinsky et al., 2012] [Cooray et al., 2012a] that are above and beyond what can be accounted for with not only known, 'counted' galaxies but, as some would agree [Helgason et al., 2012, Matsumoto et al., 2011, Kashlinsky et al., 2012], by very faint 'uncounted' galaxies at low redshift.

In this paper, we have modeled the contribution from high redshift galaxies to the mean intensity and fluctuations of the NIRB using a variation of the halo model. We have constrained the star formation efficiency by using the cold accretion model described in [Muñoz, 2012] to estimate the LF and luminosity density at high redshift, then matching this to the results of [Robertson et al., 2013] and [Oesch et al., 2012].

We find that in order to approach a match of Pop III contributions to observations of the mean NIRB intensity excess, multiple stringent conditions must be met: we would need ionizing efficiencies that are at least an order of magnitude higher than the values proposed by [Schaerer, 2002] and an extremely top-heavy stellar IMF that extends out to at least $\sim 1000\mathrm{M}_{\odot}$. We would require Pop III SF to persist in minihalos until $z \sim 8$, an unlikely scenario as minihalos are thought to have been sterilized well before this time due to high levels of the cosmic LW BG wiping out their supplies of H_2, which they need to cool gas and form stars [Holzbauer and Furlanetto, 2012]. Additionally, an extreme top-heavy stellar IMF could result in too many black holes, which may overproduce the X-ray background.

The angular PS of the NIRB we find is relatively flat over the scales of interest; Pop III stars are suggested to dominate the anisotropy of the CIRB in the NIR for $1 \leq \lambda \leq 4\mu$m over tens of arcminute scales while unresolved galaxies at $z \geq 3$ are expected to dominate at $\lambda \geq 4\mu$m for all angular scales [Cooray et al., 2004]. Existing measurements clearly show an excess in clustering at 30 arcsecond to a few tens of arcminute angular scales, beyond what can be accounted for by normal galaxies. We find that in contrast to previous studies, we cannot distinguish between different models with varying threshold mass, $M_{\rm min}$, by studying the shape of the fluctuations. A smaller $M_{\rm min}$ results in lower shot noise levels but a higher clustering amplitude, resulting in a flattened overall shape for all choices of threshold mass. Additionally, by using a luminosity per halo mass that varies with $M_{\rm min}$ and SF efficiencies matched to high redshift observations, we determine a fluctuation amplitude that is several orders of magnitude below current measurements.

The Pop III stellar contribution to the mean NIRB intensity and fluctuations is certainly present and finite but could in fact be even smaller than previously thought, implying that indeed, a previously unknown or unconsidered luminous source population at high redshift must be the culprit. The first suggestion as to the make up of this potential 'undiscovered' source population has come from [Cappelluti et al., 2013] and [Yue et al., 2013]; they infer, from detected cross correlations in the NIR and X-ray backgrounds, that the unresolved population must include a substantial fraction of black hole emitters. [Cooray et al., 2012a] suggest that instead of an undetected population being responsible for the NIRB excess, the excess can be covered by a so far uncounted contribution arising from diffuse intrahalo stellar light in galaxies at redshifts $z \sim 1 - 4$. Another possibility is that existing measurements are simply too high due to an incomplete removal of zodiacal light– in fact, recent observations of low redshift blazars [Aharonian et al., 2006, Mazin and Raue, 2007, Raue et al., 2009, Orr et al., 2011] and other high redshift gamma-ray sources [Gilmore, 2012] could indicate that the NIRB intensity may actually be lower than what is currently measured.

Hopefully future measurements with the Cosmic Infrared Background Experiment (CIBER, [Zemcov et al., 2011]), which will offer a wide field of view to measure fluctuations at even larger angular scales, will shed new light on this mystery and provide additional and more accurate measurements of the NIRB excess.

CHAPTER 4

Detecting the First Stars by Mapping Lyman-α and He II $\lambda 1640$ Fluctuations

4.1 Introduction

The first stars to light up our universe are as yet unseen, but there have been many attempts to indirectly surmise their properties. The nine-year *Wilkinson Microwave Anisotropy Probe* (WMAP-9) results indicate that the cosmic reionization of neutral hydrogen occurred at a redshift of $z_{reion} \sim 10$ if the process was instantaneous and homogeneous in a spatially flat universe [Hinshaw et al., 2012]. Detections of the Gunn-Peterson (GP) trough [Gunn and Peterson, 1965] in $z \sim 6$ quasars [Becker et al., 2001, Fan et al., 2002, Fan et al., 2006] suggest that the reionization process was in its final stages around that time. In addition, recent observations have indicated a peak in the quasar luminosity function (QLF) at $z \sim 3$ and a drop in quasar space density at earlier times [Pei, 1995, Fan et al., 2006]. If quasars were not dominantly responsible for reionization, then it is likely that the first stars (Population/Pop III stars) played an important part in that process.

Pop III stars are thought to have first formed out of metal-free H/He gas contained in minihalos at redshifts $z \sim 20 - 30$ [Couchman and Rees, 1986a]. These stars are too far away to resolve directly, so astronomers are now engaged in inventing new, creative methods with which to indirectly detect these sources. By probing the highest redshifts that current and near future technology can access, we may be able to catch a glimpse of the final phase of Pop III star formation (SF) at $z \sim 9-10$. The near-infrared background (NIRB) has for some time been investigated theoretically [Fernandez et al., 2010, Silva et al., 2013] and observationally [Kashlinsky, 2005] as a potential window to Pop III stars, as the Lyman-α recombination lines emitted at $z = 7-15$ are redshifted to $\sim 1-2\mu$m. However, current measurements of the NIRB are still uncertain due to zodiacal light contamination and current models of Pop III stars are limited due to our lack of constraints on the stellar initial mass function (IMF).

As an alternative, we could select Pop III sources based on their broadband colors in a way similar to the Lyman-break technique [Steidel et al., 1999], which exploits the fact that the observed spectrum of a galaxy is wiped out at wavelengths short ward of the Lyman limit due to absorption by the intergalactic medium (IGM). Pop III stars are inherently bluer than metal enriched Pop II stars, but the excess blueness is neutralized by the reprocessing of Lyman-continuum photons into continuous nebular emission [Tumlinson et al., 2003], resulting in a degeneracy of broadband color between Pop III/II stars. Perhaps more promising is a narrowband search for emission line signatures unique to the first stars.

What are these Pop III stellar emission line signatures and what makes them so special? Pop III stars begin to form in the usual way, with a nascent protostellar cloud accreting gas. However, the processes that regulate protostellar accretion rates in metal enriched SF (such as cooling through metal lines) are absent in primordial gas, leading to very strong accretion rates and less fragmentation in the clouds [Ferrara, 2001]. Consequently, Pop III stars may have been very massive, with typical masses $M_\star \sim 100\mathrm{M}_\odot$ [Yoshida et al., 2006]. They are also more compact; Pop III stars are roughly two times hotter and five times smaller than Pop II stars of the same mass [Tumlinson et al., 2003]. This results in a much harder ionizing spectrum [Tumlinson et al., 2001, Schaerer, 2002]. In fact, the increase in ionizing flux from solar to zero metallicity can be as much as a factor of 10 [Schaerer, 2003]. A large portion of the ionizing photons have energies with

$h\nu > 54.4$ eV that carve out substantial patches of doubly ionized helium, He III. These photoionized regions then begin to shine brightly in He II recombination emission. Due to the lack of heavy elements in these regions, Pop III stars must rely on hydrogen and helium for cooling, enhancing both the Lyman-α and He II emission lines. In this regard, Pop III stars can be characterized as 'dual emitters,' i.e. producers of both Lyman-α and He II emission signatures.

Pop III stars are expected to produce Lyman-α emission lines with unusually high equivalent widths (EWs; [Tumlinson et al., 2003]), which can range between $500 - 1000$ Å. Metal-enriched stars at solar metallicity, in contrast, have much smaller EWs that span from $200 - 300$ Å [Schaerer, 2003, Schaerer, 2008]. Since the Lyman-α EW is so sensitive to metallicity, it can potentially serve as a powerful indicator for Pop III sources. However, this line is strongly attenuated by dust absorption and resonant scattering through neutral hydrogen clouds [Schaerer, 2003], altering the intrinsic value of its EW [Schaerer, 2007]. In addition, Lyman-α emission is not unique to Pop III stars, so by itself it is not a reliable indicator of primordial stars. However, it becomes a powerful tool when coupled with He II emission.

He II recombination emission appears to be almost unique to extremely metal poor stars with $\log(Z/\mathrm{Z}_{\odot}) < -5.3$ [Schaerer, 2003]. The He II recombination lines at $\lambda 1640$ Å ($n = 3 \rightarrow 2$), $\lambda 3203$ Å ($n = 5 \rightarrow 3$), and $\lambda 4686$ Å ($n = 4 \rightarrow 3$) are exceptional to utilize for Pop III detection since those transitions do not suffer from resonant scattering effects and experience minimal absorption from intervening dust [Scannapieco et al., 2003]. Among these lines, the He II $\lambda 1640$ line is the strongest [Tumlinson et al., 2001]: its rest-frame equivalent width (EW) can reach as much as a few tens of Å if a galaxy contains a large number of Pop III stars [Schaerer, 2003]. Theoretically, the detection of He II $\lambda 1640$ sourced from Pop III stars may be feasible with current observational facilities [Tumlinson et al., 2003]. Together, Lyman-α and He II emission can offer a much more robust signature of Pop III stars.

Several groups have already embarked on a search for the elusive Pop III stars by seeking high redshift Lyman-α emitters (LAEs) with large EWs. The LALA (Large Area Lyman-α) Survey [Malhotra and Rhoads, 2002] observed high Lyman-α EWs at $z \sim 4.5$; over 60% of detections were reported to have EWs above the maximum attainable by Pop II clusters. However, other groups delving into the Subaru Deep Field [Hu et al., 2004, Shimasaku et al., 2006] find that this number is probably much lower ($\sim 10-40\%$). It is possible that some of these detections have probed metal-free stars, but since the observed Lyman-α EWs are so strongly attenuated by the IGM, high uncertainty remains in the interpretation of this data [Dijkstra and Wyithe, 2007]. Additionally, updated calculations by [Raiter et al., 2010] show that expectations for Pop III Lyman-α EWs could be even higher than previously thought.

Once a source has been identified as a LAE, further investigation is needed to uncover any possible He II emission. There have been several attempts to do this. [Dawson et al., 2004] investigated the stacked spectra of 17 LAEs at $z \sim 4.5$ and found no He II λ1640 signal, implying that Pop III stars should form at $z > 4.5$. [Ouchi et al., 2008] performed a similar stacking analysis on an even larger sample of LAEs at $z \sim 3.1-5.7$ and also failed to detect He II. Performing ultra-deep NIR spectroscopy on an individual Subaru Deep Field LAE at $z = 6.33$, [Nagao et al., 2005] also came up empty handed. [Nagao et al., 2008] followed up this study, also using Subaru, with a combined narrow and intermediate band search for high redshift dual emitters at $z \sim 4-4.5$. Though no convincing candidates were found, they obtained the first upper limit value for the Pop III SFR ($< 5 \times 10^{-6}$ M$_\odot$ yr^{-1} Mpc^{-3}) based on the observed flux limits of the survey.

Most recently, [Cassata et al., 2013] discovered 39 He II λ1640 emitters at $2 < z < 4.6$ in the VIMOS (Visible Multi Object Spectrograph)-VLT (Very Large

Telescope of the European Southern Observatory) Deep Survey (VVDS) Deep and Ultra-Deep data. Of these sources, 11 are so far consistent with (or at least cannot exclude) a very low redshift tail scenario of Pop III SF. Their estimates of Pop III SF are interestingly compatible with predictions by [Tornatore et al., 2007], who used numerical simulations to suggest that due to inefficient cosmic metal mixing, Pop III SF can proceed all the way down to $z \sim 2.5$ in a wave of preserved primordial gas propagating outward from collapsed structures in an 'inside-out' behavior. Ultimately it is as yet unknown if such a special phase of pristine SF can continue into such late epochs, however the presence of He II emission in itself certainly does not confirm a Pop III origin.

Though the signature Lyman-α + He II dual emission is an excellent signpost for metal-free stars, it is not exclusive to them. Other possibilities for the origin of this dual emission are AGN, supernova driven winds, or Wolf-Rayet (W-R) stars. In fact, [Shapley et al., 2003] were the first to detect broad He II emission in a composite spectrum of over ~ 1000 $z \sim 3$ galaxies; these detections were later confirmed as originating from W-R stars [Brinchmann et al., 2008, Elridge and Stanway, 2012]. W-R stars are usually straightforward to distinguish from Pop III stars, as they are associated with strong winds that produce very broad emission lines (usually a few ~ 1000 km sec^{-1}; [Schaerer, 2003]). Additionally, W-R stars, AGN, and supernova driven winds typically demonstrate other emission lines in their spectra, like C III and C IV.

As we have discussed above, detections of Lyman-α + He II dual emission in individual galaxies is rare and open to interpretation. Detection at very high redshift is currently challenged and constraints on stellar observations from photometric observations of galaxies at $z > 7$ are very weak [Dunlop et al., 2013, Robertson et al., 2013]. A more promising trail of attack may be to map fluctuations in the total intensity, which will allow us to indirectly assess sources that are below typical luminosity thresholds of deep surveys. Some studies have discussed doing this for Lyman-α emission [Silva et al., 2013], which lies in the NIR for sources at high redshift. We propose cross-correlating fluctuations in intensity of Lyman-α and He II emission as a more robust method for detecting primordial stellar populations. Cross-correlating these two lines, one of which is extremely sensitive to stellar metallicity, is very powerful in that it allows us to better isolate the redshift of source emission. In section 4.2 we will describe how we model the mean intensity and volume emissivity for Pop II and Pop III Lyman-α and He II $\lambda 1640$ emission. In sections 4.3 and 4.4 we present results for the Lyman-α and He II $\lambda 1640$ mean intensities. In section 4.5 we calculate the cross-PS for the Lyman-α and He II $\lambda 1640$ lines originating from primordial stars at high redshift. In section 4.6 we present a summary and conclusions.

4.2 Modeling the Lyman-α and He II $\lambda 1640$ Å Backgrounds

4.2.1 The Mean Intensity and Volume Emissivity

We can write the observed mean intensity at an observed frequency, ν, and redshift, z, (following pg. 115 from [Loeb and Furlanetto, 2013]) as:

$$\bar{I}_\nu(z) = \frac{c}{4\pi} \int_z^\infty dz' \frac{\bar{\epsilon}_{\nu'}(z')}{H(z')(1+z')}, \tag{4.1}$$

where $H(z)$ is the cosmic expansion rate and $\bar{\epsilon}_{\nu'}(z')$ is the comoving volume emissivity at emitting frequency, $\nu' = \nu(1+z')/(1+z)$, and redshift, z'. We assume that the time averaged star formation rate (SFR) density is proportional to the time derivative of the collapse fraction, $f_{\rm coll}$ (fraction of mass in the universe contained in galaxies, or collapsed in a halo). In this work, we use the Sheth-Tormen mass function [Sheth and Tormen, 1999] to calculate $f_{\rm coll}$. With this, we can write the star formation rate density as $\dot{\rho}_\star(z) = f_\star \times \dot{M}_{\rm acc}$, or:

$$\dot{\rho}_\star(z) = \bar{\rho}_{b0} f_\star \left[\frac{d}{dt} f_{\rm coll}(z) \right], \tag{4.2}$$

where $f_\star$ is the star formation efficiency (fraction of baryons that actually go into forming stars over the typical star forming (SF) timescale, which we will assume here to be the same for all halos), and the mean baryon density today is $\bar{\rho}_{b0} = 2.775 \times 10^{11}(\Omega_b h^2)\mathrm{M}_\odot\mathrm{Mpc}^{-3}$. We define the SF timescale as $t_{\mathrm{SF}} \equiv [d \ln \rho_\star(z)/dt]^{-1}$. From eqn 4.2, it follows that $t_{\mathrm{SF}} \equiv [d \ln f_{\mathrm{coll}}(z)/dt]^{-1}$, which is around 55 Myrs at $z = 10$. $\dot{M}_{\mathrm{acc}}$ is the rate at which the halo accretes baryonic gas.

In order to determine the total volume emissivity, $\bar{\epsilon}_\nu$, it is necessary to adopt a model describing the stellar population residing in each halo (described in detail in §4.2.2).

In order to calculate the average volume emissivity of this region, $\bar{\epsilon}(z)$, we integrate the NIR luminosity per halo mass over the halo mass function:

$$\bar{\epsilon}_i(z) = \int_{M_{\min}}^{\infty} dm n(m) m \frac{L_{h,i}(z)}{M_h}, \tag{4.3}$$

where $\bar{\epsilon}_i(z)$ is the average volume emissivity arising from component i and $L_{h,i}(z)/M_h$ is the luminosity per halo mass of component i.

4.2.2 Stellar Properties and Populations

Past literature exploring models of the NIRB have used various analytic prescriptions to describe the earliest stellar populations and their properties. However, very little is known as to the exact properties of Pop III stellar families. We adopt two different IMFs, $f(m)$, to represent the total stellar mass spectrum. The first is a Salpeter [Salpeter, 1955] IMF with a mass range of $3 - 150\mathrm{M}_\odot$:

$$f(m) \propto m^{-2.35}, \tag{4.4}$$

while the second is a Larson [Larson, 1998] IMF with mass range of $5 - 150\mathrm{M}_\odot$:

$$f(m) \propto \frac{1}{m}\left(1 + \frac{m}{m_c}\right)^{-1.35}, \tag{4.5}$$

where $m_c = 50\mathrm{M}_\odot$. The average stellar mass of the population is calculated as follows:

$$m_\star = \int dm\ mf(m), \tag{4.6}$$

where $m_\star = 8.7$ and $27.4\mathrm{M}_\odot$ for the Salpeter and Larson IMFs respectively. As we are only interested in stars that produce a non-negligible supply of ionizing photons, the values we use here for the SF efficiency, $f_\star$, only account for this high stellar mass component. The actual values of $f_\star$, which also incorporate non-contributing low-mass stars, are most likely larger. Additionally, in this work we exclusively employ the top-heavy Larson IMF to describe Pop III stellar populations and the more tempered Salpeter version for metal-poor Pop II stars. However, recent simulations [Clark et al., 2008, Stacy et al., 2010b, Clark et al., 2011a, Clark et al., 2011b] challenge the long accepted scenario of isolated, massive Pop III SF and suggest a model rife with significant fragmentation in the primordial protostellar disks. These fragments could lead to additional protostars with masses ~ 0.1 to $10\mathrm{M}_\odot$ [Greif et al., 2011]. In this case, a Salpeter IMF could be more appropriate and a Larson IMF would result in an upper limit for the total stellar emission.

Next we consider properties of individual stars: the main sequence lifetime, $\tau(m)$, the hydrogen photoionization rate, $\bar{Q}_{\mathrm{H}}(m)$ (averaged over the lifetime), and the He^+ photoionization rate, $\bar{Q}_{\mathrm{He}^+}(m)$ (also averaged over the lifetime). We present these properties for Pop III metal-free ($Z = 0$) stars and Pop II metal-poor ($Z = 1/50\mathrm{Z}_\odot$) stars below in §4.2.2.1 and §4.2.2.2.

4.2.2.1 Metal-Free Stellar Properties

We use the following fitting formulae from [Schaerer, 2002] to model properties of individual metal-free ($Z = 0$) Pop III stars. The main sequence lifetime, $\tau(m)$, hydrogen photoionization rate, $\bar{Q}_{\mathrm{H}}(m)$ (number of hydrogen ionizing photons produced per second, averaged over the lifetime), and He^+ photoionization rate, $\bar{Q}_{He^+}(m)$, apply to stars with $m = 5 - 500 M_\odot$:

$$\log_{10}\left(\frac{\tau}{\rm yr}\right) = 9.785 - 3.759x + 1.413x^2 - 0.186x^3, \tag{4.7}$$

$$\log_{10}\left(\frac{\bar{Q}_{\rm H}}{\rm sec^{-1}}\right) = \begin{cases} 39.29 + 8.55x, & 5 - 9 M_\odot \\ 43.61 + 4.9x - 0.83x^2, & 9 - 500 M_\odot \end{cases} \tag{4.8}$$

$$\log_{10}\left(\frac{\bar{Q}_{\rm He^+}}{\rm sec^{-1}}\right) = 26.71 + 18.14x - 3.58x^2. \tag{4.9}$$

where $x \equiv \log_{10}(m/M_\odot)$. The stars below the mass cutoff produce a negligible amount of hydrogen and He^+ ionizing photons (less than 1% of the total for both Pop III and Pop II stars).

4.2.2.2 Metal-Poor Stellar Properties

We use the following fitting formulae from [Schaerer, 2002] for individual metal-poor ($Z = 1/50 Z_\odot$) Pop II stars. The main sequence lifetime, $\tau(m)$, and hydrogen photoionization rate, $\bar{Q}_{\rm H}(m)$ apply to stars with $m = 7 - 150 M_\odot$:

$$\log_{10}\left(\frac{\tau}{\rm yr}\right) = 9.59 - 2.79x + 0.63x^2, \tag{4.10}$$

$$\log_{10}\left(\frac{\bar{Q}_{\rm H}}{\rm sec^{-1}}\right) = 27.8 + 30.68x - 14.8x^2 + 2.5x^3. \tag{4.11}$$

The He^+ photoionization rate, $Q_{He^+}(m)$, is given by [Schaerer, 2002] as:

$$\log_{10}\left(\frac{\bar{Q}_{\rm He^+}}{\rm sec^{-1}}\right) = 34.65 + 8.99x - 1.40x^2. \tag{4.12}$$

This expression is valid for metal-poor stars with stellar masses between $20 - 150 M_\odot$ (stars with $m < 20 M_\odot$ have a negligible He II ionizing flux).

4.2.3 The Stellar Ionizing Efficiency

We can determine the total emission from both the Lyman-α and He II $\lambda1640$ components by first calculating the stellar ionizing efficiency, $\bar{\epsilon}_{b,i}$, i.e., the average number of ionizing photons emitted per stellar baryon. The Lyman-α and He II $\lambda1640$ components are directly proportional to the hydrogen ionizing efficiency and He$^+$ ionizing efficiency, which we will parameterize through $\bar{\epsilon}_{b,\mathrm{H}}$ and $\bar{\epsilon}_{b,\mathrm{HeII}}$, respectively. We obtain $\bar{\epsilon}_{b,i}$ by integrating the appropriate photoionization rate and stellar lifetime over the stellar IMF:

$$\bar{\epsilon}_{b,i} = \frac{\int dm\ f(m) Q_i(m) \tau(m)}{\int dm\ f(m)(m/m_p)}, \tag{4.13}$$

where m_p is the proton mass. Eqn 4.13 gives us the stellar ionizing efficiency averaged over the entire stellar population. Average hydrogen ionizing efficiencies for Pop III stars with a Salpeter and Larson IMF are approximately $\bar{\epsilon}_b \sim 30,000$ and $60,000$ photons per baryon, respectively.

Average He II ionizing efficiencies for Pop III stars and Pop II stars with a Salpeter IMF are approximately $\bar{\epsilon}_{b,\mathrm{HeII}} \sim 424$ and 14 photons per baryon, respectively. For a Pop III stellar population characterized by a Larson IMF, $\bar{\epsilon}_{b,\mathrm{HeII}} \sim 1400$ photons per baryon.

4.2.4 The Lyman-α Component

In order to calculate the average volume emissivity, we first start with the luminosity per halo mass. The Lyman-α luminosity per halo mass can be written as:

$$\left.\frac{L_h(z)}{M_h}\right|_{\mathrm{Ly}\alpha} = f_\star \frac{\Omega_b}{\Omega_m}(1 - f_{\mathrm{esc},\alpha}) \frac{f_{\mathrm{Ly}\alpha} \bar{\epsilon}_{b,\mathrm{H}} E_{\mathrm{Ly}\alpha}}{t_{\mathrm{SF}}(z) m_p}, \tag{4.14}$$

where $f_\star$ is the SF efficiency (fraction of baryons that go into forming stars), $f_{\mathrm{esc},\alpha}$ is the escape fraction of the Lyman-α photons (fraction of photons that escape out of the stellar nebular and into the IGM), $f_{\mathrm{Ly}\alpha} \sim 2/3$ is the approximate fraction of recombinations that result in a Lyman-α photon, $E_{\mathrm{Ly}\alpha} = 13.6$ eV is the energy of one Lyman-α photon, m_p is the proton mass, and t_{SF} is the SF timescale. Finally, $\bar{\epsilon}_{b,\mathrm{H}}$ is the stellar ionizing efficiency, i.e., the average number of hydrogen ionizing photons emitted per stellar baryon.

4.2.5 The He II $\lambda 1640$ Å Component

The average volume emissivity for the He II $\lambda 1640$ component can be written in a very similar way. The He II luminosity per halo mass is:

$$\left.\frac{L_h(z)}{M_h}\right|_{\mathrm{HeII}} = f_\star \frac{\Omega_b}{\Omega_m}(1 - f_{\mathrm{esc,HeII}}) \frac{f_{\mathrm{HeII}} \bar{\epsilon}_{b,\mathrm{HeII}} E_{\mathrm{HeII}}}{t_{\mathrm{SF}}(z) m_p}, \tag{4.15}$$

.

Once the stars carve out a patch of doubly ionized helium, He III, some of these He III ions recombine and emit He II photons. A fraction, $f_{\mathrm{HeII}} \sim 0.47$, of these recombinations result in He II $\lambda 1640$ photon emission [Schaerer, 2002].

4.3 Results: The Lyman-α Background

4.3.1 The Lyman-α Luminosity Function

We follow [Muñoz and Loeb, 2011] in developing an expression for the Lyman-α luminosity function (LF):

$$\Phi(L, z) = \int_{M_{\mathrm{min}}}^{\infty} dm \frac{dn(z)}{dm} \frac{dP(L|m)}{dL}, \tag{4.16}$$

where $dn(z)/dm$ is the halo mass function [Sheth and Tormen, 1999], $L(M_{\mathrm{min}}) = L_{\mathrm{lim}}$. Rather than assume unrealistically that there is only a single halo mass that corresponds to a particular luminosity, we can incorporate a luminosity distribution into our model, such that $dP(L|m)/dL$ is the probability that a halo of mass, m, has luminosity, L. We can approximate the distribution of luminosities

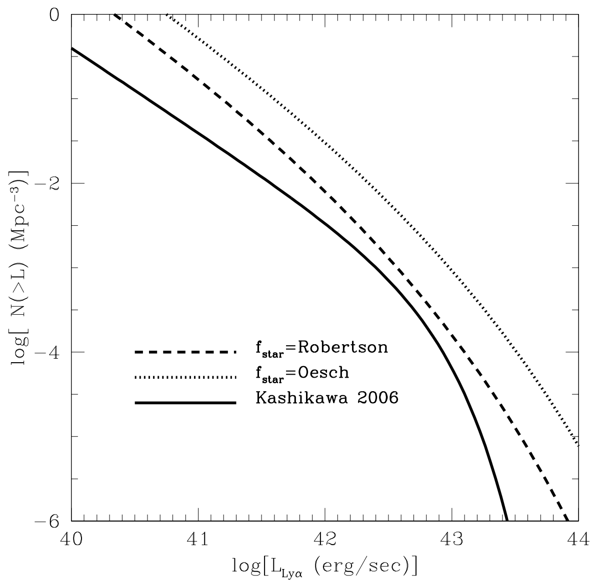

Figure 4.1: The Lyman-α LF [Mpc^{-3}] at $z = 6.5$. The solid curve represents best-fit Schechter parameters from [Kashikawa et al., 2006], who measured the LF of LAEs in the Subaru Deep Field. The remaining two curves represent our modeled Lyman-α LFs using equation 4.16. Both curves assume a halo population with $M_{\rm min} = 10^8 {\rm M}_\odot$, $f_{\rm esc} = 0.1$, and Pop III stellar populations characterized by a Salpeter IMF with stellar mass range $3 - 150{\rm M}_\odot$. The dashed curve uses the SF efficiency, $f_\star(z)$, generated using results from [Robertson et al., 2013], while the dotted curve uses $f_\star(z)$ generated using the observations of [Oesch et al., 2012].

produced by halos of a given mass as a log-normal distribution:

$$\frac{dP}{d\log L} = \frac{1}{\sqrt{2\pi\sigma_L^2}} \exp\left\{ -\frac{[\log(L/L_c)]^2}{2\sigma_L^2} \right\}, \tag{4.17}$$

with a standard deviation $\sigma_L \sim 0.25$, and where $L_c = (M_h/10^{10}\ {\rm M}_\odot)L_{10}$, and L_{10} is the mean Lyman-α luminosity of a $10^{10}{\rm M}_\odot$ halo which is obtained using equation 4.15.

Figure 4.1 shows our results for the Lyman-α LF at $z = 6.5$. The topmost two curves represent our modeled Lyman-α LFs using equation 4.16. Both curves assume a halo population with $M_{\rm min} = 10^8 {\rm M}_\odot$, $f_{\rm esc} = 0.1$, and Pop III stellar populations characterized by a Salpeter IMF with stellar mass range $3 - 150{\rm M}_\odot$. These two curves differ only in the parameterization of the SF efficiency, $f_\star(z)$. The dashed curve uses $f_\star(z)$ generated using results from [Robertson et al., 2013], while the dotted curve uses $f_\star(z)$ generated using the observations of [Oesch et al., 2012].

The solid curve represents best-fit Schechter parameters from [Kashikawa et al., 2006], who measured the LF of Lyman-α emitters (LAEs) in the Subaru Deep Field at $z \sim 5.7$ and 6.5. Both of our models over estimate the observed LF at $z = 6.5$. This is expected as Lyman-α photons are strongly attenuated by resonant scattering and dust absorption; more than half of these photons from high redshift LAEs are estimated to be absorbed by the IGM [Haiman, 2002].

In order to match our model LF (the dashed curve calibrated using results from [Robertson et al., 2013]) to the [Kashikawa et al., 2006] observed LF (solid line) over the range of luminosities that their observations cover (approximately $10^{42} - 10^{43}$ erg/sec) we must adjust our LF by a Lyman-α factor, $X_{\rm Ly\alpha}$, of ~ 0.54. This factor is comparable to measurements by [Stark et al., 2011], who obtained $X_{\rm Ly\alpha} \sim 0.5$ for Lyman Break Galaxies (LBGs) with UV luminosities between $-20.25 < M_{\rm UV} < -18.75$ ($L_{\rm UV} \sim 10^{43}$ erg/sec), at $z \sim 6$, and exhibiting Lyman-α emission with rest frame EWs > 25 Å. In reality, this Lyman-α factor is expected to vary with both luminosity and redshift, so our corrected model LF is only an upper limit. Additionally, if we are only interested in Pop III stars, this factor will be even smaller, since these stars are expected to produce Lyman-α emission lines with very high rest frame EWs, which can range between $500 - 1000$ Å [Schaerer, 2003, Schaerer, 2008].

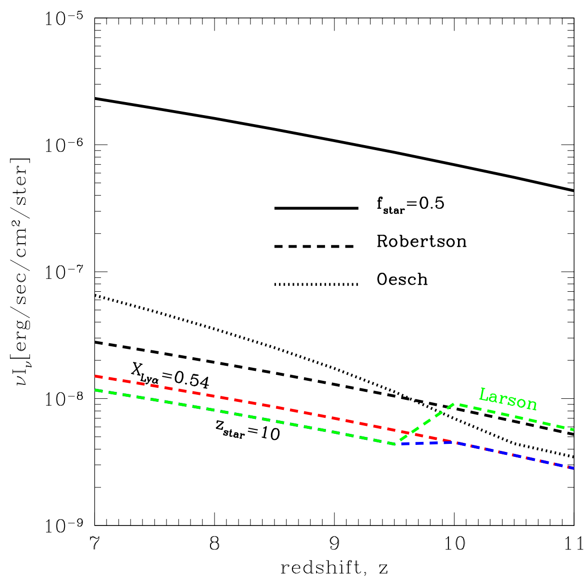

Figure 4.2: Observed Lyman-α intensity [erg/sec/cm^2/ster] from galaxies at varying redshift, z. All of the black curves are from Pop III stars with a Salpeter IMF, $f_{\rm esc} = 0.1$, $M_{\rm min} = 10^8 {\rm M}_\odot$. The solid black curve uses a constant value for the SF efficiency, $f_\star = 0.5$. The black dashed and dotted curves use values for $f_\star(z)$ generated using results from [Robertson et al., 2013] and [Oesch et al., 2012] respectively. The remaining colored dashed curves include a Lyman-α fraction, $X_{\rm Ly\alpha} = 0.54$. The blue and green dashed curves incorporate a step function model to describe the transition from Pop III to Pop II stars: Pop III stars are only found at redshifts above $z_\star = 10$ while Pop II stars are only found at redshifts below $z_\star = 10$. The green curve uses a Larson IMF to describe the Pop III stars.

4.3.2 The Lyman-α Mean Intensity

Figure 4.2 displays the observed Lyman-α intensity [erg/sec/cm^2/ster] from galaxies at varying redshift, z. All of the black curves are from Pop III stars with a Salpeter IMF, $f_{\rm esc} = 0.1$, $M_{\rm min} = 10^8 {\rm M}_\odot$. The solid black curve uses a constant value for the SF efficiency, $f_\star = 0.5$. The black dashed and dotted curves use values for $f_\star(z)$ generated using results from [Robertson et al., 2013] and [Oesch et al., 2012] respectively. The red dashed curve includes a Lyman-α fraction, $X_{{\rm Ly}\alpha} = 0.54$.

The blue and green dashed curves incorporate a simple 'step' function model to describe the transition from Pop III to Pop II stars. We define a threshold redshift, $z_\star$, such that Pop III stars exclusively live at $z > z_\star$ and Pop II stars exclusively live at $z < z_\star$, and assume that the transition takes place over $\Delta z = 0.5$. However, in reality, the transition from Pop III to Pop II stars is most likely much more extended in time [Tornatore et al., 2007, Furlanetto and Loeb, 2005]. The green curve uses a Larson IMF to describe the Pop III stars and Salpeter IMF to characterize the Pop II stars.

As opposed to Pop III Lyman-α emission, Pop II stars produce Lyman-α emission that is smaller by a factor of approximately ~ 1.3 when both Pop III and Pop II stars are characterized by Salpeter IMFs. If instead, a Larson IMF is used for the Pop III stars, that factor is ~ 2.6, making the transition more marked. However, since Pop III stellar populations are expected to gradually dissipate over time, the step seen in the blue and green dashed curves will be substantially beveled out. Consequently, distinguishing between the Pop III and Pop II stellar populations by only using the Lyman-α signal will be extremely difficult. In order to exaggerate the distinction, we can utilize the He II $\lambda 1640\,\text{Å}$ signal in conjunction with the Lyman-α component. We estimate the He II background below (see §4.4).

Our Figure 4.2 can be directly compared to Figure 4 from [Silva et al., 2013], who estimated the Lyman-α average intensity by parameterizing the SFR with halo mass and matching this to various observations and simulations. The amplitudes for our [Robertson et al., 2013] constrained models that are corrected with a Lyman-α fraction (red, blue, and green dashed curves) are within a factor of two compared to the [Silva et al., 2013] results at $z = 7$, however our curves evolve much more slowly with time compared to that in [Silva et al., 2013]. This difference stems from the fact that we chose a smaller threshold halo mass, which gives us a slower decline in $f_{\rm coll}$. We also use a SF efficiency that is increasing sharply to compensate for the decline in $f_{\rm coll}$ towards high redshift, resulting in a gentler decline in the overall intensity.

4.4 Results: The He II λ1640 Å Background

Figure 4.3 displays the observed Lyman-α (black curves) and He II λ1640 (red curves) intensities [erg/sec/cm^2/ster] from galaxies at varying redshift, z. All curves use $f_{\rm esc} = 0.1$, $M_{\rm min} = 10^8 {\rm M}_\odot$. The solid curves use a constant SF efficiency $f_\star = 0.5$ while the dashed curves use values for $f_\star(z)$ generated using results from [Robertson et al., 2013]. Solid curves are produced by Pop III stars characterized by a Salpeter IMF. Dashed curves are produced by populations of both Pop II and Pop III stars characterized by Salpeter and Larson IMFs respectively. These curves incorporate a step function model to describe the transition from Pop III to Pop II stars: Pop III stars are only found at redshifts above $z_\star = 10$ while Pop II stars are only found at redshifts below $z_\star = 10$. The black dashed curve also includes a Lyman-α fraction, $X_{\rm Ly\alpha} = 0.54$, for all redshifts.

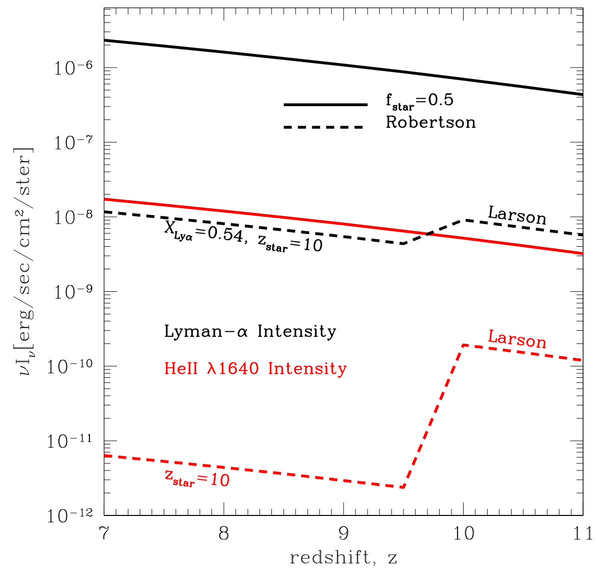

Figure 4.3: Observed Lyman-α (black curves) and He II λ1640 (red curves) intensities [erg/sec/cm^2/ster] from galaxies at varying redshift, z. All curves use $f_{\rm esc} = 0.1$, $M_{\rm min} = 10^8 {\rm M}_\odot$. The solid curves use a constant SF efficiency $f_\star = 0.5$ while the dashed curves use values for $f_\star(z)$ generated using results from [Robertson et al., 2013]. Solid curves are produced by Pop III stars characterized by a Salpeter IMF. Dashed curves are produced by populations of both Pop II and Pop III stars characterized by Salpeter and Larson IMFs respectively. These curves incorporate a step function model to describe the transition from Pop III to Pop II stars: Pop III stars are only found at redshifts above $z_\star = 10$ while Pop II stars are only found at redshifts below $z_\star = 10$. The black dashed curve also includes a Lyman-α fraction, $X_{\rm Ly\alpha} = 0.54$, for all redshifts.

4.5 The Cross Power Spectrum

4.5.1 Methodology

We can calculate the cross power spectrum between the Lyman-α and He II signals. For this basic initial calculation, we assume that the emission of both components is characterized by a delta function centered on each galaxy. For two delta function components, we can write the cross PS as:

$$
\begin{aligned}
P^{1h}_{\rm cross}(k) &= 0 & (4.18)\\
P^{2h}_{\rm cross}(k) &= \bar{\epsilon}_{{\rm Ly}\alpha}\bar{\epsilon}_{\rm HeII}\left[\int_{M_{\rm min}}^{\infty} dm n(m)\left(\frac{m}{\bar{\rho}_{\rm gal} f_{\rm coll}}\right) b(m)\right]^2 \times ... & (4.19)\\
&= ... \times P^{\rm lin}(k), & (4.20)
\end{aligned}
$$

In addition to the clustering terms, there are also fluctuations (or shot noise) that arise from the discrete nature of the halos:

$$
P_{\rm shot}(k) = \left.\frac{L_h(z)}{M_h}\right|_{{\rm Ly}\alpha} \left.\frac{L_h(z)}{M_h}\right|_{\rm HeII} \int_{M_{\rm min}}^{\infty} dm n(m) m^2 \tag{4.21}
$$

Combining all of these ingredients, we can now calculate the NIR 3D PS for any redshift.

4.5.2 Results: The 3D Cross Power Spectrum

Figure 4.4 displays the observed Lyman-α and He II λ1640 3D cross PS [$\rm nW^2/m^3$] at varying redshift and wavenumber, k [$\rm cMpc^{-1}$]. The cross PS are shown (from top to bottom) for $z = 6$ (black), 10 (blue), and 15 (red). The solid curves use a constant SF efficiency $f_\star = 0.1$ while the dashed curves use values for $f_\star(z)$ generated using results from [Robertson et al., 2013]. All models are produced by Pop III stars characterized by a Larson IMF and use $f_{\rm esc} = 0.1$, $M_{\rm min} = 10^8 \rm M_\odot$.

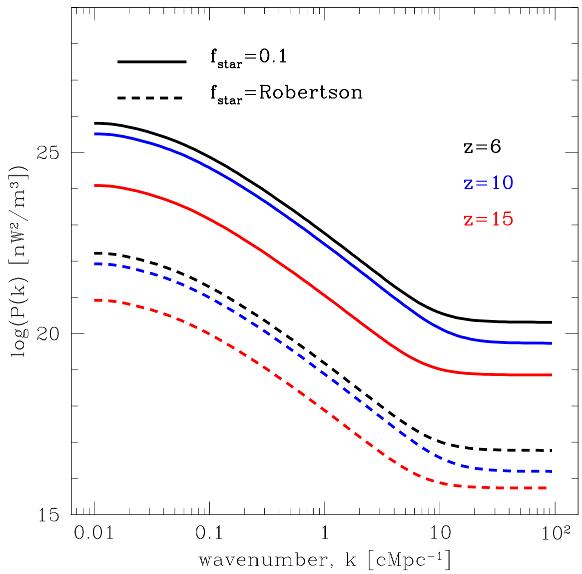

Figure 4.4: The observed Lyman-α and He II $\lambda1640$ 3D cross PS [nW^2/m^3] at varying redshift and wavenumber, k [cMpc^{-1}]. The cross PS are shown (from top to bottom) for $z = 6$ (black), 10 (blue), and 15 (red). The solid curves use a constant SF efficiency $f_\star = 0.1$ while the dashed curves use values for $f_\star(z)$ generated using results from [Robertson et al., 2013]. All models are produced by Pop III stars characterized by a Larson IMF and use $f_{\rm esc} = 0.1$, $M_{\rm min} = 10^8 \mathrm{M}_\odot$. The dashed curves also incorporate a Lyman-α fraction, $X_{\rm Ly\alpha} = 0.54$, for all redshifts.

The dashed curves also incorporate a Lyman-α fraction, $X_{\mathrm{Ly}\alpha} = 0.54$, for all redshifts.

4.6 Summary & Conclusions

In this paper we have proposed a new method for detecting primordial metal-free and very metal-poor stellar populations by cross-correlating fluctuations in intensity of Lyman-α and He II λ1640 emission sourced from high redshifts. Detecting Lyman-α + He II dual emission in individual galaxies at high redshift is difficult and rare. The few Lyman-α + He II dual emitters that have been discovered are still somewhat mysterious as the identities of the source engines powering this emission have not yet been clearly elucidated [Prescott et al., 2009, Scarlata et al., 2009, Cassata et al., 2013].

Cross-correlating the Lyman-α and He II λ1640 lines is a very robust method for detecting Pop II/Pop III stellar populations, since (1) the two lines together allow us to better isolate the redshift of source emission, and (2) the presence of the He II λ1640 emission is extremely sensitive to stellar metallicity; it appears to be unique to extremely metal poor stars with $\log(Z/\mathrm{Z}_{\odot}) < -5.3$ [Schaerer, 2003]. Since ground-based instruments are very much limited by atmospheric contamination in the NIR, we propose that a space-borne experiment could map out Lyman-α and He II anisotropies over a broad range of redshifts with narrow-band observations surveyed over a reasonable patch of sky. [Oh et al., 2001] suggest that He II recombination lines could be detectable with the upcoming *James Webb Space Telescope* (JWST) even at redshifts beyond $z \sim 10$.

This method is a strong indicator of Pop III, but there can also be other explanations for a detected Lyman-α + He II correlation, so further modeling will be required to confirm metal-free stars as the source. Another possibility for the origin of He II emission is the infall of metal-free gas onto an overdensity at

$z \sim 2-3$ [Yang et al., 2006], but distinguishing this scenario from true Pop III is unfortunately not as transparent. Both cases produce similar He II luminosities, but their He II/Lyman-α flux ratios are predicted to differ by up to a factor of 10 [Schaerer, 2003, Yang et al., 2006]. As we will discuss further, however, the He II/Lyman-α flux ratio may not be a viable differentiator.

In practice, the He II/Lyman-α flux ratio is highly variable along the line of sight due to several factors that affect both the Lyman-α and He II observed fluxes. It is well known that Lyman-α photons are strongly affected by resonant scattering and dust absorption; more than half of these photons from high redshift LAEs are estimated to be absorbed by the IGM [Haiman, 2002]. These effects can shrink the Lyman-α EW and alter the shape of the line profile. The He II EW is predicted to be highly sensitive to the age of the Pop III cluster, and the emission signature disappears rapidly due to the short lifetimes of these massive stars [Schaerer, 2002]. In the case of an instantaneous burst of Pop III SF, the He II EW is expected to peak at $\sim 100\,\text{Å}$ at the zero age of the cluster and becomes undetectable only ~ 2 Myrs later [Schaerer, 2003]. On the other hand, in the case of ongoing SF, the He II EW is expected to reach $\sim 20\,\text{Å}$. These values suggest that high redshift He II emission is accessible with current deep surveys [Nagao et al., 2008], but only if the Pop III source is younger than 2 Myrs or is harboring constant SF with a high enough SFR.

Additionally, all models predicting Pop III stellar He II emission assume that all photons with energies > 54.4 eV ionize one He^+ ion, but in practice nearby neutral hydrogen appropriates some of these photons. This competition between He^+ and HI for ionizing photons can cost He II some of its line strength [Stasińska and Tylenda, 1986].

Due to the high nebular continuum flux around the He II line, the He II EW is expected to be smaller than that of the Lyman-α line [Schaerer, 2003]; the He II/Lyman-α flux ratio for Pop III stars is estimated to be < 0.1 [Schaerer, 2003].

All of the environmental factors and theoretical uncertainties outlined above strongly influence how we interpret observations, for it is not clear if or how well the intrinsic He II/Lyman-α flux ratio will be preserved or even if both lines will be visible simultaneously. Though certainly complicated, the Lyman-α and He II λ1640 lines are very promising tools for approaching the next frontier- the first stars to ever form in the Universe. Mapping fluctuations in Lyman-α and He II λ anisotropies at high redshift, as opposed to directly seeking these lines in individual galaxies, could provide us with a more far-reaching methodology that could allow us to characterize the sources responsible for cosmic reionization.

CHAPTER 5

Conclusion

In Chapter 2, we have modeled fluctuations in the LW and Lyman-α radiation backgrounds using a variation of the halo model. First, we calculated the LW power spectrum and found that the power is characterized by an abrupt cut-off at the LW horizon distance, r_{LW}; the power turns over at the horizon wavenumber, k_{LW}, unless the sources are so rare that the one-halo term dominates (i.e., correlations are determined by the flux profiles of individual sources).

We found that the fluctuations in the background are weak and should not lead to substantial spatial fluctuations in H_2 content. Once a population of low-mass halos produces enough stars to generate a threshold LW background large enough to destroy their own H_2 reservoirs used for cooling, star formation can only proceed in larger halos with more substantial reservoirs. Our model predicts that, by the time this threshold is reached, fluctuations in the intensity field will be quite small, so this transition will be rather homogeneous across the entire Universe.

Next we considered the fluctuations in the Lyman-α background in a similar fashion. The Lyman-α flux profile imprints a series of wiggles on the shape of the power, corresponding to the series of horizon steps that characterize the profile. Unfortunately, unlike the LW case, these signature wiggles are washed out once we account for halo growth over time. We found that the amplitude of the Lyman-α power is smaller than that for the LW background by a factor of ~ 2 for scales larger than ~ 15 cMpc. The smaller fluctuations are due to the large Lyman-α

horizon distance, $r_{Ly\alpha} \sim 3r_{LW}$, allowing the halos to 'see' further.

We used our model for the fluctuations in the Lyman-α background to generate power spectra for the brightness temperature, T_b, of the 21-cm signal. We find our values to be in good agreement with previous estimates [Pritchard and Furlanetto, 2006, Barkana and Loeb, 2005a] that used a very different approach to estimate the radiation field fluctuations. We do not see a signature feature present in the power in contrast to the distinct LW turnover.

In Chapter 3, we have modeled the contribution from high redshift galaxies to the mean intensity and fluctuations of the NIRB using a variation of the halo model. We have constrained the star formation efficiency by using the cold accretion model described in [Muñoz, 2012] to estimate the LF and luminosity density at high redshift, then matching this to the results of [Robertson et al., 2013] and [Oesch et al., 2012].

We find that in order to approach a match of Pop III contributions to observations of the mean NIRB intensity excess, multiple stringent conditions must be met: we would need ionizing efficiencies that are at least an order of magnitude higher than the values proposed by [Schaerer, 2002] and an extremely top-heavy stellar IMF that extends out to at least $\sim 1000 M_{\odot}$. We would require Pop III SF to persist in minihalos until $z \sim 8$, an unlikely scenario as minihalos are thought to have been sterilized well before this time due to high levels of the cosmic LW BG wiping out their supplies of H_2, which they need to cool gas and form stars [Holzbauer and Furlanetto, 2012]. Additionally, an extreme top-heavy stellar IMF could result in too many black holes, which may overproduce the X-ray background.

The angular PS of the NIRB we find is relatively flat over the scales of interest; Pop III stars are suggested to dominate the anisotropy of the CIRB in the NIR for $1 \leq \lambda \leq 4\mu$m over tens of arcminute scales while unresolved galaxies at $z \geq 3$ are expected to dominate at $\lambda \geq 4\mu$m for all angular scales [Cooray et al., 2004].

Existing measurements clearly show an excess in clustering at 30 arcsecond to a few tens of arcminute angular scales, beyond what can be accounted for by normal galaxies. We find that in contrast to previous studies, we cannot distinguish between different models with varying threshold mass, M_{min}, by studying the shape of the fluctuations. A smaller M_{min} results in lower shot noise levels but a higher clustering amplitude, resulting in a flattened overall shape for all choices of threshold mass. Additionally, by using a luminosity per halo mass that varies with M_{min} and SF efficiencies matched to high redshift observations, we determine a fluctuation amplitude that is several orders of magnitude below current measurements.

The Pop III stellar contribution to the mean NIRB intensity and fluctuations is certainly present and finite but could in fact be even smaller than previously thought, implying that indeed, a previously unknown or unconsidered luminous source population at high redshift must be the culprit. Hopefully future measurements with the Cosmic Infrared Background Experiment (CIBER, [Zemcov et al., 2011]), which will offer a wide field of view to measure fluctuations at even larger angular scales, will shed new light on this mystery and provide additional and more accurate measurements of the NIRB excess.

In Chapter 4, we have proposed a new method for detecting primordial metal-free and very metal-poor stellar populations by cross-correlating fluctuations in intensity of Lyman-α and He II $\lambda1640$ emission sourced from high redshifts. Cross-correlating the Lyman-α and He II $\lambda1640$ lines is a very robust method for detecting Pop II/Pop III stellar populations, since (1) the two lines together allow us to better isolate the redshift of source emission, and (2) the presence of the He II $\lambda1640$ emission is extremely sensitive to stellar metallicity; it appears to be unique to extremely metal poor stars with $\log(Z/Z_{\odot}) < -5.3$ [Schaerer, 2003]. Since ground-based instruments are very much limited by atmospheric contamination in the NIR, we propose that a space-borne experiment could map out Lyman-α

and He II anisotropies over a broad range of redshifts with narrow-band observations surveyed over a reasonable patch of sky. [Oh et al., 2001] suggest that He II recombination lines could be detectable with the upcoming *James Webb Space Telescope* (JWST) even at redshifts beyond $z \sim 10$.

Though certainly complicated, the Lyman-α and He II λ1640 lines are very promising tools for approaching the next frontier- the first stars to ever form in the Universe. Mapping fluctuations in Lyman-α and He II λ anisotropies at high redshift, as opposed to directly seeking these lines in individual galaxies, could provide us with a more far-reaching methodology that could allow us to characterize the sources responsible for cosmic reionization.

References

[Abel et al., 2002] Abel, T., Bryan, G. L., and Norman, M. L. (2002). the formation of the first star in the universe. *Science*, 295:93–98.

[Aharonian et al., 2006] Aharonian, F., Akhperjanian, A. G., Bazer-Bachi, A. R., Beilicke, M., Benbow, W., and Berge, D. (2006). a low level of extragalactic background light as revealed by gamma-rays from blazars. *Nature*, 440:1018–1021.

[Ahn et al., 2009] Ahn, K., Shapiro, P. R., Iliev, I. T., Mellema, G., and Pen, U.-L. (2009). The inhomogeneous background of h2-dissociating radiation during cosmic reionization. *ApJ*, 695:1430–1445.

[Barkana and Loeb, 2001a] Barkana, R. and Loeb, A. (2001a). In the beginning: the first sources of light and reionization of the universe. *PhysRep*, 349:125–238.

[Barkana and Loeb, 2001b] Barkana, R. and Loeb, A. (2001b). In the beginning: the first sources of light and the reionization of the universe. *PhysRep*, 349:125–238.

[Barkana and Loeb, 2004] Barkana, R. and Loeb, A. (2004). Unusually large fluctuations in the statistics of galaxy formation at high redshift. *ApJ*, 609:474–481.

[Barkana and Loeb, 2005a] Barkana, R. and Loeb, A. (2005a). Detecting the earliest galaxies through two new sources of 21 centimeter fluctuations. *ApJ*, 626:1–11.

[Barkana and Loeb, 2005b] Barkana, R. and Loeb, A. (2005b). A method for separating the physics from the astrophysics of high-redshift 21 centimeter fluctuations. *ApJ*, 624:L65–L68.

[Becker et al., 2001] Becker, R. H., Fan, X., White, R. L., Strauss, M. A., Narayanan, V. K., Lupton, R. H., Gunn, J. E., Annis, J., Bahcall, N. A., Brinkmann, J., Connolly, A. J., Csabai, I., Czarapata, P. C., Doi, M., Heckman, T. M., Hennessy, G. S., Ivezić, Z., Knapp, G. R., Lamb, D. Q., McKay, T. A., Munn, J. A., Nash, T., Nichol, R., Pier, J. R., Richards, G. T., Schneider, D. P., Stoughton, C., Szalay, A. S., Thakar, A. R., and York, D. G. (2001). Evidence for reionization at z 6: Detection of a gunn-peterson trough in a z=6.28 quasar. *AJ*, 122:2850–2857.

[Bharadwaj and Ali, 2004] Bharadwaj, S. and Ali, S. S. (2004). The cosmic microwave background radiation fluctuations from hi perturbations prior to reionization. *MNRAS*, 352:142–146.

[Bond et al., 1986] Bond, J. R., Carr, B. J., and Hogan, C. J. (1986). Spectrum and anisotropy of the cosmic infrared background. *ApJ*, 306:428–450.

[Bouwens et al., 2013] Bouwens, R. J., Bradley, L., Zitrin, A., Coe, D., Franx, M., Zhend, W., Smit, R., Host, O., Postman, M., Moustakas, L., Labbé, I., Carrasco, M., Molino, A., Donahue, M., Kelson, D. D., Meneghetti, M., Jha, S., Benítez, N., Lemze, D., Umetsu, K., Broadhurst, T., Moustakas, J., Rosati, P., Jouvel, S., Bartelmann, M., Ford, H., Graves, G., Grillo, C., Infante, L., Jimenez-Teja, Y., Lahav, O., Maoz, D., Medezinski, E., Melchior, P., Merten, J., Nonino, M., Ogaz, S., and Seitz, S. (2013). A census of star-forming galaxies in the z 9-10 universe based on hst+spizter observations over 19 clash clusters: three candidate z 9-10 galaxies and improved constraints on the star formation rate density at z 9.2. *ArXiv e-prints*, 1211.2230.

[Bouwens et al., 2007] Bouwens, R. J., Illingworth, G. D., Franx, M., and Ford, H. (2007). Uv luminosity functions at z 4,5, and 6 from the hubble ultra deep field and other deep hubble space telescope acs fields: Evolution and star formation history. *ApJ*, 670:928–958.

[Bouwens et al., 2011a] Bouwens, R. J., Illingworth, G. D., Labbé, I., Oesch, P. A., Trenti, M., Carollo, C. M., van Dokkum, P. G., Franx, M., Stiavelli, M., Gonzalez, V., Magee, D., and Bradley, L. (2011a). A candidate redshift z 10 galaxy and rapid changes in that population at an age of 500 myr. *Nature*, 469:504–507.

[Bouwens et al., 2011b] Bouwens, R. J., Illingworth, G. D., Oesch, P. A., Labbé, I., Trenti, M., van Dokkum, P., Franx, M., Stiavelli, M., Carollo, C. M., Magee, D., and Gonzalez, V. (2011b). Ultraviolet luminosity functions from 132 z 7 and z 8 lyman-break galaxies in the ultra-deep hudf09 and wide-area early release science wfc3/ir observations. *ApJ*, 737:90.

[Brinchmann et al., 2008] Brinchmann, J., Pettini, M., and Charlot, S. (2008). new insights into the stellar content and physical conditions of star-forming galaxies at z=2-3 from spectral modeling. *MNRAS*, 385:769–782.

[Bromm et al., 2002] Bromm, V., Coppi, P. S., and Larson, R. B. (2002). the formation of the first stars. i. the primordial star-forming cloud. *ApJ*, 564:23–51.

[Bromm et al., 2001] Bromm, V., Kudritzki, R. P., and Loeb, A. (2001). Generic spectrum and ionization efficiency of a heavy initial mass function for the first stars. *ApJ*, 552:464–472.

[Bromm and Larson, 2004] Bromm, V. and Larson, R. B. (2004). The first stars. *ARA&A*, pages 79–118.

[Bromm and Loeb, 2004] Bromm, V. and Loeb, A. (2004). Accretion onto a primordial protostar. *NewA*, 9:353–364.

[Bromm et al., 2009] Bromm, V., Yoshida, N., Hernquist, L., and McKee, C. F. (2009). The formation of the first stars and galaxies. *Nature*, 459:49–54.

[Brown and Mathews, 1970] Brown, R. L. and Mathews, W. G. (1970). theoretical continuous spectra of gaseous nebulae. *ApJ*, 160:939.

[Cambrésy et al., 2001] Cambrésy, L., Reach, W. T., Beichmann, C. A., and Jarrett, T. H. (2001). The cosmic infrared background at 1.25 and 2.2 microns using dirbe and 2mass: A contribution not due to galaxies? *ApJ*, 555:563–571.

[Cantalupo et al., 2008] Cantalupo, S., Porciani, C., and Lilly, S. J. (2008). Mapping neutral hydrogen during reionization with the lyman-alpha emission from quasar ionization fronts. *ApJ*, 672:48–58.

[Cappelluti et al., 2013] Cappelluti, N., Kashlinsky, A., Arendt, R. G., Comastri, A., Fazio, G. G., Finoguenov, A., Hasinger, G., Mather, J. C., Miyaji, T., and Moseley, S. H. (2013). Cross-correlating cosmic infrared and x-ray background fluctuations: Evidence of significant black hole populations among the cib sources. *ApJ*, 769:68.

[Cassata et al., 2013] Cassata, P., Fèvre, O. L., Charlot, S., Contini, T., Cucciati, O., Garilli, B., Zamorani, G., Adami, C., Bardelli, S., Brun, V. L., Lemaux, B., Maccagni, D., Pollo, A., Pozzetti, L., Tresse, L., Vergani, D., Zanichelli, A., and Zucca, E. (2013). He ii emitters in the vimos vlt deep survey: Population iii star formation or peculiar stellar populations in galaxies at 2¡z¡4.6? *A&A*, 556:68.

[Chen and Miralda-Escudé, 2004] Chen, X. and Miralda-Escudé, J. (2004). The spin-kinetic temperature coupling and the heating rate due to lyman-alpha scattering before reionization: predictions for 21 centimeter emission and absorption. *ApJ*, 602:1–11.

[Clark et al., 2008] Clark, P. C., Glover, S. C. O., and Klessen, R. S. (2008). the first stellar cluster. *ApJ*, 672:757–764.

[Clark et al., 2011a] Clark, P. C., Glover, S. C. O., Klessen, R. S., and Bromm, V. (2011a). gravitational fragmentation in turbulent primordial gas and the initial mass function of population iii stars. *ApJ*, 727:110.

[Clark et al., 2011b] Clark, P. C., Glover, S. C. O., Smith, R. J., Greif, T. H., Klessen, R. S., and Bromm, V. (2011b). the formation and fragmentation of disks around primordial protostars. *Science*, 331:1040.

[Coe et al., 2013] Coe, D., Zitrin, A., Carrasco, M., Shu, X., Zheng, W., Postman, M., Bradley, L., Koekemoer, A., Bouwens, R., Broadhurst, T., Monna, A., Host, O., Moustakas, L., Ford, H., Moustakas, J., van der Wel, A., Donahue, M., Rodney, S. A., Benítez, N., Jouvel, S., Seitz, S., Kelson, D. D., and Rosati,

P. (2013). Clash: three strongly lensed images of a candidate z 11 galaxy. *ApJ*, 762:32.

[Cooray et al., 2004] Cooray, A., Bock, J. J., Keating, B., Lange, A. E., and Matsumoto, T. (2004). First star signature in infrared background anisotropies. *ApJ*, 606:611–624.

[Cooray et al., 2012a] Cooray, A., Gong, Y., Smidt, J., and Santos, M. G. (2012a). A measurement of the intrahalo light fraction with near-infrared background anisotropies. *ArXiv e-prints*, 1210.6031.

[Cooray et al., 2012b] Cooray, A., Gong, Y., Smidt, J., and Santos, M. G. (2012b). The near-ir background intensity and anisotropies during the epoch of reionization. *ApJ*, 756:92.

[Cooray and Sheth, 2002] Cooray, A. and Sheth, R. (2002). Halo models of large scale structure. *PhysRep*, 372:1–129.

[Cooray et al., 2007] Cooray, A., Sullivan, I., Chary, R.-R., Bock, J. J., Dickinson, M., Ferguson, H. C., Keating, B., Lange, A. E., and Wright, E. L. (2007). Ir background anisotropies in spitzer goods images and constraints on first galaxies. *ApJ*, 659:L91–L94.

[Cooray and Yoshida, 2004] Cooray, A. and Yoshida, N. (2004). First sources in infrared light: stars, supernovae and miniquasars. *MNRAS*, 351:L71–L77.

[Couchman and Rees, 1986a] Couchman, H. M. P. and Rees, M. J. (1986a). Pregalactic evolution in cosmologies with cold dark matter. *MNRAS*, 221:53–62.

[Couchman and Rees, 1986b] Couchman, H. M. P. and Rees, M. J. (1986b). Pregalactic evolution in cosmologies with cold dark matter. *MNRAS*, 221:53–62.

[Dalal et al., 2010] Dalal, N., Pen, U.-L., and Uros, S. (2010). Large-scale bao signatures of the smallest galaxies. *JCAP*, 11:007.

[Dawson et al., 2004] Dawson, S., Rhoads, J. E., Malhotra, S., Stern, D., Dey, A., Spinrad, H., Jannuzi, B. T., Wang, J., and Landes, E. (2004). spectroscopic properties of the z 4.5 lya emitters. *ApJ*, 617:707–717.

[Dijkstra et al., 2004] Dijkstra, M., Haiman, Z., and Loeb, A. (2004). A limit from the x-ray background on the contribution of quasars to reionization. *ApJ*, 613:646–654.

[Dijkstra et al., 2008] Dijkstra, M., Haiman, Z., Mesinger, A., and Wyithe, J. S. B. (2008). Fluctuations in the high-redshift lyman-werner background: close halo pairs as the origin of supermassive black holes. *MNRAS*, 391:1961–1972.

[Dijkstra and Wyithe, 2007] Dijkstra, M. and Wyithe, J. S. B. (2007). very massive stars in high-redshift galaxies. *MNRAS*, 379:1589–1598.

[Dopita and Sutherland, 2002] Dopita, M. A. and Sutherland, R. S. (2002). *Astrophysics of the Diffuse Universe*, Berlin: Springer.

[Dunlop et al., 2013] Dunlop, J. S., Rogers, A. B., McLure, R. J., Ellis, R. S., Robertson, B. E., Koekemoer, A., Dayal, P., Curtis-Lake, E., Wild, V., Charlot, S., Bowler, R. A. A., Schenker, M. A., Ouchi, M., Ono, Y., Cirasuolo, M., Furlanetto, S. R., Stark, D. P., Targett, T. A., and Schneider, E. (2013). The uv continua and inferred stellar populations of galaxies at z=7-9 revealed by the hubble ultra-deep field 2012 campaign. *MNRAS*, 432:3520–3533.

[Dwek et al., 1998] Dwek, E., Arendt, R. G., Hauser, M. G., Fixsen, D., Kelsall, T., Leisawitz, D., Pei, Y. C., Wright, E. L., Mather, J. C., Moseley, S. H., Odegard, N., Shafer, R., Silverberg, R. F., and Weiland, J. L. (1998). The cobe diffuse infrared background experiment search for the cosmic infrared background. iv. cosmological implications. *ApJ*, 508:106–122.

[Eisenstein and Hu, 1999] Eisenstein, D. J. and Hu, W. (1999). Power spectra for cold dark matter and its variants. *ApJ*, 511:5–15.

[Ellis et al., 2013] Ellis, R. S., McLure, R. J., Dunlop, J. S., Robertson, B. E., Ono, Y., Schenker, M. A., Koekemoer, A., Bowler, R. A. A., Ouchi, M., Rogers, A. B., Curtis-Lake, E., Schneider, E., Charlot, S., Stark, D. P., Furlanetto, S. R., and Cirasuolo, M. (2013). The abundance of star-forming galaxies in the redshift range 8.5-12: New results from the 2012 hubble ultra deep field campaign. *ApJ*, 763:L7.

[Elridge and Stanway, 2012] Elridge, J. J. and Stanway, E. R. (2012). The effect of stellar evolution uncertainties on the rest-frame ultraviolet stellar lines of c iv and he ii in high-redshift lyman-break galaxies. *MNRAS*, 419:479–489.

[Fan et al., 2002] Fan, X., Narayanan, V. K., Strauss, M. A., White, R. L., Becker, R. H., Pentericci, L., and Rix, H.-W. (2002). Evolution of the ionizing background and the epoch of reionization from the spectra of z 6 quasars. *AJ*, 123:1247–1257.

[Fan et al., 2006] Fan, X., Strauss, M. A., Becker, R. H., White, R. L., Gunn, J. E., Knapp, G. R., Richards, G. T., Schneider, D. P., Brinkmann, J., and Fukugita, M. (2006). Constraining the evolution of the ionizing background and the epoch of reionization with z 6 quasars. ii. a sample of 19 quasars. *AJ*, 132:117–136.

[Fazio et al., 2004] Fazio, G. G., Hora, J. L., Allen, L. E., Ashby, M. L. N., Barmby, P., Deutsch, L. K., Huang, J. S., Kleiner, S., Marengo, M., Megeath, S. T., Melnick, G. J., Pahre, M. A., Patten, B. M., Polizotti, J., Smith, H. A., Taylor, R. S., and Wang, Z. (2004). the infrared array camera (irac) for the spitzer space telescope. *ApJS*, 154:10–17.

[Fernandez et al., 2012] Fernandez, E. R., Iliev, I. T., Komatsu, E., and Shapiro, P. R. (2012). The cosmic near infrared background iii: Fluctuations, reionization, and the effects of minimum mass and self-regulation. *ApJ*, 750:20.

[Fernandez and Komatsu, 2006] Fernandez, E. R. and Komatsu, E. (2006). The cosmic near-infrared background: Remnant light from early stars. *ApJ*, 646:703–718.

[Fernandez et al., 2010] Fernandez, E. R., Komatsu, E., Iliev, I. T., and Shapiro, P. R. (2010). The cosmic near-infrared background. ii. fluctuations. *ApJ*, 710:1089–1110.

[Ferrara, 2001] Ferrara, A. (2001). physical processes at cosmic dawn. *in "The Physics of Galaxy Formation", ASP Conference Proceedings*, 222:301.

[Field, 1958] Field, G. B. (1958). Excitation of the hydrogen 21-cm line. *Proc. IRE*, 46:240–250.

[Field, 1959] Field, G. B. (1959). The spin temperature of intergalactic neutral hydrogen. *ApJ*, 129:536.

[Field et al., 1966] Field, G. B., Somerville, W. B., and Dressler, K. (1966). Hydrogen molecules in astronomy. *ARA&A*, 4:207.

[Furlanetto, 2006] Furlanetto, S. R. (2006). The global 21-centimeter background from high redshifts. *MNRAS*, 371:867–878.

[Furlanetto and Loeb, 2005] Furlanetto, S. R. and Loeb, A. (2005). Is double reionization physically plausible? *ApJ*, 634:1–13.

[Furlanetto et al., 2006] Furlanetto, S. R., Oh, S. P., and Briggs, F. H. (2006). Cosmology at low frequencies: the 21 cm transition and the high-redshift universe. *PhysRep*, 433:181–301.

[Gilmore, 2012] Gilmore, R. C. (2012). constraining the near-infrared background light from population iii stars using high-redshift gamma-ray sources. *MNRAS*, 420:800–809.

[Gnedin, 2000] Gnedin, N. Y. (2000). Effect of reionization on structure formation in the universe. *ApJ*, 542:535–541.

[Gnedin and Hui, 1998] Gnedin, N. Y. and Hui, L. (1998). Probing the universe with the lyalpha forest - i. hydrodynamics of the low-density intergalactic medium. *MNRAS*, 296:44–55.

[Gorjian et al., 2000] Gorjian, V., Wright, E. L., and Chary, R. R. (2000). tentative detection of the cosmic infrared background at 2.2 and 3.5 microns using ground-based and space-based observations. *ApJ*, 536:550–560.

[Greif et al., 2011] Greif, T. H., Springel, V., White, S. D. M., Glover, S. C. O., Clark, P. C., Smith, R. J., Klessen, R. S., and Bromm, V. (2011). simulations on a moving mesh: the clustered formation of population iii protostars. *ApJ*, 737:75.

[Gunn and Peterson, 1965] Gunn, J. E. and Peterson, B. A. (1965). On the density of neutral hydrogen in intergalactic space. *ApJ*, 142:1633–1641.

[Haiman, 2002] Haiman, Z. (2002). the detectability of high-redshift lyman-alpha emission lines prior to the reionization of the universe. *ApJ*, 576:L1–L4.

[Haiman et al., 2000] Haiman, Z., Abel, T., and Rees, M. J. (2000). The radiative feedback of the first cosmological objects. *ApJ*, 534:11–24.

[Haiman et al., 1996a] Haiman, Z., Rees, M. J., and Loeb, A. (1996a). H 2 cooling of primordial gas triggered by uv irradiation. *ApJ*, 467:522.

[Haiman et al., 1997] Haiman, Z., Rees, M. J., and Loeb, A. (1997). Destruction of molecular hydrogen during cosmological reionization. *ApJ*, 476:458.

[Haiman et al., 1996b] Haiman, Z., Thoul, A. A., and Loeb, A. (1996b). Cosmological formation of low-mass objects. *ApJ*, 464:523.

[Helgason et al., 2012] Helgason, K., Ricotti, M., and Kashlinsky, A. (2012). Reconstructing the near-infrared background fluctuations from known galaxy populations using multiband measurements of luminosity functions. *ApJ*, 752:113.

[Hinshaw et al., 2012] Hinshaw, G., Larson, D., Komatsu, E., Spergel, D. N., Bennett, C. L., Dunkley, J., Nolta, M. R., Halpern, M., Hill, R. S., Odegard, N., Page, L., Smith, K. M., Weiland, J. L., Gold, B., Jarosik, N., Kogut, A., Limon, M., Meyer, S. S., Tucker, G. S., Wollack, E., and Wright, E. L. (2012). Nine-year wilkinson microwave anistropy probe (wmap) observations: Cosmological parameter results. *ArXiv e-prints*, 1212.5226.

[Hirata, 2006] Hirata, C. M. (2006). Wouthuysen-field coupling strength and application to high-redshift 21-cm radiation. *MNRAS*, 367:259–274.

[Holzbauer and Furlanetto, 2012] Holzbauer, L. N. and Furlanetto, S. R. (2012). Fluctuations in the high-redshift lyman-werner and ly-alpha radiation background. *MNRAS*, 419:718–731.

[Hu et al., 2004] Hu, E. M., Cowie, L. L., Capak, P., McMahon, R. G., Kayashino, T., and Komiyama, Y. (2004). the luminosity function of lya emitters at redshift z 5.7. *AJ*, 127:563–575.

[Iliev et al., 2007] Iliev, I. T., Mellema, G., Shapiro, P. R., and Pen, U.-L. (2007). Self-regulated reionization. *MNRAS*, 376:534–548.

[Jimenez and Haiman, 2006] Jimenez, R. and Haiman, Z. (2006). significant primordial star formation at redshifts z 3-4. *Nature*, 440:501–504.

[Karzas and Latter, 1961] Karzas, W. J. and Latter, R. (1961). Electron radiative transitions in a coulomb field. *ApJS*, 6:167.

[Kashikawa et al., 2006] Kashikawa, N., Shimasaku, K., Malkan, M. A., Doi, M., Matsuda, Y., Ouchi, M., Taniguchi, Y., Ly, C., Nagao, T., Iye, M., Motohara, K., Murayama, T., Murozono, K., Nariai, K., Ohta, K., Okamura, S., Sasaki, T., Shioya, Y., and Umemura, M. (2006). the end of the reionization epoch probed by lyman-alpha emitters at z=6.5 in the subaru deep field. *ApJ*, 648:7–22.

[Kashlinsky, 2005] Kashlinsky, A. (2005). Cosmic infrared background and early galaxy evolution [review article]. *PhysRep*, 409:361–438.

[Kashlinsky et al., 2012] Kashlinsky, A., Arendt, R. G., Ashby, M. L. N., Fazio, G. G., Mather, J., and Moseley, S. H. (2012). New measurements of the cosmic infrared background fluctuations in deep spitzer/irac survey data and their cosmological implications. *ApJ*, 753:63.

[Kashlinsky et al., 2007] Kashlinsky, A., Arendt, R. G., Mather, J., and Moseley, S. H. (2007). New measurements of cosmic infrared background fluctuations from early epochs. *ApJ*, 654:L5–L8.

[Komatsu et al., 2011] Komatsu, E., Smith, K. M., Dunkley, J., Bennett, C. L., Gold, B., Hinshaw, G., Jarosik, N., Larson, D., Nolta, M. R., Page, L., Spergel, D. N., Halpern, M., Hill, R. S., Kogut, A., Limon, M., Meyer, S. S., Odegard, N., Tucker, G. S., Weiland, J. L., Wollack, E., and Wright, E. L. (2011). Seven-year wilkinson microwave anisotropy probe (wmap) observations: cosmological interpretation. *ApJS*, 192:18.

[Larson, 1998] Larson, R. B. (1998). Early star formation and the evolution of the stellar initial mass function in galaxies. *MNRAS*, 301:569.

[Lejeune and Schaerer, 2001] Lejeune, T. and Schaerer, D. (2001). Database of geneva stellar evolution tracks and isochrones for hst-wfpc2, geneva and washington photometric systems. *A&A*, 366:538–546.

[Levenson et al., 2007] Levenson, L. R., Wright, E. L., and Johnson, B. D. (2007). Dirbe minus 2mass: Confirming the cirb in 40 new regions at 2.2 and 3.5 microns. *ApJ*, 666:34–44.

[Limber, 1954] Limber, D. N. (1954). The analysis of counts of the extragalactic nebulae in terms of a fluctuating density field. ii. *ApJ*, 119:655.

[Loeb and Furlanetto, 2013] Loeb, A. and Furlanetto, S. R. (2013). The first galaxies in the universe. *The First Galaxies in the Universe (Princeton University Press).*

[Machacek et al., 2003] Machacek, M. E., Bryan, G. L., and Abel, T. (2003). Effects of a soft x-ray background on structure formation at high redshift. *MNRAS*, 338:273–286.

[Madau and Pozzetti, 2000] Madau, P. and Pozzetti, L. (2000). Deep galaxy counts, extragalactic background light and the stellar baryon budget. *MNRAS*, 312:L9–L15.

[Madau and Silk, 2005] Madau, P. and Silk, J. (2005). Population iii and the near-infrared background excess. *MNRAS*, 359:L37–L41.

[Magliocchetti et al., 2003] Magliocchetti, M., Salvaterra, R., and Ferrara, A. (2003). First stars contribution to the near-infrared background fluctuations. *MNRAS*, 342:L25–L29.

[Maio et al., 2011] Maio, U., Koopmans, L. V. E., and Ciardi, B. (2011). the impact of primordial supersonic flows on early structure formation, reionization and the lowest-mass dwarf galaxies. *MNRAS*, 412:L40–L44.

[Malhotra and Rhoads, 2002] Malhotra, S. and Rhoads, J. E. (2002). large equivalent width lya line emission at z=4.5: young galaxies in a young universe? *ApJ*, 565:L71–L74.

[Matsumoto et al., 2005] Matsumoto, T., Matsuura, S., Murakami, H., Tanaka, M., Freund, M., Lim, M., Cohen, M., Kawada, M., and Noda, M. (2005). Infrared telescope in space observations of the near-infrared extragalactic background light. *ApJ*, 626:31–43.

[Matsumoto et al., 2011] Matsumoto, T., Seo, H. J., Jeong, W. S., Lee, H. M., Matsuura, S., Matsuhara, H., Oyabu, S., Pyo, J., and Wada, T. (2011). Akari observation of the fluctuation of the near-infrared background. *ApJ*, 742:124.

[Mazin and Raue, 2007] Mazin, D. and Raue, M. (2007). new limits on the density of the extragalactic background light in the optical to the far infrared from the spectra of all known tev blazars. *A&A*, 471:439–452.

[McBride et al., 2009] McBride, J., Fakhouri, O., and Ma, C.-P. (2009). Mass accretion rates and histories of dark matter haloes. *MNRAS*, 398:1858–1868.

[McDowell, 1961] McDowell, M. R. C. (1961). On the formation of h2 in h 1 regions. *Observatory*, 81:240–243.

[McLure et al., 2012] McLure, R. J., Dunlop, J. S., Bowler, R. A. A., Curtis-Lake, E., Schenker, M., Ellis, R. S., Robertson, B. E., Koekemoer, A. M., Rogers, A. B., Ono, Y., Ouchi, M., Charlot, S., Wild, V., Stark, D. P., Furlanetto, S. R., Cirasuolo, M., and Targett, T. A. (2012). A new multi-field determination of the galaxy luminosity function at z=7-9 incorporating the 2012 hubble ultra deep field imaging. *ArXiv e-prints*, 1212.5222.

[Mesinger and Furlanetto, 2009] Mesinger, A. and Furlanetto, S. R. (2009). The inhomogeneous ionizing background following reionization. *MNRAS*, 400:1461–1471.

[Mo and White, 1996] Mo, H. J. and White, S. D. M. (1996). An analytic model for the spatial clustering of dark matter haloes. *MNRAS*, 282:347–361.

[Moore et al., 1999] Moore, B., Quinn, T., Governato, F., Stadel, J., and Lake, G. (1999). Cold collapse and the core catastrophe. *MNRAS*, 310:1147–1152.

[Muñoz, 2012] Muñoz, J. A. (2012). Understanding the observed evolution of the galaxy luminosity function from z=6-10 in the context of hierarchical structure formation. *ArXiv e-prints*, 1104.0927.

[Muñoz and Loeb, 2011] Muñoz, J. A. and Loeb, A. (2011). constraining the minimum mass of high-redshift galaxies and their contribution to the ionization state of the intergalactic medium. *ApJ*, 729:99.

[Nagao et al., 2005] Nagao, T., Motohara, K., Maiolino, R., Marconi, A., Taniguchi, Y., Aoki, K., Ajiki, M., and Shioya, Y. (2005). an observational pursuit for pop iii stars in a lya emitter at z=6.33 through he ii emission. *ApJ*, 631:L5–L8.

[Nagao et al., 2008] Nagao, T., Sasaki, S. S., Maiolino, R., Grady, C., Kashikawa, N., Ly, C., Malkan, M., Motohara, K., Murayama, T., Schaerer, D., Shioya, Y., and Taniguchi, Y. (2008). a photometric survey for lya-he ii dual emitters: searching for pop iii stars in high-redshift galaxies. *ApJ*, 680:100–109.

[Naoz and Barkana, 2007] Naoz, S. and Barkana, R. (2007). The formation and gas content of high-redshift galaxies and minihaloes. *MNRAS*, 377:667–676.

[Navarro et al., 1996] Navarro, J. F., Frenk, C. S., and White, S. D. M. (1996). The structure of cold dark matter halos. *ApJ*, 462:563.

[Oesch et al., 2012] Oesch, P. A., Bouwens, R. J., Illingworth, G. D., Labbé, I., Trenti, M., Gonzalez, V., Carollo, C. M., Franx, M., van Dokkum, P. G., and Magee, D. (2012). Expanded search for z 10 galaxies from hudf09, ers, and candels data: evidence for accelerated evolution at z¿8? *ApJ*, 745:110.

[Oh and Haiman, 2002] Oh, S. P. and Haiman, Z. (2002). second-generation objects in the universe: radiative cooling and collapse of halos with virial temperatures above 10,000k. *ApJ*, 569:558–572.

[Oh et al., 2001] Oh, S. P., Haiman, Z., and Rees, M. J. (2001). Heii recombination lines from the first luminous objects. *ApJ*, 553:73–77.

[Orr et al., 2011] Orr, M. R., Krennrich, F., and Dwek, E. (2011). strong new constraints on the extragalactic background light in the near- to mid-infrared. *ApJ*, 733:77.

[Ouchi et al., 2008] Ouchi, M., Shimasaku, K., Akiyama, M., Simpson, C., Saito, T., Ueda, Y., Furusawa, H., Sekiguchi, K., Yamada, T., Kodama, T., Kashikawa, N., Okamura, S., Iye, M., Takata, T., Yoshida, M., and Yoshida, M. (2008). the subaru/xmm-newton deep survey (sxds). iv. evolution of lya emitters from z=3.1 to 5.7 in the 1 square degree field: Luminosity functions and agn. *ApJS*, 176:301–330.

[Pei, 1995] Pei, Y. C. (1995). the luminosity function of quasars. *ApJ*, 438:623–631.

[Postman et al., 2012] Postman, M., Coe, D., Benítez, N., Bradley, L., Broadhurst, T., Donahue, M., Ford, H., Graur, O., Graves, G., Jouvel, S., Koekemoer, A., Lemze, D., Medezinski, E., Molino, A., Moustakas, L., Ogaz, S., Riess, A., Rodney, S., Rosati, P., Umetsu, K., Zheng, W., Zitrin, A., Bartelmann, M., Bouwens, R., Czakon, N., Golwala, S., Host, O., Infante, L., Jha, S., Jimenez-Teja, Y., Kelson, D., Lahav, O., Lazkoz, R., Maoz, D., McCully, C., Melchior, P., Meneghetti, M., Merten, J., Moustakas, J., Nonino, M., Patel, B., Regös, E., Sayers, J., and Seitz, S. (2012). The cluster lensing and supernova survey with hubble: An overview. *ApJS*, 199:25.

[Prescott et al., 2009] Prescott, M. K., Dey, A., and Jannuzi, B. T. (2009). the discovery of a large lyman-alpha+he ii nebula at z=1.67: a candidate low metallicity region? *ApJ*, 702:554–566.

[Press and Schechter, 1974] Press, W. H. and Schechter, P. (1974). Formation of galaxies and clusters of galaxies by self-similar gravitational condensation. *ApJ*, 187:425–438.

[Pritchard and Furlanetto, 2006] Pritchard, J. R. and Furlanetto, S. R. (2006). Descending from on high: Lyman-series cascades and spin-kinetic temperature coupling in the 21-cm line. *MNRAS*, 367:1057–1066.

[Raiter et al., 2010] Raiter, A., Schaerer, D., and Fosbury, R. A. E. (2010). predicted uv properties of very metal-poor starburst galaxies. *A&A*, 523:64.

[Raue et al., 2009] Raue, M., Kneiske, T., and Mazin, D. (2009). first stars and the extragalactic background light: how recent gamma-ray observations constrain the early universe. *A&A*, 498:25–35.

[Ricotti et al., 2002] Ricotti, M., Gnedin, N. Y., and Shull, M. J. (2002). The fate of the first galaxies. ii. effects of radiative feedback. *ApJ*, 575:49–67.

[Robertson et al., 2013] Robertson, B. E., Furlanetto, S. R., Schneider, E., Charlot, S., Ellis, R. S., Stark, D. P., McLure, R. J., Dunlop, J. S., Koekemoer, A. M., Schenker, M., Ouchi, M., Ono, Y., Curtis-Lake, E., Rogers, A. B., Bowler, R. A. A., and Cirasuolo, M. (2013). New constraints on cosmic reionization from the 2012 hubble ultra deep field campaign. *ApJ*, 768:71R.

[Salpeter, 1955] Salpeter, E. E. (1955). The luminosoity function and stellar evolution. *ApJ*, 121:161.

[Salvaterra and Ferrara, 2003] Salvaterra, R. and Ferrara, A. (2003). The imprint of the cosmic dark ages on the near-infrared background. *MNRAS*, 339:973–982.

[Salvaterra et al., 2006] Salvaterra, R., Magliocchetti, M., Ferrara, A., and Schneider, R. (2006). The infrared glow of the first stars. *MNRAS*, 368:L6–L9.

[Santos et al., 2002] Santos, M. R., Bromm, V., and Kamionkowski, M. (2002). The contribution of the first stars to the cosmic infrared background. *MNRAS*, 336:1082–1092.

[Scannapieco et al., 2002] Scannapieco, E., Ferrara, A., and Madau, P. (2002). Early enrichment of the intergalactic medium and its feedback on galaxy formation. *ApJ*, 574:590–598.

[Scannapieco et al., 2003] Scannapieco, E., Schneider, R., and Ferrara, A. (2003). the detectability of the first stars and their cluster enrichment signatures. *ApJ*, 589:35–52.

[Scarlata et al., 2009] Scarlata, C., Colbert, J., Teplitz, H. I., Bridge, C., Francis, P., Palunas, P., Siana, B., Williger, G. M., and Woodgate, B. (2009). He ii emission in lyman-alpha nebulae: Agn or cooling radiation? *ApJ*, 706:1241–1252.

[Schaerer, 2002] Schaerer, D. (2002). On the properties of massive population iii stars and metal-free stellar populations. *A&A*, 382:28–42.

[Schaerer, 2003] Schaerer, D. (2003). the transition from population iii to normal galaxies: Lyalpha and he ii emission and the ionizing properties of high redshift starburst galaxies. *A&A*, 397:527–538.

[Schaerer, 2007] Schaerer, D. (2007). primeval galaxies. *in "The emission line Universe", XVIII Canary Islands Winter School of Astrophysics, Ed. J. Cepa, Cambridge Univ. Press, arXiv.0706.0139.*

[Schaerer, 2008] Schaerer, D. (2008). searching for pop iii stars and galaxies at high redshift. *IAUS*, 255:66–74.

[Shapley et al., 2003] Shapley, A. E., Steidel, C. C., Pettini, M., and Adelberger, K. L. (2003). rest-frame ultraviolet spectra of z 3 lyman break galaxies. *ApJ*, 588:65–89.

[Sheth and Tormen, 1999] Sheth, R. K. and Tormen, G. (1999). Large-scale bias and the peak backgroud split. *MNRAS*, 308:119–126.

[Shimasaku et al., 2006] Shimasaku, K., Kashikawa, N., Doi, M., Ly, C., Malkan, M., Matsuda, Y., Ouchi, M., Hayashino, T., Iye, M., Motohara, K., Murayama, T., Nagao, T., Ohta, K., Okamura, S., Sasaki, T., Shioya, Y., and Taniguchi, Y. (2006). Lya emitters at z=5.7 in the subaru deep field. *PASJ*, 58:313–334.

[Silva et al., 2013] Silva, M. B., Santos, M. G., Gong, Y., Cooray, A., and Bock, J. (2013). intensity mapping of lyman-alpha emission during the epoch of reionization. *ApJ*, 763:132.

[Spitzer, 1978] Spitzer, L. (1978). *Physical Processes in the Interstellar Medium (New York: Wiley).*

[Stacy et al., 2011] Stacy, A., Bromm, V., and Loeb, A. (2011). effect of streaming motion of baryons relative to dark matter on the formation of the first stars. *ApJ*, 730:L1.

[Stacy et al., 2010a] Stacy, A., Greif, T. H., and Bromm, V. (2010a). The first stars: formation of binaries and small multiple systems. *MNRAS*, 403:45–60.

[Stacy et al., 2010b] Stacy, A., Greif, T. H., and Bromm, V. (2010b). The first stars: formation of binaries and small multiple systems. *MNRAS*, 403:45–60.

[Stark et al., 2011] Stark, D. P., Ellis, R. S., and Ouchi, M. (2011). keck spectroscopy of faint 3¡z¡7 lyman break galaxies: a high fraction of line emitters at z=6. *ApJL*, 728:L2.

[Stasińska and Tylenda, 1986] Stasińska, G. and Tylenda, R. (1986). intermediate mass stars undergoing a very hot phase - can we measure their temperatures? *A&A*, 155:137–144.

[Stecher and Williams, 1967] Stecher, T. P. and Williams, D. A. (1967). Photodestruction of hydrogen molecules in h i regions. *ApJ*, 149:L29.

[Steidel et al., 1999] Steidel, C. C., Adelberger, K. L., Giavalisco, M., Dickinson, M., and Pettini, M. (1999). lyman-break galaxies at z¿ 4 and the evolution of the ultraviolet luminosity density at high redshift. *ApJ*, 519:1–17.

[Tegmark et al., 1997] Tegmark, M., Silk, J. I., Rees, M. J., Blanchard, A., Abel, T., and Palla, F. (1997). How small were the first cosmological objects? *ApJ*, 474:1.

[Thompson et al., 2007a] Thompson, R. I., Eisenstein, D., Fan, X., Rieke, M., and Kennicutt, R. C. (2007a). Constraints on the cosmic near-infrared background excess from nicmos deep field observations. *ApJ*, 657:669–680.

[Thompson et al., 2007b] Thompson, R. I., Eisenstein, D., Fan, X., Rieke, M., and Kennicutt, R. C. (2007b). Evidence for a z¡8 origin of the source-subtracted near-infrared background. *ApJ*, 666:658–662.

[Tornatore et al., 2007] Tornatore, L., Ferrara, A., and Schneider, R. (2007). population iii stars: hidden or disappeared? *MNRAS*, 382:945–950.

[Totani et al., 2001] Totani, T., Yoshii, Y., Iwamuro, F., Maihara, T., and Motohara, K. (2001). Diffuse extragalactic background light versus deep galaxy counts in the subaru deep field: Missing light in the universe? *ApJ*, 550:L137–L141.

[Trenti and Stiavelli, 2009] Trenti, M. and Stiavelli, M. (2009). Formation rates of population iii stars and chemical enrichment of halos during the reionization era. *ApJ*, 694:879–892.

[Tseliakhovich et al., 2011] Tseliakhovich, D., Barkana, R., and Hirata, C. M. (2011). Suppression and spatial variation of early galaxies and minihaloes. *MNRAS*, 418:906–915.

[Tseliakhovich and Hirata, 2010] Tseliakhovich, D. and Hirata, C. (2010). relative velocity of dark matter and baryonic fluids and the formation of the first structures. *PhRvD*, 82:083520.

[Tumlinson et al., 2001] Tumlinson, J., Giroux, M. L., and Shull, M. J. (2001). probing the first stars with hydrogen and helium recombination emission. *ApJ*, 550:L1–L5.

[Tumlinson et al., 2003] Tumlinson, J., Shull, M. J., and Venkatesan, A. (2003). cosmological effects of the first stars: evolving spectra of population iii. *ApJ*, 584:608–620.

[Turk et al., 2009] Turk, M. J., Abel, T., and O'Shea, B. (2009). The formation of population iii binaries from cosmological initial conditions. *Science*, 325:601.

[Vonlanthen et al., 2011] Vonlanthen, P., Semelin, B., Baek, S., and Revaz, Y. (2011). Distinctive rings in the 21 cm signal of the epoch of reionization. *A&A*, 532:97.

[Wouthuysen, 1952] Wouthuysen, S. A. (1952). *AJ*, 57:31.

[Wright, 2001] Wright, E. L. (2001). Dirbe minus 2mass: Confirming the cosmic infrared background at 2.2 microns. *ApJ*, 553:538–544.

[Wright and Johnson, 2001] Wright, E. L. and Johnson, B. D. (2001). dirbe minus 2mass: the cosmic infrared background at 3.5 microns. *ArXiv e-prints*, 0107205.

[Wright and Reese, 2000] Wright, E. L. and Reese, E. D. (2000). detection of the cosmic infrared background at 2.2 and 3.5 microns using dirbe observations. *ApJ*, 545:43–55.

[Yang et al., 2006] Yang, Y., Zabludoff, A. I., Davé, R., Eisenstein, D., Pinto, P. A., Katz, N., Weinberg, D. H., and Barton, E. J. (2006). probing galaxy formation with he ii cooling lines. *ApJ*, 640:539–552.

[Yoshida et al., 2003] Yoshida, N., Abel, T., Hernquist, L., and Sugiyama, N. (2003). Simulations of early structure formation: primordial gas clouds. *ApJ*, 592:645–663.

[Yoshida et al., 2008] Yoshida, N., Omukai, K., and Hernquist, L. (2008). Protostar formation in the early universe. *Science*, 321:669.

[Yoshida et al., 2006] Yoshida, N., Omukai, K., Hernquist, L., and Abel, T. (2006). formation of primordial stars in a cdm universe. *ApJ*, 652:6–25.

[Yue et al., 2013] Yue, B., Ferrara, A., Salvaterra, R., Xu, Y., and Chen, X. (2013). Infrared background signatures of the first black holes. *ArXiv e-prints*, 1305.5177.

[Zemcov et al., 2011] Zemcov, M., Arai, T., Battle, J., Bock, J. J., Cooray, A., Hristov, V., Keating, B., Kim, M.-G., Lee, D.-H., Levenson, L., Mason, P., Matsumoto, T., Matsuura, S., Mitchell-Wynne, K., Nam, U. W., Renbarger, T., Smidt, J., Sullivan, I., Tsumura, K., and Wada, T. (2011). Measuring light from the epoch of reionization with ciber, the cosmic infrared background experiment. *ArXiv e-prints*, 1101.1560.

[Zheng et al., 2012] Zheng, W., Postman, M., Zitrin, A., Moustakas, J., Shu, X., Jouvel, S., Høst, O., Molino, A., Bradley, L., Coe, D., Moustakas, L., Carrasco, M., Ford, H., Benítez, N., Lauer, T. R., Seitz, S., Bouwens, R., Koekemoer, A., Medezinski, E., Bartelmann, M., Broadhurst, T., Donahue, M., Grillo, C., Infante, L., Jha, S. W., Kelson, D. D., Lahav, O., Lemze, D., Melchior, P., Meneghetti, M., Merten, J., Nonino, M., Ogaz, S., Rosati, P., Umetsu, K., and van der Wel, A. (2012). A magnified young galaxy from about 500 million years after the big bang. *Nature*, 489:406–408.